공학박사학위논문

Non-volatile Memory Devices and Integrated Sensors for Multifunctional Stretchable and Bioresorbable Electronics

연성 및 생재흡수성 전자소자용 비휘발성 메모리 소자와 집적센서 구현

2015 년 8 월

서울대학교 대학원

화학생물공학부

손 동 희

Non-volatile Memory Devices and Integrated Sensors for Multifunctional Stretchable and Bioresorbable Electronics

지도 교수 김대형

이 논문을 공학박사 학위논문으로 제출함
2015 년 6 월

서울대학교 대학원
화학생물공학부
손동희

손동희의 공학박사 학위논문을 인준함
2015 년 7 월

위원장 성영은 (인)
부위원장 김대형 (인)
위원 현택환 (인)
위원 황철성 (인)
위원 이민백 (인)

Abstract

Non-volatile Memory Devices and Integrated Sensors for Multifunctional Stretchable and Bioresorbable Electronics

Donghee Son
School of Chemical and Biological Engineering
The Graduate School
Seoul National University

Over years, major advances in healthcare have been made through research in the fields of nanomaterials and microelectronics technologies. However, the mechanical and geometrical constraints inherent in the standard forms of rigid electronics have imposed challanges of unique integration and therapeutic delivery in non-invasive and minimally invasive medical devices. Here, we describe two types of multifunctional electronic systems.

The first type is wearable-on-the-skin systems that address the challenges via monolithic integration of nanomembranes fabricated by top-down approach,

nanotubes and nanoparticles assembled by bottom-up strategies, and stretchable electronics on tissue-like polymeric substrate. The system consists of physiological sensors, non-volatile memory, logic gates, and drug-release actuators. Some quantitative analyses on the operation of each electronics, mechanics, heat-transfer, and drug-diffusion characteristic validated their system-level multi-functionalities.

The second type is a bioresorbable electronic stent with drug-infused functionalized nanoparticles that takes flow sensing, temperature monitoring, data storage, wireless power/data transmission, inflammation suppression, localized drug delivery, and photothermal therapy. In vivo and ex vivo animal experiments as well as in vitro cell researches demonstrate its unrecognized potential for bioresorbable electronic implants coupled with bioinert therapeutic nanoparticles in the endovascular system.

As demonstrations of these technologies, we herein highlight two representative examples of multifunctional systems in order of increasing degree of invasiveness: electronically enabled wearable patch and endovascular electronic stent that incorporate onboard physiological monitoring, data storage, and therapy under moist and mechanically rigorous conditions.

Keywords: stretchable electronics, wearable electronics, bioresorbable electronics, non-volatile memory, logic gate, stent, sensor.

Student number: 2012-30742

Contents

Abstract

Chapter 1. Introduction

Chapter 2. Multifunctional wearable devices for diagnosis and therapy of movement disorders

Chapter 3. Stretchable Carbon Nanotube Charge-Trap Floating-Gate Memory and Logic Devices for Wearable Electronics

Chapter 4. Bioresorbable Electronic Stent Integrated with Therapeutic Nanoparticles for Endovascular Diseases

Chapter 1. Introduction

1.1 Organic flexible and wearable electronics

Recent progresses in flexible and wearable electronics are mainly driven by the efforts to reduce the power consumption of circuit components, to enhance device operating speeds and signal-to-noise ratios. Those real-time physiological measurement technologies are closely related to exploit interfaces on the human skin. Recently, flexible smart phones or wearable watches equipped with various sensing modules to detect physiological signals, such as electrocardiogram (ECG), electromyograph (EMG), body temperature, and motion-induced strain have attracted enormous attention due to their multifunctionality and portability. Although the flexible and wearable devices have proven their practicality, several limitations, such as low flexibility, low signal-to-ratio, high cost of the materials, and high power consumption still remain. Therefore, many research groups have extensively studied to overcome these problems.

Organic materials for flexible and wearable electronics: *flexible and stretchable electrode*

A conducting electrode composed of a mixture of single wall carbon nanotube (SWNT), an ionic liquid, and 4-methyl-2-pentanone is processed by a jet-milling homogenizer[1]. The SWNT-based paste can be patterned on PDMS substrate using screen printing (Figure 1.1a). Figure 1.1b, c indicate a plot of the conductivity as a function of stretchability since the SWNT content was changed from 1.4 to 15:8 wt%. The optimized composition of SWNTs enables the SWNT composite electrodes to have an extraordinarily high stretchability upto 118% and conductivity of 9.7 S cm^{-1}. These flexibility and stretchability of SWNT composite electrodes show higher conductivity than the conventional conducting rubber in different stretched modes. The SWNT composite electrode was applied to the electrode of the organic light-emitting diode (LED) to verify the electrical performance. The organic LED integrated with the SWNT composite electrode display higher brightness compared to the LED integrated with conventional conducting rubber, which evidences that the SWNT composite electrode with high conductivity and stretchability are crucial for flexible and wearable applications.

Conductive, transparent, and stretchable film coated by spraying SWNTs can be directly fabricated onto a substrate of PDMS. Figure 1.1e shows a series of schematic diagrams depicting the changes in morphology of SWNTs on a PDMS substrate with strain, as well as corresponding AFM images[2]. At strain of ≈170%, the resistance of the SWNT film irreversibly increased by several orders of the magnitude. Stretching capability of the film with elastic properties is shown in figure 1.1f,g. Biaxially stretched SWNT films were reversibly stretchable in any direction. These SWNT films embedded in PDMS are also highly transparent with bending-induced strains (Figure 1.1h).

Organic materials for flexible and wearable electronics: *carbon nanotube-based sensor*

The SWNT network film can be fabricated onto the PDMS substrate as an electrode of the transparent and stretchable capacitive sensor, which is capable of sensing local pressures (Figure 1.2a-c)[2]. The crosstalk among adjacent pixels in the 64-pixel device is low. And when the pressure is applied, the change in capacitance registered by the pixel is also five times higher than the average of that registered by the four adjacent pixels (Figure 1.2d). Although the sensor with both stretchable and transparent properties is difficult to maintain high performances with strains, the skin-like SWNT pressure sensor shows high transparency and high spatial sensitivity.

As one of the channel materials, semiconducting SWNT (s-SWNT) with high mobility, high flexibility, and low cost can be applied to operate flexible field effect transistors, which are basic modules for wearable active-matrix devices. Figure 1.2e shows optical and SEM images of fabricated 16 × 16 pixels and s-SWNT junctions, respectively[3]. The cross-sectional, exploded, and circuitry schematics of the s-SWNT active matrix with pressure sensing modules and the OLED are shown in Figure 1.2f-h. The full system fabricated on a polyimide substrate is heterogeneously integrated with 16 × 16 pixel arrays of s-SWNT TFTs, OLEDs, and pressure sensors. The interactive s-SWNT-based e-skin can be used to spatially map and visually display the applied pressure profiles (Figure 1.2i).

Organic materials for flexible and wearable electronics: ***film-based sensor***

Semiconducting organic film-based active matrix equipped with pressure sensitive rubber is used to analyze local strains on the surface of the artificial skin. The fabrication process of spin-coated organic film is simple to control its thickness, which is a key factor for the switching property. Figure 1.3a shows transfer curves of the pentacene film-based TFT with a sensing module under different pressures[4]. The spatial map is measured by the active matrix sensors

(Figure 1.3b). The electrical performances are well-maintained with radius R varying from 50 to 2 mm, which corresponds to tensile strain from 0.1% to 1.5%, respectively (Figure 1.3c). The image of the sensor array on a soft substrate is shown in figure 1.3d. The pressure map image obtained by using the active matrix sensor is shown in Figure 1.3e along with a photograph of the "rubber lips", which is used to apply pressure. Even though the resolution of the present device is too low to be compared with that of real "lip" image, it is enough to verify the shape of the lip. Although these active matrix sensors show good performances, the device has limitations, such as a heavyweight design and low conformability. In general, ultra-thin organic transistor or other components maintain their electrical properties since their thin passivation layer protects the device from ambient oxygen or water molecules, which are prone to cause malfunctions. Here, an ultra-lightweight pressure sensor array is fabricated on a polyethylene naphthalate (PEN) foil (Figure 1.3f-h)[5]. The device coated with the parylene film shows passivation ability enough to prohibit the influx of environmental gases. Figure 1.3i indicates an image (left) and a corresponding drain current map of a metallic ring placed on the sensing device (right). The spatial map of pressure information shows good sensitivity of the device. The device can be laminated onto the noncoplanar structures of a human upper jaw model (Figure 1.3j).

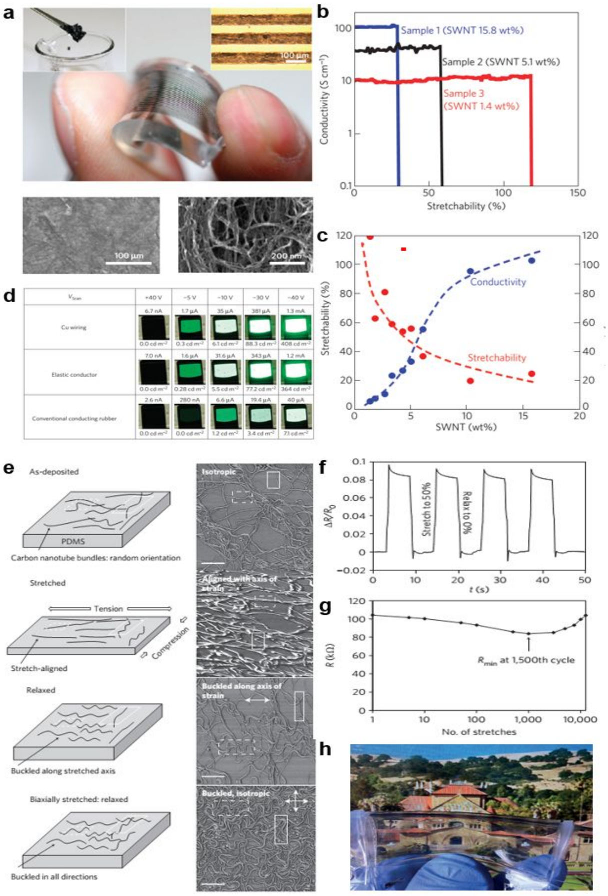

Figure 1.1 a, Stretchable conducting electrodes on a PDMS sheet. The insets indicate SWNTs dispersed in conducting paste and the magnified image of the electrode. The SEM images of the electrode (bottom). **b,** Conductivity of stretchable electrode as a function of stretchability. **c,** Stretchability and conductivity as a function of carbon nanotube content. **d,** Luminance of a display cell array. **e,** Morphological evolution of the SWNT film with different strains. **f,** Percentage change of resistance versus time stretching from 0 to 50%. **g,** Resistance versus stretching cycles. **h,** Image of the sensor composed of the SWNT film.

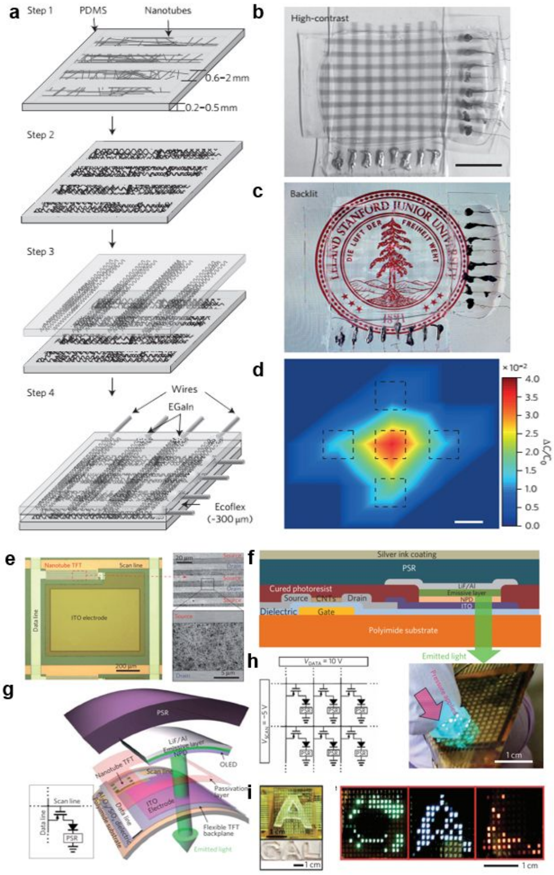

Figure 1.2 **a,** Fabrication processes for the arrays of transparent, compressible, capacitive sensors by spray-coating method. **b,** Photographical image of a64-pixel array of the pressure sensor. **c,** Image of the same device on a display. **d,** Map of the pressure distributions based on the change in capacitance. **e,** Optical image of a fabricated pixel before the integration of the OLED and pressure sensitive rubber. A SEM image of the SWNT junctions. **f,** Schematic of user-interactive e-skin. **g,** Exploded view of the e-skin. **h,** Circuit diagram of the e-skin matrix and **i,** corresponding spatial mapping array with different pressures.

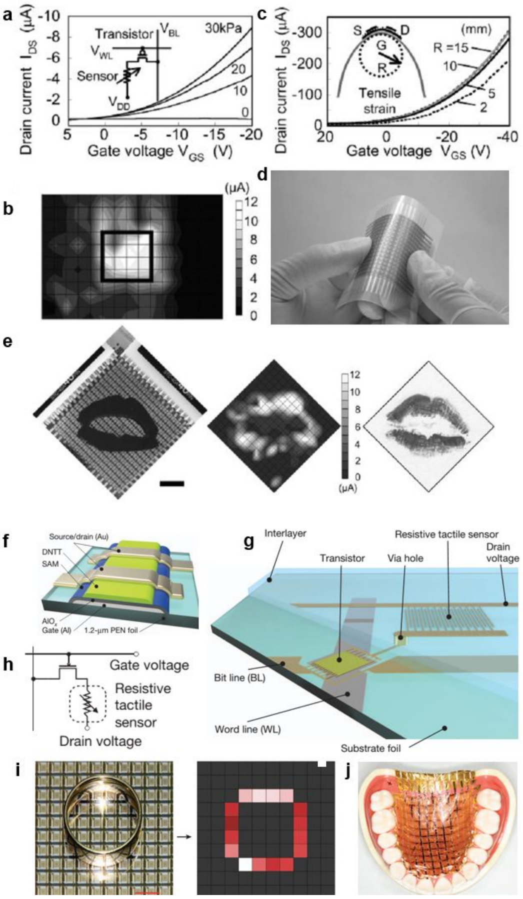

Figure 1.3 **a,** Transfer characteristics are measured for a sensor cell under application of various pressures from 0 to 30 kPa. **b,** Pressure map image with a rectangular rubber block. **c,** The transfer curves of a pentacene transistor with different radii (right). **d,** Image of the artificial skin. **e,** A pressure image of a kiss mark is taken by using the fabricated sensor array. **f,** Schematic of pentacene transistor. **g,** Illustration of a transistor with pressure sensing nodes. **h,** Circuit diagram of the artificial skin matrix. **i,** Images of pressure sensor array (left) and corresponding spatial map (right). **j,** Conformal contact of the array on a model of the human upper jaw.

Organic materials for flexible and wearable electronics: *organic logic circuits*

Semiconducting organic materials, such as carbon nanotube and pentacene, are expected to be used in the development of transistors and logic circuits for future devices, including low-cost, printable and wearable electronic devices. Here, this section covers the fabrication of high-performance thin-film transistors and integrated circuits on flexible and transparent substrates. Figure 1.4a shows an image of various device arrays composed of SWNT TFTs and integrated circuits, including inverters, ring oscillators (3, 11, and 21 stages), NOR and NAND gates, reset–set flip-flops, and delay flip-flops on a polyethylene naphthalate (PEN) substrate[6]. A structural image and IV characteristics of single SWNT transistor are shown in figure 1.4b,c. Figure 1.4d indicates the voltage transfer curves and gain characteristics of the SWNT inverter. Figure 1.4e-f show diagrams and graphs for a 21-stage ring oscillator with an output buffer on a PEN substrate where 44-SWNT-TFTs are integrated. The output voltage begins oscillating spontaneously at VDD = 22 V, and the oscillation frequency reaches 2.0 kHz at a VDD of 24 V. This value is significantly better than that reported in recent research. Besides, basic NOR/NAND gates and an integrated circuit (master–slave delay flip-flops) fabricated on the PEN substrate are also shown in figure 1.4g-j. Although

SWNT-based transistor and logic gates show good electrical performances, some drawbacks with an electrical hysteresis issue still remain in the devices, which causes degradation of the switching speed of the SWNT-based transistors.

Bottom-gate, pentacene-based transistor (P-Tr) shows not hysteresis effects in transfer curves (Figure 1.5a-c)[7]. Therefore, the P-Tr-based logic gate indicates good performances (gain of 40) (Figure 1.5d). Figure 1.5e shows an optical image (top, left) and a circuit diagram (bottom, left) of a 21-stage ring oscillator. The circuit oscillation with a signal delay per stage of 4.5 ms with flat and bent modes (right). The results indicate that high performanced P-Tr-based logic circuits can be used as a core component of the active devices. Even though SWNT or pentacene-based electronic devices show reliable operations, the organic materials are hard to handle compared to the inorganic materials in an ambient condition, which is the main reason to replace the organic materials with inorganic materials (Figure 1.6).

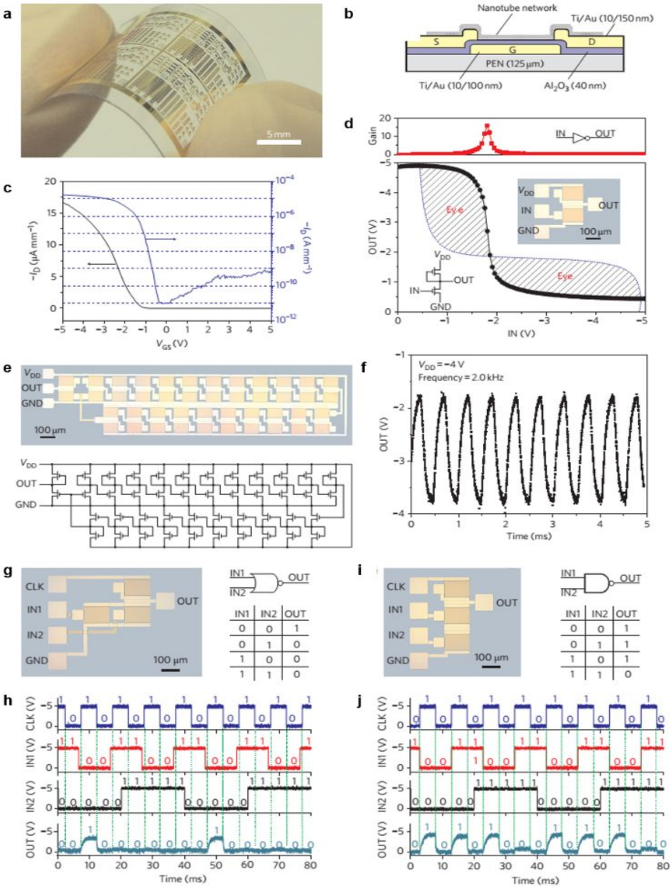

Figure 1.4 a, Image of SWNT devices fabricated on a flexible and transparent PEN substrate. **b,** Illustration of the SWNT transistor. **c,** Transfer curves of the SWNT transistor at V_d= -0.5 V (L_{ch}/W_{ch}=100/100 μm). **d,** Voltage transfer curves and gain characteristics of an inverter. Insets show optical micrograph, circuit schematic diagram of the inverter. **e,** Optical image (top) and circuit diagram (bottom) of a 21-stage ring oscillator. **f,** Output measurements of the ring oscillator with an oscillation frequency of 2.0 kHz at V_{DD} = -4V. **g-j,** Schematics and corresponding input-output characteristics of the NOR (**g,h,**) and NAND (**i,j,**) gates, respectively.

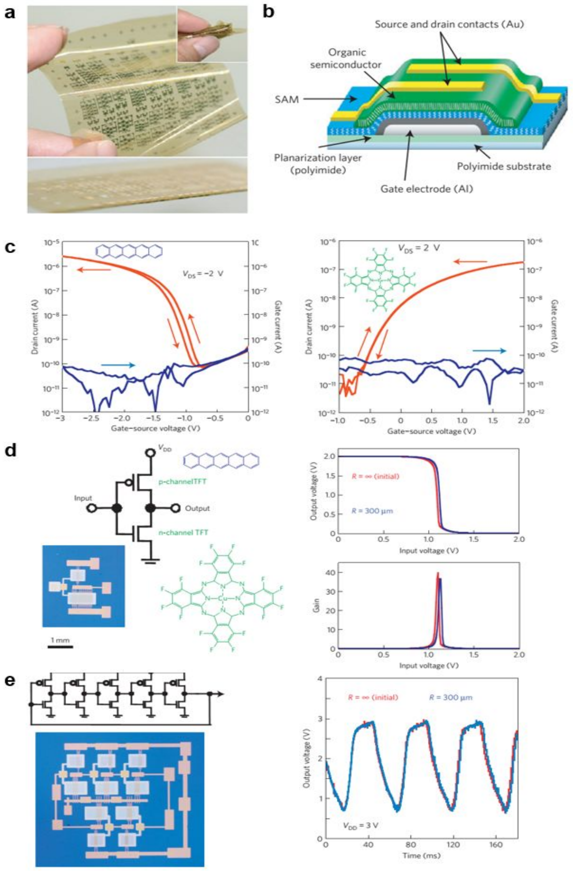

Figure 1.5 a, Images of a flexible polyimide substrate with functional organic TFTs and organic complementary circuits. **b,** Illustration of the pentacene transistor. **c,** Transfer curves of p-type (left) and n-type (right) channel transistors. **d,** Schematic diagram of the inverter circuit (left). The frames on the right show voltage transfer curves and gain characteristics of the inverter. **e,** Optical image (top, left) and circuit diagram (bottom, left) of a 21-stage ring oscillator. The circuit oscillation with a signal delay per stage of 4.5 ms with flat and bent modes (right).

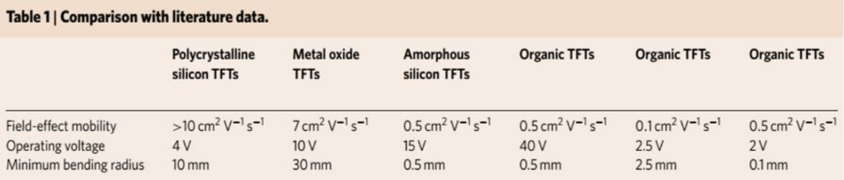

Table 1 | Comparison with literature data.

	Polycrystalline silicon TFTs	Metal oxide TFTs	Amorphous silicon TFTs	Organic TFTs	Organic TFTs	Organic TFTs
Field-effect mobility	$>10\,\mathrm{cm^2\,V^{-1}\,s^{-1}}$	$7\,\mathrm{cm^2\,V^{-1}\,s^{-1}}$	$0.5\,\mathrm{cm^2\,V^{-1}\,s^{-1}}$	$0.5\,\mathrm{cm^2\,V^{-1}\,s^{-1}}$	$0.1\,\mathrm{cm^2\,V^{-1}\,s^{-1}}$	$0.5\,\mathrm{cm^2\,V^{-1}\,s^{-1}}$
Operating voltage	4 V	10 V	15 V	40 V	2.5 V	2 V
Minimum bending radius	10 mm	30 mm	0.5 mm	0.5 mm	2.5 mm	0.1 mm

Figure 1.6 Comparison with literature data.

1.2 Inorganic flexible and wearable electronics

Inorganic materials for flexible and stretchable electronics: *flexible and stretchable nanomembrane*

In general, inorganic film-based devices are fabricated on wafers and the subsequently diced and integrated into micro/nanoelectronic circuits in order to perform data storage, signal verification, and recording. The film technologies can be applied to the flexible and stretchable electronics by transfer printing processes. The transfer-printed metallic and semiconducting nanomembranes with wavy geometries are of growing interests because they play key roles in producing high-performance flexible and stretchable electronic systems. In addition, pop-up electrodes are a new development to offer extremely high stretchability. This section covers the inorganic materials and mechanical design strategies for classes of electronic and bioelectronic devices.

Figure 1.7a shows SEM images of flat and wavy gold stripes on the PDMS substrate[8]. The wavy patterns are formed by local strains at the interface between the prestretched substrate and the gold film. This wavy structures enable the electrode to be stretched up to ~100% without electrical degradations (Figure 1.7b). The stretchability of the interconnection can be enhanced by using the pop-up bridge-like design (Figure 1.7c,d)[9], which enables the electrode to be stretched up to ~140%. The principle of enhanced stretchability is as follows. When external strain is applied along the x-directions, these noncoplanar electrodes effectively compensate the applied strains through the height difference. Stretchable semiconducting and piezoelectric nanomembranes can also be fabricated onto the elastic rubber by the same processes. Figure 1.7e-j show SEM images and a schematic of bucked PZT/Si/ nanomembranes transfer-printed onto the PDMS substrate[10-12]. These noncoplnar structures of the metallic and semiconducting nanomembranes are very crucial to achieve stretchable electronic devices.

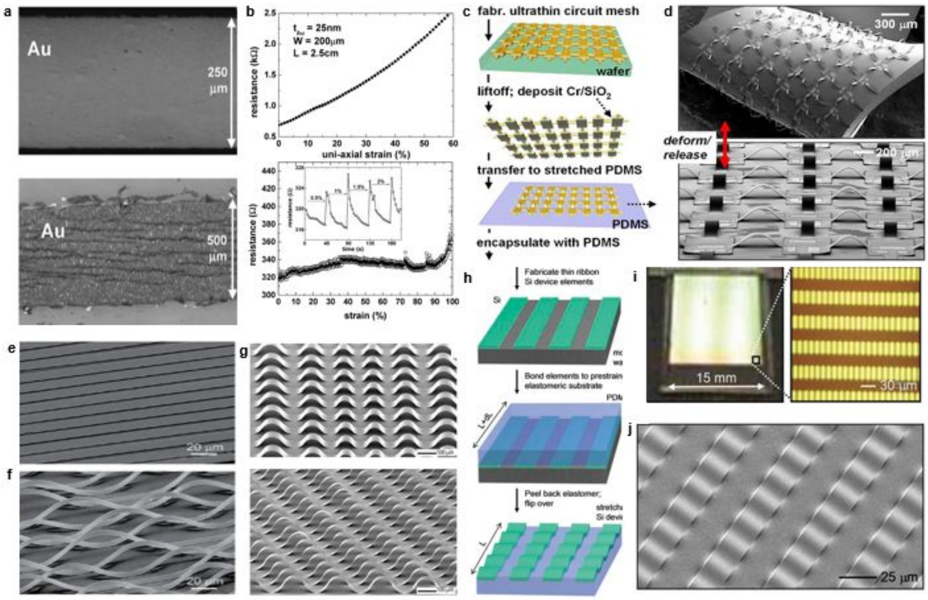

Figure 1.7 a, Images of gold electrodes on PDMS substrates with pristine (top) and stretched (bottom) modes. **b,** Electrical resistances of flat (top) and buckled (bottom) gold electrodes with different strains. **c,** Schematics of fabrication process for noncoplanar stretchable electronics with deformations. **d,** SEM images of the noncoplanar stretchable interconnects. . **e,** A SEM image of PZT ribbons transfer printed to rubber substrate with zero prestrain. **f,** Buckled PZT ribbons with prestrained conditions. **g,** SEM images of Si ribbon structures formed on a PDMS substrate pre-strained to 50% and patterned with different widths. **h,** Schematic illustration of the process for fabricating stretchable Silicon devices on rubber substrate. **i,** Optical images of wavy Si ribbons on PDMS. **j,** A SEM image of 4 wavy Si ribbons.

Inorganic materials for flexible and stretchable electronics: *flexible and stretchable multiplexed sensor arrays.*

Inorganic nanomaterials such as zero-dimensional (0D) quantum dot, 1D nanowire/nanotube, and 2D nanomembrane/nanoribbon structures have drawn attention to high performance electronic devices since they are reliable on the ambient conditions and compatible with the conventional mico-/nano-fabrication processes compared with the organic materials. In this section, 1D ZnO nanowires and 2D Si nanomembranes for multiplexed pressure sensor arrays based on the two-terminal metal-semiconductor-metal structure are introduced.

Although conventional architectures, such as 3D integrated circuits and wrap-gate vertical transistors, have presented efficient approaches in achieving high-density assembly of nano-scale devices, it is hard to fabricate the gate electrode and manage the interconnection layout to control an individual cell effectively within a high density matrix. To overcome the problems resulted from the complex fabrication processes, a simple capacitor-like structure is newly developed by combining vertically aligned ZnO nanowires with micro/nanofabrication processes. A schematic of a wrap-gate nanowire FET and a 3D strain-gated vertical piezotronic transistor (SGVPT) is shown in figure 1.8a[13]. The SGVPT shows a piezoelectronic effect which modulates local contact characteristics and charge carrier transport by strain-induced ionic polarization charges at the interface of a metal-semiconductor contact region (schottky barrier). The piezoelectronic effect made by modulations of schottky barrier heights according to the local stress or force is different from the voltage-gated operation of a traditional field effect transistor. Based on the piezoelectronic effect of the SGVPT, representative data from 23 taxels in a typical single-channel line scan (1 × 92) measurement for a SGVPT array device are shown in figure 1.8b,c. The current data from each taxel under 1 V bias, with and without external pressure (20 kPa) applied to a localized region (around taxels 45 and 46), are recorded and plotted with colors representing the ratio of the response amplitude for each taxel. The measured sensing range of a few kPa to ~30 kPa for a SGVPT array is well matched to the range of human finger pressure applied to sense texture and shape of the objects, 10 to 40 kPa. The area density of the SGVPT array is 8464 cm^{-2}, which is higher than that of organic material-based sensor arrays.

Even though nanowire-based sensor arrays show high density and high sensitivity performances, they have some drawbacks, which are electrical malfunctions caused by nonuniform growth rates of the nanowires and environmental heat-induced schottky barrier modulations. Single-crystalline silicon shows highly uniform electrical performances and high piezoresistive effects. Si nanomembranes derived from silicon-on-insulator substrates are fabricated on the flexible substrate by using transfer printing processes. A schematic and a circuit diagram of Si nanomembrane strain sensor arrays are shown in figure 1.8d[14]. The Wheatstone bridge (WB) design with four separate Si resistors enables the sensor to precisely sense the local pressures by verifying the changes in voltage drops across the four Si resistors. Figure 1.8e,f show the effective gauge factor (~43) and local strain map of the Si nanomembrane strain sensors. Also, the simulation results of the WB structure-based Si sensor prove the measurements right. The reliability results of the Si sensor in figure 1.8h show that the changes in output voltages do not vary with different bending radii from 25 to 12 mm with up to 1000 cycles. The bending tests of the Si sensor indicate the good flexibility.

Besides, the sensitivity to variations in temperature is also tested in Si sensor arrays. Figure 1.8i,j show fractional changes in resistance and voltage of a Si sensor as a function of temperature from 40 °C to 80 °C. For strain gauges in WB configurations, the same temperature coefficient of resistance (TCR) associated with four Si resistors yields the minimal temperature effect in the unstrained condition, although the temperature can affect the device performance in the strained state. Thus, high quality electrical data with decoupled ambient thermal fluctuations can be delivered by the WB design.

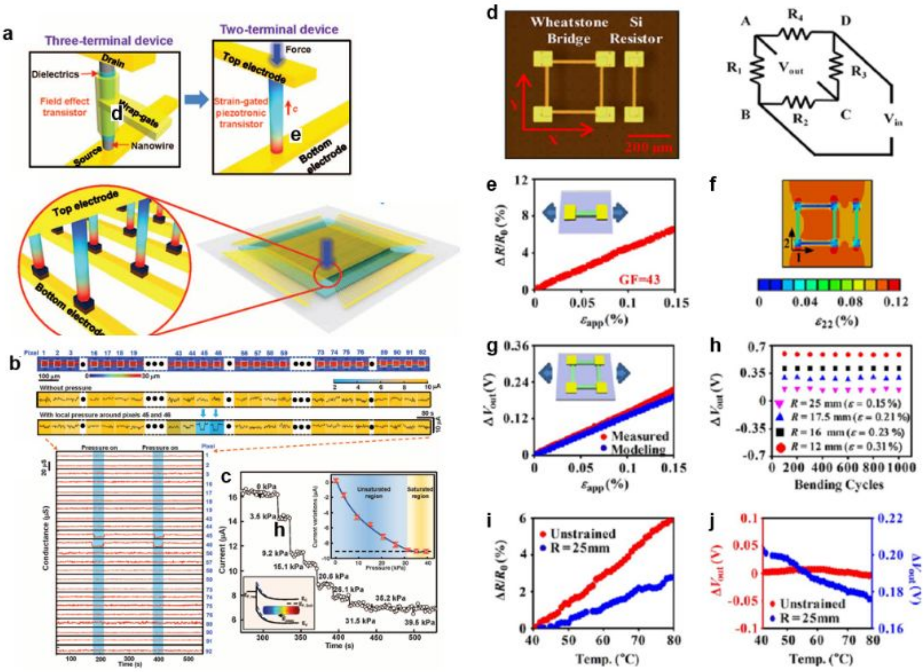

Figure 1.8 a, Schematic illustrations for structures of three-terminal and two-terminal transistors. The magnified illustration of strain-gated vertical piezotronic transistor array. **b,** Topological profile images (top view) of 23 selected taxels in a 1 × 92 piezotronic devices (single channel; top frame) and their corresponding current responses (middle and bottom frames). **c,** Single-channel conductance measurement. **d,** Top-view image and circuit diagram of a wheatstone bridge (WB) and Si resistor. **e,** Changes in resistance of a Si resistor versus tensile strain. **f,** Contour map data of strain distribution of the devices. **g,** Changes in output voltage of a WB versus strains. **h,** Voltage output from a WB measured at different stages of bending tests. **i,** Changes in resistance of a Si resistor versus temperature. **j,** Changes in output voltage of a WB versus different temperatures.

Inorganic materials for flexible and stretchable electronics: *flexible and stretchable transistors, LEDs and logic gates*

Making single-crystalline silicon complementary metal-oxide semiconductor (Si-CMOS) integrated circuits (ICs) reversibly flexible and stretchable is a prerequisite in realizing wearble electronic devices. This section covers transistors, logic gates, LEDs, other sensors taken from stretchable strategies, such as multilayer neutral mechanical plane designs, wavy structural layouts, and serpentine interconnects. Figure 1.9a,b show images and electrical measurements of of wavy Si-CMOS inverters formed with different tensile, uniaxial applied strains of ~3.9%[15]. The Poisson effect results in compression in the orthogonal direction, which leads to increases and decreases in the amplitudes and periods of waves with this orientation, respectively. Voltage transfer curves and transistor transfer characteristics (inset) of the inverter show high performances (gain of ~100) at supply voltages (V_{DD}) of 5V, consistent with circuit simulations that use the individual transistor responses. In addition, the effective mobilities of 290 cm^2/Vs and 140 cm^2/Vs for the n- and p-type MOSFET are also shown in figure 1.9b inset. The right frame of figure 1.9b summarizes the voltage at maximum gain (VM) for different strains along x- and y- directions. More complex stretchable circuits can be fabricated by using these inverters as the core components. Figure 1.9c,d show optical images (top, middle) and electrical measurements (bottom) of Si-CMOS ring oscillators that use three inverters under unstrained and strained conditions. The electrical data show the stable oscillation frequencies of ~3.0 MHz at supply voltages of 10 V, even under severe wavy deformations and strains of 5% and larger. Figure 1.9e,f show images and oscillation characteristics of a differential amplifier. The amplifier is designed to have a voltage gain of ~1.4 for a 500-mV peak-to-peak input signal. The data measured at different tensile strains along the red arrow show gains that vary by less than ~20%. Even though these devices are highly flexible and stretchable, the flexibility is not high enough to be conformally laminated onto the surface of the skin by soft contact.

A different approach is introduced Figure1.9g, in which the electrodes, electronics, sensors, power supply, and communication components are configured together into ultrathin, low-modulus, lightweight, and stretchable skin-like membranes. The devices and interconnects exploit ultrathin structures (<7 mm), neutral mechanical plane configurations, and optimized geometrical designs. The active components use established electronic materials, such as silicon and gallium arsenide, in the form of wavy nanomembranes. The results are high-performance electronic systems that offer reversible and elastic responses to large strain deformations with effective moduli (<150 kPa), bending stiffnesses (<1 nN m), and areal mass densities (<3.8 mg/cm^2) that are in orders of the magnitude smaller than those possible with the conventional electronic devices. These mechanical characteristics render materials hold strong adhesion on skin via van der Waals forces alone, without any adhesive tapes. Figure 1.9h indicates platinum-based temperature sensors built with serpentine interconnections (left) and in-plane strain gauges based on carbonblack-doped silicones (right). Figure 1.9i shows that the gate of a fully serpentine (FS) MOSFET is connected to an extended FS electrode for efficient coupling to the body potential. This FS MOSFET is used in the on-site signal amplifications. Images of LEDs/photodetectors based on AlInGaP (left) and Si photovoltaic cells (right) are shown in figure 1.9j. These strategies suggested here is able to attach high-performance electronic functionality on the surface of the skin. Thus, future wearable devices might be applicated by these technologies.

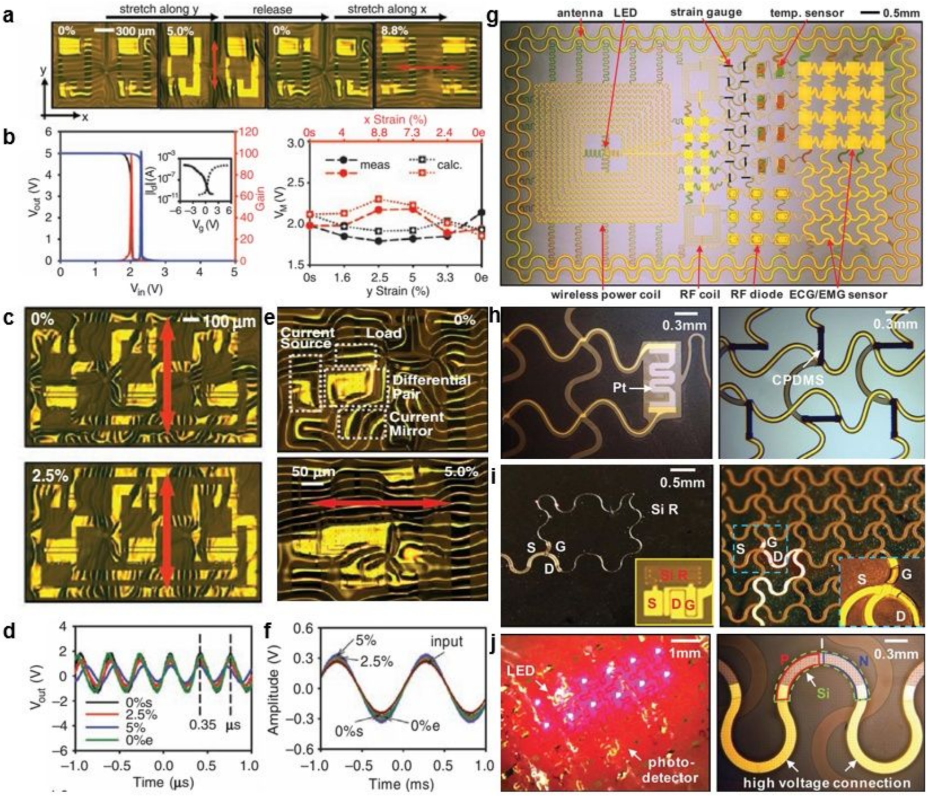

Figure 1.9 a, Optical images of buckled Si-CMOS inverters under tensile strains along the x and y directions. **b,** Measured and simulated voltage transfer curves (left) and threshold voltage characteristics (right) of Si-CMOS inverter, respectively. **c,** Images of ring oscillator with pristine and stretched modes. **d,** Voltage output of the ring oscillator versus time. **e,** Images of a differential amplifier with pristine and stretched modes. **f,** Frequency domain responses of an oscillator at various applied strains. **g,** Image of a representative sample for epidermal electronics. **h,** Images of a temperature and a strain sensor. **i,** Optical micrographs of a silicon MOSFET for local amplification. **j,** Optical images of an array of micro-scale Al/In/Ga/P LEDs (left) and photodetectors (right).

1.3 Flexible non-volatile memory devices

Flexible floating-gate memory

A current flash memory device has an ability of non-volatile data storage which can be divided into two types of the charge trap layers, based on how the floating gate is conducting (floating gate memory, FGM) or insulating (charge-trap flash memory, CTFM) materials. Compared to CTFM, the FGM shows very long retention and high operation voltages. The good property of retention results from FG materials, such as noble metals having high work functions. Figure 1.10a shows an image and a schematic for the structures of organic metal/oxide/semiconductor (MOS)-based FGM transistors[16]. The FG layer (Aluminum film) is sandwiched between the tunneling oxide (T_{ox}) and blocking oxide (B_{ox}) layers. T_{ox} (AlO_x+self-assembled monolayers (SAM)) is used as potential barrier for electron tunneling quantum transports between the semiconductor substrate and the FG layer. B_{ox} (AlO_x+SAM) is also used in thicker potential barrier than the T_{ox} layer to prevent a back-tunneling effect from the control gate. The FGM transistor with thick dielectrics causes bad gate-controllability due to the low effective field, compared to that with the thin SAM dielectric layer. The structure of the FGM transistor is shown in figure 1.10c. The electrical operation is governed by electron or hole trapping processes through the Fowler-Nordheim (FN) tunneling effect, which causes threshold voltage shift of the FGM device (Figure 1.10d). Controlling the thickness and quality of the various insulating layers can optimize low operation voltages.

To improve the ability of data storage, a 2D structure of previous FG can be replaced with 0D structures, which have the high surface-to-volume ratio (Figure 1.10e)[17]. Metal nanoparticle-based FG enables more electrons or holes to be trapped on the surface of the FG. In addition, the application of metal elements with high work functions to the FG can also be a good option. A TEM image of self-assembled gold nanoparticle (SGN) film is shown in Figure 1.10g. The TEM result shows that the SGN film as a core materials of the FGM is highly uniform. Figure 1.10h shows schematics describing the band bending of the SGN-FGM under applied positive/negative biases on the control gate. Holes are trapped in the SGN film by tunneling (the band gap of Al_2O_3 (T_{ox}) is ~8.8 eV) under a negative gate bias (PGM operation). The ERS operation (positive gate bias) discharges holes from the SGN-FG layer to the channel layer by FN tunneling through the T_{ox} layer. The electrical performance of a single SGN-FGM transistor is characterized under ambient conditions (Figure 1.10i). Figure 1.15i indicates the transfer curves and switching speed characteristics of the SGN-FGM transistor at different positive/negative gate voltages. These results indicate the effectiveness of charging/discharging of the charge carriers into/from the SGN-FG layer.

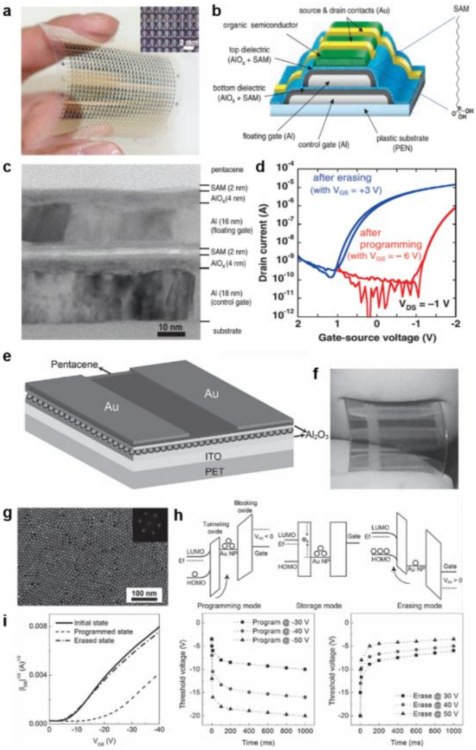

Figure 1.10 a, Images of an organic floating gate transistor device comprising 26 by 26 cells. **b,** Illustration of the pentacene-based floating gate memory. **c,** Cross-sectional TEM image of the memory. **d,** Transfer curves of the memory with erasing and programming modes. **e,** Schematic of the gold nanoparticle-integrated floating gate memory. **f,** Image of the flexible floating gate memory. **g,** Top-view TEM image of gold nanoparticle assembly. **h,** Band diagrams on different operation modes. **i,** Transfer characteristics and charging/discharging sensitivity of the memory on erasing and programming modes.

Flexible resistance random access memory

A single structure of RRAM similar to that of capacitor consists of top/bottom metal electrodes and insulator. The RRAM device designs show 4 types of structures, which indicate 1 resistor (1R), 1 transistor (1T)/1R, 1 diode (1D)/1R, and 1 selector (1S)/ 1R. This section covers efficient methods for realization of the RRAM array with the high cell density and non-disturbed multiplexing ability.

Figure 1.11a shows a flexible RRAM device array with the AgNW/MoO_x/MoS_2/AgNW 1R structure[18]. The MoS_2 film assembled by modified Langmuir-Blodgett film processes is transfer-printed on the inkjet-printed AgNW networks. MoO_x is then formed on the surface of the MoS_2 via thermal oxidation. Especially, the composition of Mo ions is devided into Mo^{5+} and Mo^{6+} states, which make the MoOx film conducting or insulating (Figure 1.11b), respectively. When the Mo^{6+} ions on the top surface of the MoO_x forms the schottky barrier at the MoO_x/AgNW interface, the MoS_2 RRAM device shows bipolar resistive switching in IV characteristics (Figure 1.11c). These results imply that the switching mechanism conform to the schottky emission conduction theory, in which heat is a driving force to enable mobile charge carriers to leap the schottky barrier. A plot of the resistive switching voltage of the MoS_2 RRAM as a function of the MoS_2 film thickness shows that MoS_2

RRAM has no dependence on the film thickness, because the resistive switching dominantly occurs at the interface between AgNWs and MoO_x. Meanwhile, the scan rates are highly correlated to the resistive switching voltages (Figure 1.11e).

The graphene oxide film also shows good resistive switching characteristics. A schematic of the cross-bar array on the flexible substrate is shown in figure 1.11f[19]. Figure 1.11g indicates the corresponding IV curves, which are bipolar resistive switching. The inset shows an image of flexed graphene oxide RRAM device arrays. The reliability of the RRAM device is tested during bending cycles of ~1000 with bending radii ranging from 7 mm to 20 mm (Figure 1.11h,i). Figure 1.11j shows a suggested resistive switching mechanism, in which mobile oxygen ions form the interfacial insulating/conducting layer at the top electrode applied by positive/negative voltages. The resistance states of the RRAM cell by these operations can be reversible.

Although these 1R-type RRAM arrays show attractive electrical characteristics, the neighboring cell operations in the large-scale area can disturb the individual cell access. Thus, RRAM array should protect the sneak path effect. The RRAM structures suggested in Figure 1.12 are promising candidates for large-scale RRAM demonstrations[20]. First, flexible 1T-1R arrays with a Al/a-TiO_2/Al RRAM cell structure are demonstrated in Figure 1.12a-e.

Figure 1.12a,b indicate schematics of the Si nanomembrane-based 1T-1R array and a single cell. The transfer curves and IV characteristics of the RRAM device connected to the Si TFT show good performances (Figure 1.12c-e). The electrical operations of the RRAM cell are controlled by the Si TFT, which can impede undesired external voltages. Thus, 1D-1R or 1S-1R structures are also highly efficient to protect electrical malfunctions by virtue of adopting the same procedures (Figure 1.12f-m)[21,22].

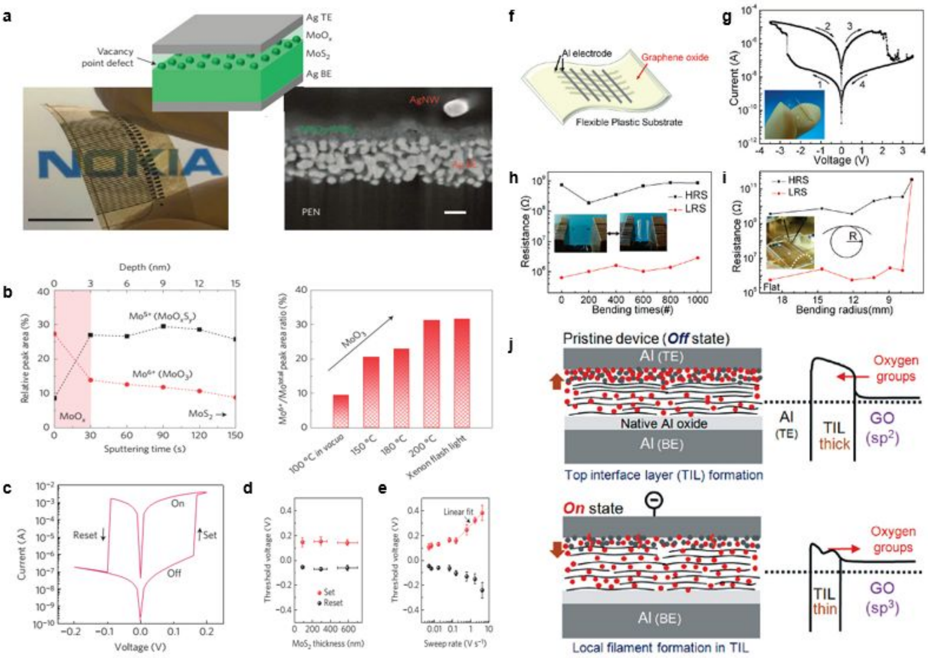

Figure 1.11 **a,** Schematic and images of MoS$_2$ resistive memory. **b,** XPS data for compositional analysis of Mo5$^+$ and Mo6$^+$ under different annealing conditions. **c,** Bipolar IV curves of the memory. **d,** The memory shows no dependency on the thickness of MoS$_2$. **e,** Threshold voltage of the memory as a function of scan rate. **f,** Schematic of the graphene oxide RRAM array. **g,** Bipolar IV curves of the memory. **h,** Endurance data with bending cycles and **i,** bending-induced strains. **j,** Schematic illustrations and simple band diagrams for the operational mechanism of the memory with LRS and HRS, respectively.

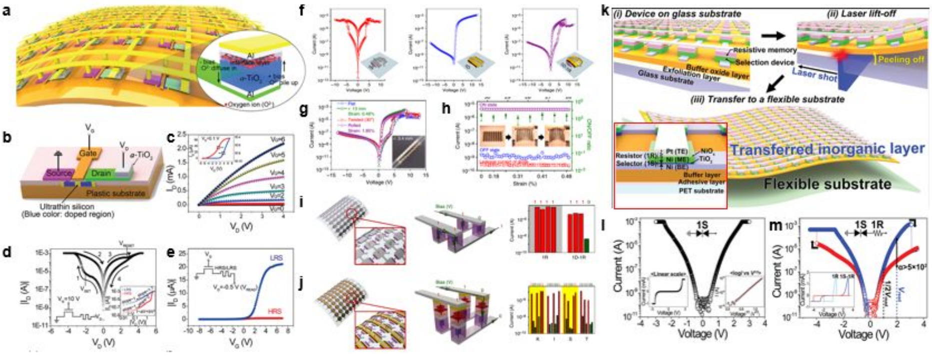

Figure 1.12 **a,** Schematic illustration of the 1 transistor and 1 RRAM array structures. **b,** Schematic of the Si MOSFET. **c,** Vd-Id and Vg-Id curves of the MOSFET. **d,** IV curves of the Al/TiO$_2$/Al RRAM. Inset shows double log-log plots of the RRAM cell. **e,** Transfer curves of the 1T-1R with HRS and LRS. **f,** IV characteristics of 1 resistor (R), 1 diode (D), and 1R-1D. **g,** IV curves of the 1T-1R with different strains. **h,** Endurance data with bending-induced strains. **i,** Schematics and data storage verifications of 1R array and **j,** 1D-1R array. **k,** Schematic illustrations of laser lift-off process of the 1 selector (S)-1R array. **l,** IV curves of the 1S and **m,** 1S-1R.

1.4 Bioresorbable materials and devices

Bioresorbable stent

Percutaneous coronary intervention (PCI) was introduced as an effective and safe treatment surgical method for single vessel and multivessel coronary atherosclerotic diseases in 1979. Since then, PCI has been widely used to treat cardiovascular diseases. Although PCI is an effective surgical procedure, its critical problems, such as restenosis, still remain, which is defined as the renarrowing of the treated vessel lumen to >50% occlusion, usually within 6 months after the PCI procedure. Especially, the inflammatory responses to the endothelial denudation and subintimal hemorrhage caused by the balloon angioplasty are estimated to be strongly correlated to the renarrowing phenomenon, because they result in the onset of several proliferative processes, including vascular smooth muscle cell (VSMC) proliferation and migration, extracellular matrix formation, and neointrimal hyperplasia. However, the causative mechanisms of restenosis have not yet been fully identified.

The introduction of drug-eluting stent (DES) was seen as an alternative to restenosis treatment and, initially, DES alleviated the incidence of restenosis significantly. Even though DES is a good approach toward the prevention of restenosis, in-stent restenosis (ISR) still remains as a problem, which is associated with foreign material in the coronary arteries. In light of the ISR-related issues including polymer-induced inflammation, thrombosis, and restenosis, the development of bioresorbable polymers has been a pivotal focus of the study. Figure 1.13a shows an image of the poly-lactic acid (PLA)-based stent, which has a zig-zag helical coil design with straight bridges. In the resorption process, hydrolysis of bonds of lactide components generates lactic acid that enters the Krebs cycle and is metabolized to carbon dioxide and water[23]. This PLA stent can cause polymer-induced inflammations because it has no antiproliferative drugs. The PLA-based sirolimus-eluting stent shown in figure 1.13b is advanced model to treat the inflammation associated with PCI and with polymer degradation[24]. However, these polymer-based stents do not hold sufficient radial strength for an appropriate duration. The magnesium alloy (WE-43) stent has sinusoidal in-phase hoops linked by straight bridges, which are solid for vessel recoil (Figure 1.13c). The metal stent is also bioresorbable and can be coated with therapeuctic polymers. Figure 1.1d,e show the effect of DES on the ISR. The DES with ammonium tetrathiomolybdate (TTM) shows high efficiency for the ISR compared with the control.

The therapeutic and bioresorbable stent platforms, mentioned above, are limited to diagnose and/or monitor endovascular diseases, because they have no functions of internal data processing and wireless transmission. Figure 1.13f shows a strainless steel stent with integrated fully wireless implantable cardiovascular pressure sensors[25]. The suggessted stent demonstrates fully wireless-pressure-sensing functionality with an external 35-dB·m RF powering source across a distance of 10 cm. The measurements made in a regulated pressure chamber demonstrate the ability of the wireless stent platform to achieve pressure resolutions of 0.5 mmHg over a range of 0–50 mmHg using a channel data-rate of 42.2 kb/s. However, these electronic components and strainless steel stent might cause ISR issues due to non-bioresorbability. Thus, all electronic components should be composed of bioresorbable materials in order to prevent inflammation-induced ISR. This approach will be covered in the next section.

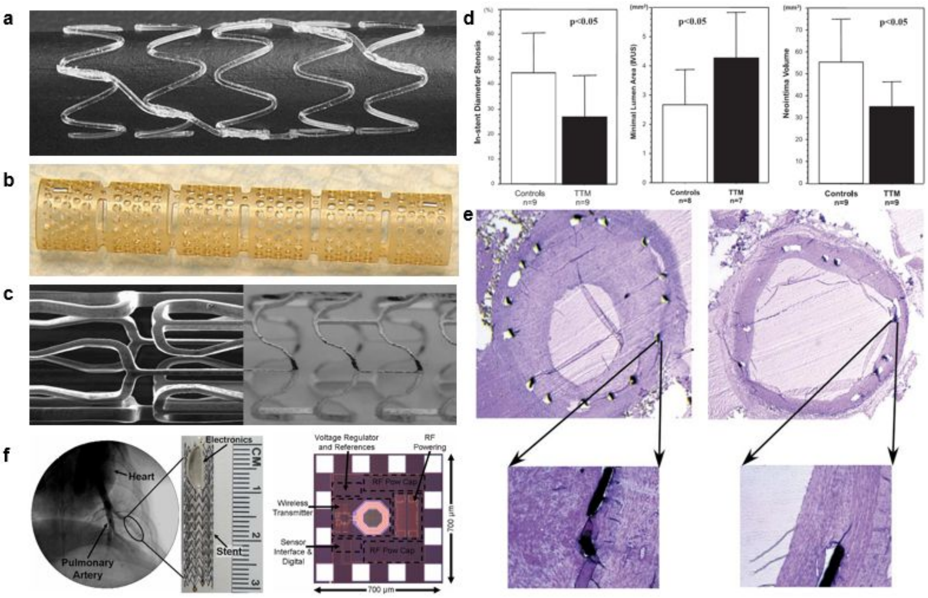

Figure 1.13 a-c, Images of polymer (**a**), polymer-drug (**b**), and magnesium alloy (**c**) stents. **d,** In-stent diameter stenosis measured by quantitative coronary angiography, minimal lumen area measured by intravascular ultrasound, and neointimal volume measured by histomorphometry. **e,** Representative histology of a control (left) and a tetrathiomolybdate (TTM)-treated (right) animal. **f,** Images of an electronic device-integrated on stainless stent.

Bioresorbable electronics

Bioresorbable materials such as metals (Zn, Mg, Mo, W), semiconductors (Si, ZnO, MgO), and polymers (PLA, PLGA, PCL) can be applied to the interconnection, active switching channel, and substrate, respectively. Electronic circuits based on the bioresorbable materials can exploit these transient behaviors including implantable medical sensors and therapeutic actuators that resorb in the body to avoid adverse long-term effects. Figure 1.14a,b show an image and a schematic of a bioresorbable electronic platform that includes transistors, diodes, inductors, capacitors, and resistors, with interconnects and interlayer dielectrics, all on a thin silk substrate[26]. All of the components are dissolved when immersed in water solution.

Figure 1.14c shows images of an LC (inductor-capacitor) oscillator composed of Mg electrodes and MgO dielectric layers (top, left), an array of Si nanomembrane diodes with Mg resistors (top, right), a p-type MOSFET array (bottom, left), and an inverter composed of n-type transistors (bottom, right). The corresponding data are shown in figure 1.14d. The electrical characteristics of the inductor are well matched to that of the LC oscillator. In addition, the resulting transfer curves for an n-channel device include saturation and linear regime mobilities of 560 $cm^2/V\cdot s$ and 660 $cm^2/V\cdot s$, respectively. V_d/I_d curves show good gate controllability at different gate voltages. The voltage transfer curves indicate that the inverter has the high gain value of ~7.8. The Mg antenna, one of the wireless core components is immersed in deionized (DI) water at room temperature (Figure 1.14e)[27]. The Mg interconnection and silk substrate completely disappear in ~2 hours by hydrolysis and simple dissolution, respectively. In addition to these electronic circuits, a self-powered device composed of bioresorbable materials (ZnO-Mg) is shown in figure 1.14f-k[28]. The power generation of the device is obtained from external mechanical forces-induced charge separations.

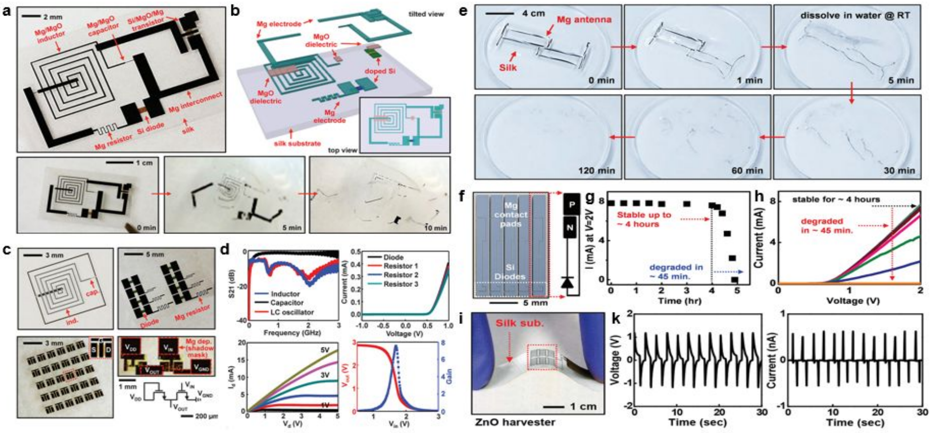

Figure 1.14 a, Image of a transient electronic device that includes transistors, diodes, inductors, capacitors, and resistors, with interconnects and interlayer dielectrics, all on a thin silk substrate. The bottom frames show images of the time sequence of dissolution in DI water. **b,** The exploded image of the transient system, with a top view in the lower right inset. **c,** Image of an LC (inductor-capacitor) oscillator composed of Mg electrodes and MgO dielectric layers (left) and an array of Si nanomembrane diodes with Mg resistors (right). The bottom frames show a p-type MOSFET array and an inverter composed of n-type transistors. **d,** Data measurement of the S_{21} scattering parameter of an inductor (blue), capacitor (black), and LC oscillator (red) at frequencies up to 3 GHz (top, left). IV curves of diodes connected to three different Mg resistors (top, right) are shown. Vd-Id curves of the n-type transistor (bottom, left). Voltage transfer curves and gain characteristics of the inverter (bottom, right). **e,** A set of images of an Mg-based antenna on a silk substrate illustrate the process of dissolution in DI water.. **f,** Measurements of dissolution kinetics of a diode encapsulated with 500 nm-thick MgO. **i,** Optical image of a ZnO/silk energy harvester. **k,**

Output voltage versus time, and output current versus time during cycles of bending.

References

1. Sekitani, T., *et al.* Stretchable active-matrix organic light-emitting diode display using printable elastic conductors. *Nat. Mater.* **2009**, *8*, 494-499.
2. Lipomi, D. J., *et al.* Skin-like pressure and strain sensors based on transparent elastic films of carbon nanotubes. *Nat. Nanotechnol.* **2011**, *6*, 788-792.
3. Wang, C., *et al.* User-interactive electronic skin for instantaneous pressure visualization. *Nat. Mater.* **2013**, *12*, 899-904.
4. Someya, T., *et al.* A large-area, flexible pressure sensor matrix with organic field-effect transistors for artificial skin applications. *PNAS* **2004**, *101*, 9966-9970.
5. Kaltenbrunner, M., *et al.* An ultra-lightweight design for imperceptible plastic electronics. *Nature 499*, **2013**, 458-463.
6. Sun, D.-M., *et al.* Flexible high-performance carbon nanotube integrated circuits. *Nat. Nanotechnol.* **2011**, *6*, 156-161.
7. Sekitani, T., *et al.* Flexible organic transistors and circuits with extreme bending stability. *Nat. Mater.* **2010**, *9*, 1015-1022
8. Lacour, S. P., *et al.* Stretchable interconnects for elastic electronic surfaces. *Proceedings of the IEEE.* **2005**, *93*, 1459-1467.

9. Kim, D.-H., *et al.* Materials and noncoplanar mesh designs for integrated circuits with linear elastic responses to extreme mechanical deformations. *PNAS* **2008**, *48*, 18675-18680.
10. Khang, D.- Y., *et al.* A stretchable form of single-crystal silicon for high-performance electronics on rubber substrates. *Science* **2006**, *311*, 208-212.
11. Sun, Y., *et al.* Controlled buckling of semiconductor nanoribbons for stretchable electronics. *Nat. Nanotechnol.* **2006**, *6*, 201-207.
12. Qi, Y., *et al.* Enhanced piezoelectricity and stretchability in energy harvesting devices fabricated from buckled PZT ribbons. *Nano Lett.* **2011**, *11*, 1331-1336.
13. Wu, W., *et al.* Taxel-addressable matrix of vertical-nanowire piezotronic transistors for active and adaptive tactile imaging. *Science* **2013**, *340*, 952-957.
14. Won, S. M., *et al.* Piezoresistive strain sensors and multiplexed arrays using assemblies of single-crystalline silicon nanoribbons on plastic substrates. *IEEE trans. on electron device.* **2011**, *58*, 4074-4078.
15. Kim, D.-H., *et al.* Stretchable and foldable silicon integrated circuits. *Science* **2008**, *333*, 838-843.
16. Sekitani, T., *et al.* Organic nonvolatile memory transistors for flexible sensor arrays. *Science* **2009**, *326*, 1516-1519.

17. Han, S.-T., *et al.* Microcontact printing of ultrahigh density gold nanoparticle monolayer for flexible flash memories. *Adv. Mater.* **2012**, *24*, 3356-3561.
18. Bessonov, A. A., *et al.* Layered memristive and memcapacitive switches for printable electronics. *Nat. Mater.* **2015**, *14*, 199-204.
19. Jeong, H. Y., *et al.* Graphene oxide thin films for flexible nonvolatile memory applications. *Nano Lett.* **2010**, *10*, 4381-4386.
20. Kim, S., *et al.* Flexible memristive memory array on plastic substrates. *Nano Lett.* **2011**, *11*, 5438-5442.
21. Ji, Y., *et al.* Flexible and twistable non-volatile memory cell array with all-organic one diode–one resistor architecture. *Nat. Commun.* **2013**, *4:2707.*
22. Kim, S., *et al.* Flexible crossbar-structured resistive memory arrays on plastic substrates via inorganic-based laser lift-Off. *Adv. Mater.* **2014**, *26*, 7480-7487.
23. Ormiston, J. A., *et al.* Bioabsorbable coronary stents. *Circulation: Cardio. Interven.* **2009**, *2*, 255-260.
24. Mandinov, L., *et al.* Inhibition of in-stent restenosis by oral copper chelation in porcine coronary arteries. *Am. J. Physiol. Heart Circ. Physiol.* **2006**, *291*, 2692-2697.Lipomi, D. J., *et al.*

25. Chow, E. Y., *et al.* Fully Wireless implantable cardiovascular pressure monitor integrated with a medical stent. *IEEE Tran. On Biomed. Eng.* **2010**, *57*, 1487-1496.
26. Hwang, S.-W., *et al.* A physically transient form of silicon electronics. *Science* **2012**, *337*, 1640-1644.
27. Hwang, S.-W., *et al.* Materials for bioresorbable radio frequency electronics. *Adv. Mater.* **2013**, *25*, 3526-3531.
28. Dagdeviren, C., *et al.* Transient, biocompatible electronics and energy harvesters based on ZnO. *Small* **2013**, *20*, 3398-3404.

Chapter 2. Multifunctional wearable devices for diagnosis and therapy of movement disorders

2.1 Introduction

Wearable sensor-laden devices that provide continuous measurement of key physiological parameters coupled with data storage and drug delivery constitute a radical advance in personal healthcare. Health monitoring devices in the form of wearable pads, wrist-bands and straps that provide long-term continuous recordings of electrophysiological activity and acute physiological responses have significantly improved our understanding of diseases, including heart failure[1], epilepsy[2] and Parkinson's disease[3,4]. Although conventional monitoring devices capture compelling physiological data, the form factors of existing devices restrict seamless integration with the skin[1], giving rise to wearability challenges and signal to noise limitations[2,4].

Electronic systems that incorporate inorganic and organic nanomaterials in flexible and stretchable configurations[5-9] are particularly powerful alternatives to bulky health monitoring devices, due to improvements in comfort and lesser social stigmas, which together drive compliance. This emerging class of electronics includes sensors, light emitting diodes, and associated circuit components that interface with internal organs (e.g. heart[10,11], brain[12,13]), skin[14], or through artificial skin scaffolds[15-17]. A key constraint of these flexible and stretchable electronics for the wearable biomedical devices, however, is in their inability to store recorded data in memory modules during continuous, long-term monitoring. Another desirable feature missing in emerging wearable devices is the ability to deliver advanced therapy in response to diagnostic patterns present in the collected data[18].

Resistive random access memory (RRAM), constructed from oxide nanomembranes (NMs), is an emerging class of high performance non-volatile memory[19-21]. RRAM devices are composed of stiff and brittle electronic materials, which tend to be mechanically incompatible with curvilinear, dynamically deforming, soft tissues. Although organic non-volatile memory has enabled flexible data-storage devices[22,23], there remain restrictions, such as high power consumption, insufficient reliability, and lack of stretchability.

In this paper, we demonstrate wearable bio-integrated systems with optimised performance of data storage, diagnostics, and drug delivery functionality in stretchable formats, which is enabled by the integration of bottom-up nanoparticles (NPs) and top-down nanomembranes (NMs). This nanoparticle-integrated system includes novel wearable low-power consumption non-volatile resistance memory devices, and programmable thermal actuators for controlled transdermal NP-assisted drug delivery along with well-known stretchable sensors (e.g. temperature and strain sensors). This system establishes new engineering design rules and guides for multifunctional healthcare system. Potential applications of these wearable patches range from monitoring physiological cues in patients of motion-related neurological disorders (movement disorders) to controlled drug delivery in response to diagnostic feedback. For example, let's suppose that a Parkinson's disease patient wears the current multifunctional device. Movement disorders, such as tremors, can be measured (Si NM strain sensors) and the monitored data will be stored in the integrated memory devices (Au NP RRAMs). The pattern of stored data will be analysed and categorised into specific disease modes. Then the corresponding feedback therapy (drug delivery from m-silica NP) will proceed transdermally with optimised rates (heater). The skin temperature will be simultaneously monitored (temperature sensor) to prevent skin burns during thermal control of the drug delivery rate.

***The contents of this chapter were published in Nature Nanotechnology**

(2014, 9, 397-404)

2.2 Experimental Section

Detailed switching mechanism of the wearable memory: The bipolar switching characteristics in I-V curves of RRAM can be attributed to the accumulation and depletion of oxygen. This accumulation and depletion depend on the bias polarity near the interface between top Al electrode and TiO_2 switching layer, where the oxygen-deficient TiO_x layer is formed (Figure 1.16, top). The interface between the bottom Al electrode and TiO_2 switching layer remains intact due to the presence of more stable AlO_x layer (Figure 1.16, bottom). Many RRAM devices are activated by the electroforming process, which makes conduction paths between cathode and anode. However, the initial set voltage of TiO_2-based memories is similar with following set voltages, and therefore, there is no need of the electroforming process. Additionally, Au NPs in TiO_2/Au NPs/TiO_2 structure produces charge trap sites[1], by which the low current level in MINIM can be explained. However, Au NPs are surrounded by alkyl chains (oleylamine ligands) and these ligands may also generate the charge trap sites. To clarify this ligand effect on the formation of charge trap sites, SAM (stearic acid, which is similar to oleylamine ligands) is used to functionalise TiO_2 NM surface (MISIM structure, Figure 1.5). However, MISIM structure did not show the decrease of switching current (Figure 1.4a).

Consequently, the ligand effect is negligible for the generation of charge trap sites. On the contrary, the increase of the number of Au NPs layers in the MINIM structure from one layer to three layers decreases the switching current further (Figure 1.4a). As a result, the number of layers of Au NPs is important for controlling the operation current, while the ligands have minimal influences.

Reliability tests (endurance, retention) of the wearable memory: The endurance operation is conducted by consecutive DC voltage sweeping from -4 V to 3 V. Each of high-resistance state (HRS) and low-resistance state (LRS) currents measured at the read voltage of -0.5 V shows stable operation (Figure 1.4e,g). In retention measurements, the individual resistance states are programmed by DC voltage bias. The high-resistance state (HRS) and low-resistance state (LRS) states are well sustained at read voltage of -0.5 V.

Cumulative probability plots of high-resistance state (HRS) and low-resistance state (LRS) in MIM and MINIM: Cumulative probability is a critical parameter in verifying the uniformity of resistive switching operation. Cumulative probabilities of high-resistance state (HRS) and low-resistance state (LRS) resistances are measured under compliance currents of 1 mA and 50 μA in 50 cells of the array, respectively. The on/off ratio between high-resistance state (HRS) and low-resistance state (LRS) in MIM and MINIM is approximately 10. Both MIM and MINIM show a good uniformity within the array.

Finite element modelling (FEM) of the strain distribution of stretchable memory: Multilayer stretchable memories are modelled as shell elements of multiple integration points in commercial finite element software ABAQUS. The elastomer substrate is modelled using 3D elements which bonds to only the intersections of the serpentine network. Strain distribution after 25% horizontally applied strain is shown in Figure 1.7i, 1.8. The maximum strain stayed below 0.008% in the intersection (switching layer, TiO_2 NM) and below 0.04% in the serpentine interconnects, which are both far below the failure strain of inorganic oxides (~1%).

.

Analytical modelling of the gauge factor of Si strain sensor: The Si strain gauges are modelled as 2D plane strain problem. When the substrate is subjected to a uniform tensile strain $\varepsilon_{\mathrm{app}}$, the normalised average strain in the Si NM is predicted to be

$$\frac{\varepsilon_{\mathrm{avg}}}{\varepsilon_{\mathrm{app}}} = \frac{\overline{E}_{\mathrm{s}} H}{\overline{E}_{\mathrm{Si}} h_{\mathrm{Si}} + \overline{E}_{\mathrm{PI}} h_{\mathrm{PI}} + \overline{E}_{\mathrm{s}} H} \quad \text{(S1)},$$

where $\overline{E}_{\mathrm{s}}$, H, $\overline{E}_{\mathrm{Si}}$, h_{Si} and $\overline{E}_{\mathrm{PI}}$, h_{PI} are the plane strain modulus and thickness of the substrate, Si and polyimide respectively. The substrate is 40:1 PDMS (E_{s} = 48 kPa) with a thickness of H = 1.5 mm. The Si NM with a thickness h_{Si} = 80 nm is along the <110> direction with doping concentration (p-type) of 9.7×10^{18} /cm^3, hence E_{Si} = 168 GPa, GF_{Si} = 112. The Si NM is sandwiched between two identical polyimide (E_{PI} = 2.5 GPa) layers of total thickness h_{PI} = 2.4 mm. With above parameters, $\varepsilon_{\mathrm{avg}}/\varepsilon_{\mathrm{app}}$ is calculated to be 0.0045. Hence the effective gauge factor of the stretchable strain gauge is given by

$$\mathrm{GF} = \mathrm{GF}_{\mathrm{Si}}\frac{\varepsilon_{\mathrm{avg}}}{\varepsilon_{\mathrm{app}}} = 112\times0.0045 = 0.5 \quad \text{(S2),}$$

which is in good match with the experimental measurement (Figure 1.9b).

.

FEM of 3D thermal profile of the resistive heater: Finite element simulations have been performed via COMSOL 4.2 to determine the temperature distribution when the wearable heater is turned on to accelerate the transdermal drug delivery. The skin is modelled as a multilayer substrate with different thermal properties in each layer as illustrated in Supplementary Fig. 1.15a. Thickness (h), heat capacity (C), heat conductivity (k), density (ρ), blood perfusion rate (ω_b) and metabolic heat generation (Q) of each skin layer used in our model are given in Table S1.

	H (mm)	C (J kg^{-1} K^{-1})	K (W m^{-1} K^{-1})	ρ (kg m^{-3})	ω_b (s^{-1})	Q (W m^{-3})
Epidermis	0.1	3589	0.235	1200	0	0

Papillary dermis	0.7	3300	0.445	1200	0.0002	368.1
Reticular dermis	0.8	3300	0.445	1200	0.0013	368.1
Fat	2	2674	0.185	1000	0.0001	368.3
Muscle	8	3800	0.51	1085	0.0027	684.2

Table S1. Normal themophysical property values and layer thicknesses of the skin.

The governing equation of the heat transfer in each skin layer is:

$$\rho C \frac{\partial T}{\partial t} = k\nabla^2 T + \rho_b C_b \omega_b (T_b - T) + Q \quad \text{(S3)},$$

where $\rho_b = 1060\ kg/m^3$ and $C_b = 3770\ \mathrm{J/kg}\ m^3$ represent the mass density and the heat capacity of blood, respectively. As for the skin patch and the PDMS encapsulation, there is no blood perfusion or heat source. Therefore, equation (S3) decays to the basic heat transfer model in solids:

$$\rho C \frac{\partial T}{\partial t} = k\nabla^2 T \quad \text{(S4)},$$

with material properties listed in Table S2. The Joule heating model for the heater is given by

$$\rho C \frac{\partial T}{\partial t} = k\nabla^2 T + \sigma(\nabla V)^2 \quad \text{(S5a)},$$

and

$$\varepsilon_0 \varepsilon_r \frac{\partial}{\partial t}(\nabla^2 V) = -\sigma \nabla^2 V \quad \text{(S5b)},$$

where V is the electrical potential, σ and ε_r denote the electrical conductivity and the relative permittivity of the heater material, respectively. The heater properties listed in Table S2 are calibrated using the experimental results given in Fig. 1.13b, which shows the surface temperature distribution of the heater fabricated on a glass slide obtained from an infrascope. If DC power is supplied, $\partial V / \partial t = 0$.

	h (mm)	C (J kg^{-1} K^{-1})	K (W m^{-1} K^{-1})	ρ (kg m^{-3})	σ (S m^{-1})	ε_r
PDMS encap.	0.1	1200	0.17	965	-	-
Heater	0.05	129	317	19.3×10^3	1.395×10^7	1
Skin patch (PU)	0.4	3100	0.2	1100	-	-

Table S2. Thermo-physical property values of PDMS capsulation, heater and skin patch.

Skin is considered infinitely large such that open boundary conditions are applied to lateral surfaces. Temperature at the bottom surface of muscle layer is set to equal the core temperature of T_b = 37 °C. Convective cooling between the surface of the PDMS encapsulation layer and the environment is taken into consideration as well as the effect of the surface-to-ambient radiation. The environmental temperature is measured to be 15 °C. By applying the Joule heating model, equation (S5), in the heater and the heat transfer model, equations (S3) and (S4), in other parts, we can simulate the heat generated in the heater due to Joule effect being transferred through the skin patch to the skin in both transient and stationary states. The stationary state can be simply degenerated from equation (S3) by setting $\partial T / \partial t = 0$. Supplementary Figure

1.15b displays the 3D temperature distribution of the skin in stationary state. The maximum temperature at the patch-skin interface is 49.2 °C in the stationary state when the heater is supplied with a power of 0.23 W. Figure 1.13c displays the 3D temperature distribution after 20 minutes heating using the transient model and Fig. 1.13g plots the temperature profile as a function of time. The red curve shows the maximum temperature in the heater which is located at the top surface of the patch, while the orange curve represents the maximum temperature at the patch-skin interface. As we can see from the plot, after the skin patch being heated for 10 minutes, the temperature in the patch/skin interface reaches a plateau and then increases slowly as heating time increases (less than 0.5 °C/min). If we set the safe temperature of the human skin (the temperature at the bottom of epidermis layer) to be 45 °C, we can keep supplying power to the heater for 20 minutes without burning the skin. The blue curve also shows the diffusivity of the drug for the transdermal drug delivery, which increases exponentially as the temperature increases.

Diffusion of Rhodamine B dyes into the pig skin as a simulated transdermal drug delivery: Rhodamine B dyes (≥95%, Sigma Aldrich, USA) are loaded on m-silica NPs, which are transfer-printed to the hydrocolloid side of the skin patch. The skin patch is applied to the prepared pig skin (size of 1.5

cm × 1.5 cm). Two groups of samples are prepared. One group is placed under the room temperature (25 °C) while the other group is continuously heated at 40 °C up to 60 minutes. Then, pig skins of each group are put into the freezer (-80 °C) for 20 minutes to terminate the diffusion of Rhodamine B dyes. The specimens are frozen in optimal cutting temperature (OCT) compound (Leica, 3801480, Nussloch, Germany) at -80 °C. Then the frozen samples are sectioned into 15 μm-thick slices by using a Cryostat Cryocut Microtome (Leica, CM1510S, Nussloch, Germany). The diffusion depth of dyes into the pig skin samples are measured with a fluorescence microscope (Nikon, Eclipse Ti, Tokyo, Japan).

Flexible wiring that connects devices to external equipment: For the operation of the power supply and the control of the multifunctional wearable system, the external equipment is connected through flexible cables (anisotropic conductive films, ACFs). Several previous reports[3,4] have shown the ACF connection is robust and reliable even under severe mechanical deformations. ACF cables connect the proposed system to external equipment (data acquisition system and parameter analyser) through the custom made PCB board. A custom-made Labview-based software controls the data acquisition system and the general purpose interface bus (GPIB) with the parameter analyser.

Synthesis of Au NPs: Au NPs are prepared via modification of previously reported procedures[5]. In the typical synthesis, 0.4 g of $HAuCl_4 \cdot 3H_2O$ (99.9%, Strem, USA), 10 mL of oleylamine (Acros, 90%, USA), and 30 mL of 1-octadecene (90%, Sigma Aldrich, USA) are mixed in a 50 mL glass vial at the room temperature. The vial is placed on an oil bath and heated up to 90 °C. The solution is heated for 2 hours, and then the NPs are precipitated and washed with ethanol twice, followed by centrifugation. The precipitated NPs are redispersed with 5 mL of chloroform.

Characterisation of Au NPs: The samples for the TEM analysis are prepared by dropping a solution containing Au NPs on the surface of a copper grid coated with amorphous carbon film. The TEM images are collected on a JEM-2010 (JEOL, Japan) electron microscope operated at an accelerating voltage of 200 kV. The UV-Vis absorption spectra are taken with a Cary V-550 UV-VIS-NIR (Agilent, USA) spectrophotometer.

Langmuir-Blodgett assembly of Au NPs: Oleylamine-capped Au NPs are dispersed in chloroform (50 mg/mL). This solution is dropped onto the water sub-phase of a Langmuir-Blodgett trough (IUD 1000, KSV instrument, Finland). After the evaporation of the solvent, the surface layer becomes compressed by the mobile barriers (5 mm/min). After a surface pressure of 30 mN/m is achieved, the Au NPs are deposited onto the substrate by lifting it up and dipping down at 1 mm/min.

Measurement of I-V curves during mechanical stretching experiments: Stretching experiments are performed with an automatic stretching stage, which can apply tensile or compressive strains in the *x* and *y* directions. With the edges of the electronic patch clamped to the stage, the electrical measurements are performed with the probe station and parameter analyser (B1500A, Agilent, USA), while generating tensile/compressive deformations.

Synthesis of mesoporous silica (m-silica) NPs: Functional molecules, i.e. drugs, can be loaded into the m-silica NPs for therapeutic applications. Monodisperse m-silica NPs are synthesised using the previously reported method[6]. NaOH (0.35 mL, 2 M, 98%, Sigma Aldrich, USA) is added to 50 mL of cetyltrimethylammonium bromide (CTAB, > 99%, Acros, USA) solution

(100 mg in 50 mL of water). The mixture is heated to 70 °C, and then 0.5 mL tetraethylorthosilicate (TEOS, 98%, Acros, USA) is added. After 1 minute, 0.5 mL of ethyl acetate (99.5%, Samchun, Korea) is added, and the resulting mixture is stirred at 70 °C for 30 s and then aged for 2 h. The resulting precipitate is collected by centrifugation and washed with copious water and ethanol. Finally, the pore-generating template, CTAB, is removed by refluxing in acidic ethanol solution.

Characterisation of m-silica NPs: A JEM-2010 transmission electron microscope (JEOL, Japan) is used for transmission electron microscopy (TEM) analysis. N_2 adsorption and desorption isotherms are measured at 77 K using a Micromeritics ASAP 2000 gas adsorption analyser. The surface area and the total pore volume are determined using the Brunauer–Emmett–Teller equation and the Barrett-Joyner-Halenda method, respectively.

Loading of Rhodamine B onto m-silica NPs: As a drug diffusion model, Rhodamine B (≥95%, Sigma Aldrich, USA) is loaded on m-silica NPs. Rhodamine B solution (0.2 mL, 20 mg/mL in methanol) is adsorbed on the surface of m-silica NPs (0.15 g). Rhodamine B loaded in m-silica NPs are dried at room temperature.

Fabrication of structured PDMS stamp for transfer printing drug-loaded m-silica NPs: Negative photoresist (SU8-25, Microchem, USA) is spin-coated on the pre-cleaned and O_2 plasma-treated Si wafer. Photolithography is conducted on spin-coated SU8 to pattern holes that are 40 μm deep, 600 μm wide, and 1.46 mm spaced. Next, the SU8 mould is placed in a dish, which is heated on a 150 °C hot plate to promote the adhesion between the mould and the Si wafer. 10:1 PDMS (Sylgard 184A:Sylgard 184B, Dow Corning, USA) is then poured into the dish. After 24 h, the cured structured PDMS stamp with the micro-dot array is slowly detached from the SU8 mould (Supplementary Fig. S8b).

Transfer printing drug-loaded m-silica NPs onto skin patch: The drug-loaded (or dye-loaded) m-silica NPs solution is dropped on the surface of the structured PDMS stamp. The stamp is dried for ~20 minutes. The dried dye-loaded m-silica NPs are transfer printed as a microdot array to the hydrocolloid side of the skin patch (Supplementary Fig. 1.14a).

Temperature distribution measurement of the heater by using an infrared camera: The wavy-patterned Cr/Au-based heater (10 nm/190 nm, line width of 300 μm, 95.9 Ω) on a 1 mm-thick slide glass is connected to the power source (12 V, 1.5 W) under 15 °C surrounding temperature. The time-dependent thermo-grams are captured by the thermographic camera (320×240 pixels, IRE Korea, Korea), and the maximum temperature of the heater is plotted.

Fabrication and electrical measurement of MINIM (Al/TiO_2 NM-Au NPs-TiO_2 NM/Al) memory on the wearable skin patch: The schematic description of fabrication processes is shown in Supplementary Figure 1.2. Thin layers of poly(methyl methacrylate) (PMMA) (A11, Microchem, USA; ~1 μm, spin-coated at 3000 rpm for 30 s) and the precursor solution of polyimide (PI) (polyamic acid, Sigma Aldrich, USA; ~1.2 μm, spin-coated at 4000 rpm for 60 s) are spin-coated on a Si handle wafer (test grade, 4science, Korea). After curing the PMMA and PI at 200 °C for 2 h, Al, which serves as the bottom electrode (350 nm thick), is deposited via thermal evaporation and patterned by photolithography and wet etching. First TiO_2 NM (66 nm thick) is then RF magnetron sputtered (base pressure of 5×10^{-6} Torr, room temperature, deposition pressure of 5 mTorr, 20 sccm, 150 W RF power). Au NPs are separately synthesised and assembled on TiO_2 NM surface through the Langmuir-Blodgett assembly process (see Materials and Methods, SI). Then, second TiO_2 NM (66 nm thick) is deposited on Au NPs in the same way as the first TiO_2 NM. Al top electrode layer is deposited by the thermal evaporation. The layer is photolithographically patterned as well, completing the formation of serpentine-patterned resistive memory. Next, the PI precursor is spin-coated to place the active layer near the neutral mechanical plane, and the entire device structure is defined by the reactive ion etching (RIE) process using O_2 and SF_6 plasma (O_2 flow rate of 100 sccm, chamber pressure of 100 mTorr, 150 W RF power for 5 min; 50 sccm of SF_6 flow rate, 55 mTorr, 250 W RF power for 4 min 30 s). After the memory fabrication, the whole device on the Si wafer is dipped in the boiling acetone. Acetone removes sacrificial PMMA layer to release the PI-encapsulated device from the Si handle wafer. Then, the memory is picked up with the water-soluble tape (3M, USA). Device on the tape is transfer printed onto PDMS. De-ionized water dissolves the water-soluble tape to release the memory device, which is then transferred again to the skin patch (Derma-Touch, Kwang Dong Pharmaceutical Co., LTD. Korea). Electrical measurements are carried out with a parameter analyser (B1500A, Agilent, USA).

Fabrication of single crystal Si NM strain sensor on the skin patch: The fabrication starts with spin coating PMMA and PI films on a Si wafer. Photolithography and RIE (SF_6 plasma, 50 sccm, chamber pressure of 50 mTorr, 100 W RF power for 20 s) of boron-doped (doping concentration: ~$9.7\times10^{18}/\mathrm{cm}^3$) silicon-on-insulator (SOI) wafer form 80 nm-thick Si NMs, which are transfer-printed on the PI film. Microscope images are shown in Supplementary Fig. S6. Thermal evaporation is used for the following metallisation (Cr/Au, 7 nm/70 nm thick), and then the metal film is defined as specific patterns by photolithography and wet chemical etching. Next, the top PI layer is covered and the entire tri-layer (PI/device/PI) is patterned and etched by O_2 and SF_6 RIE. The entire device is released from the Si wafer by removing PMMA sacrificial layer with acetone. The transfer printing of the released device to the skin patch finalises the fabrication.

Custom-made data processing and storage system: The sensing and data storage process begins by capturing physiological strain signals using on-board sensors, which can be stored locally in cells of non-volatile memory (Supplementary Figure 1.11). For this system, a custom-made programme written by Lab View software (National Instruments, USA) is used to process and store the recorded data. For example, in the case of strain sensing for the tremor model in motion-related neurological disorders (Fig. 1.9d), the frequencies of tremor, recorded by the on-board strain gauge, are analysed and classified into four different bands (0–0.5, 0.5–0.7, 0.7–0.9, and >0.9 Hz) by the custom-made Lab View programme. The programme determines the appropriate compliance current and biasing voltage to write a specific two digit code ([00], [01], [10], and [11], which are pre-assigned to each band) to the on-board wearable memory cells under multi-level-cell operation through the probe station.

Fabrication of electro-resistive heater/temperature sensor on the skin patch: The skin-mountable heater is prepared by thermal evaporation of Cr/Au (10 nm/190 nm thick) through serpentine shape metal masks to define the serpentine shape on the non-adhesive side of the skin patch (opposite side of hydrocolloid). After wiring, the heater is encapsulated by the PDMS film. The same design and fabrication methods can be used for temperature sensors.

2.3 Result and Discussion

System description

Figures 1.1a and b show a schematic illustration and image of a representative wearable bio-integrated system, containing single crystal silicon (Si) NM (~80 nm) strain sensors, temperature sensor, TiO_2 NM (~66 nm) RRAM array, and electroresistive heaters. These multifunctional arrays of sensors and memory are heterogeneously fabricated and transfer-printed onto an elastomeric hydrocolloid patch (Derma-Touch, Kwang-Dong Pharmaceutical, Korea, Figure 1.2). To minimise bending-induced strains, the switching TiO_2 NM layer containing gold (Au) NPs are sandwiched by identical polyimide layers (~1.2 μm) to be located on the neutral mechanical plane (top left, Figure 1.1a)[6]. Thickness control of inorganic active layers within tens of nanometre scale further decreases flexural rigidity and induced strain[24]. Mesoporous silica (m-silica) NPs loaded with therapeutic drugs are transferred onto the hydrocolloid side of the skin patch (bottom middle, Figure 1.1a). Ultrathin serpentines and low modulus hydrocolloids together enable intimate mechanical contact with the skin[14]. The inset of Figure 1.1b highlights a 10 × 10 RRAM array in a serpentine network, which is integrated with sensors that transmit analogue outputs. Therapeutic drugs loaded on m-silica NPs are diffused into the dermis[25], in which the diffusion rate is controlled by the temperature of the hydrocolloid elastomer which is modulated by the heater. Temperature sensors offer *in situ* temperature feedbacks to alert skin burns.

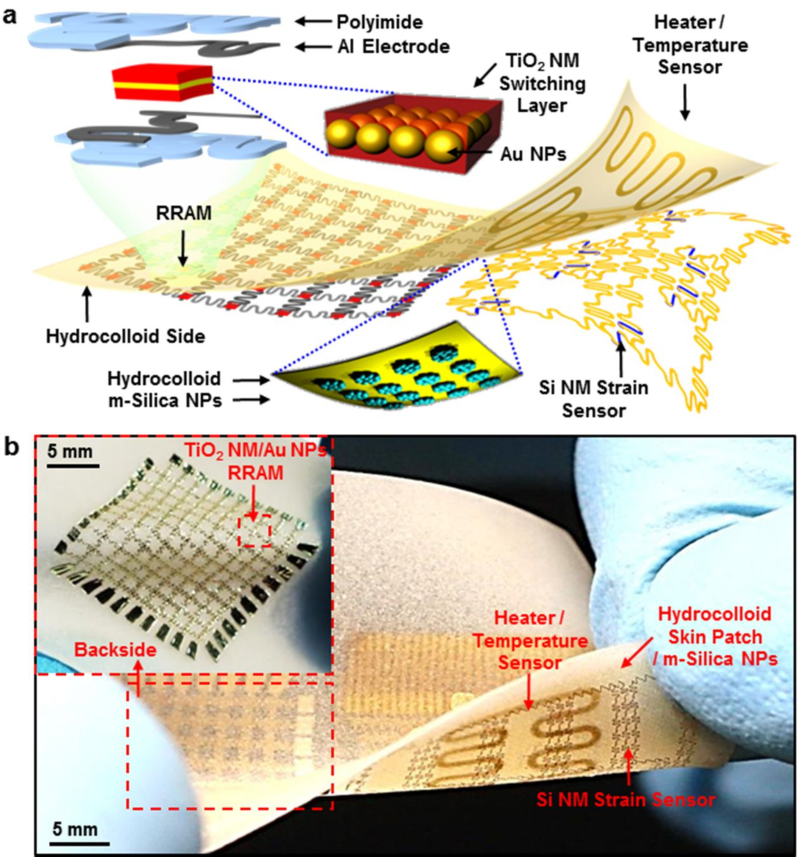

Figure 2.1 Wearable electronic patch composed of data storage modules, diagnostic tools, and therapeutic actuating elements. a, Wearable memory array consisting of a TiO_2 NM-Au NPs-TiO_2 NM switching layer and Al electrodes (top left inset shows layer information). The memory array was transfer printed on the bottom side of an elastomeric hydrocolloid skin patch. The electro-resistive heater/temperature sensor is fabricated on the top-side of the patch and Si strain sensor is on the opposite side. M-silica NPs array is

transfer-printed on the hydrocolloid side of the patch. **b,** Corresponding image of Fig. 1a, showing the wearable biointegrated system. Inset shows the wearable 10 × 10 RRAM array on the hydrocolloid side of the patch.

Integration of nanoparticles

The fabrication process (Figure 1.2) begins with the formation of TiO_2 NM on aluminum (Al) electrodes[26]. The Langmuir-Blodgett (LB) assembly process of uniform-sized Au NPs (diameter of ~12 nm)[27,28,29] on TiO_2 NM ensues (Figure 1.3a). Figures 1.3b-c shows images of the Langmuir-Blodgett process (Figure 1.3b, dipping and Figure 1.3c, pulling) and transmission electron microscope (TEM) images of assembled 1-layer (Figure 1.3d) and 3-layers Au NPs (Figure 1.3e). The number of assembly layers can be controlled by the number of dipping/pulling cycles[30]. Instead of Au NPs layers, self-assembled monolayer (SAM; stearic acid) can be coated to check the ligand effect on the memory performance (Figure 1.3a, 1.5). Cross-sectional scanning TEM (STEM) and TEM images of fabricated devices are shown in Figure 1.3f-h. Metal-insulator-SAM-insulator-metal (MISIM. Figure 1.3f), metal-insulator-NP-insulator-metal (MINIM, Figure 1.3g) with 1-layer-Au NPs (~12 nm), and MINIM with closely-packed 3-layers-Au NPs (~26 nm, Figure 1.3h) are represented, respectively. Energy-dispersive X-ray spectroscopy (EDS) profile of cross-section also confirms the thickness of 3-layers-Au NPs (Figure 1.3i). The closely-packed monolayer assembly in LB assembly process plays an important role in the device-to-device uniformity in a matrix configuration, as well as in the precise thickness control of multiple monolayers[27].

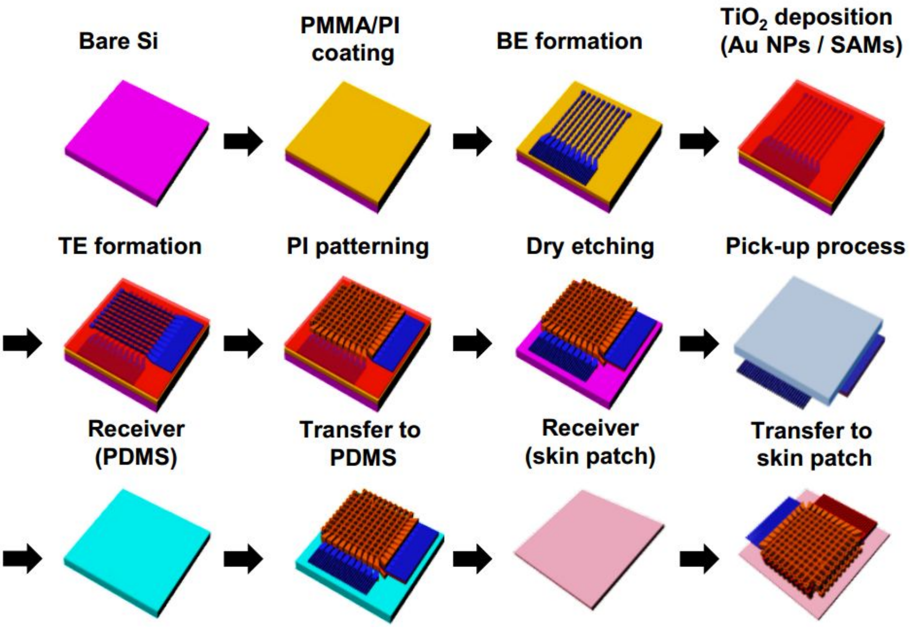

Figure 2.2 Schematic illustration of the operation process of the wearable bio-integrated system: wearable strain sensor detects movement disorders, the recorded data are stored in onboard memory modules, diagnostic patterns are analyzed on the basis of the stored data stream, thermal actuators apply heat to drug-loaded m-silica NPs, drugs are diffused transdermally, and movement disorders can be treated.

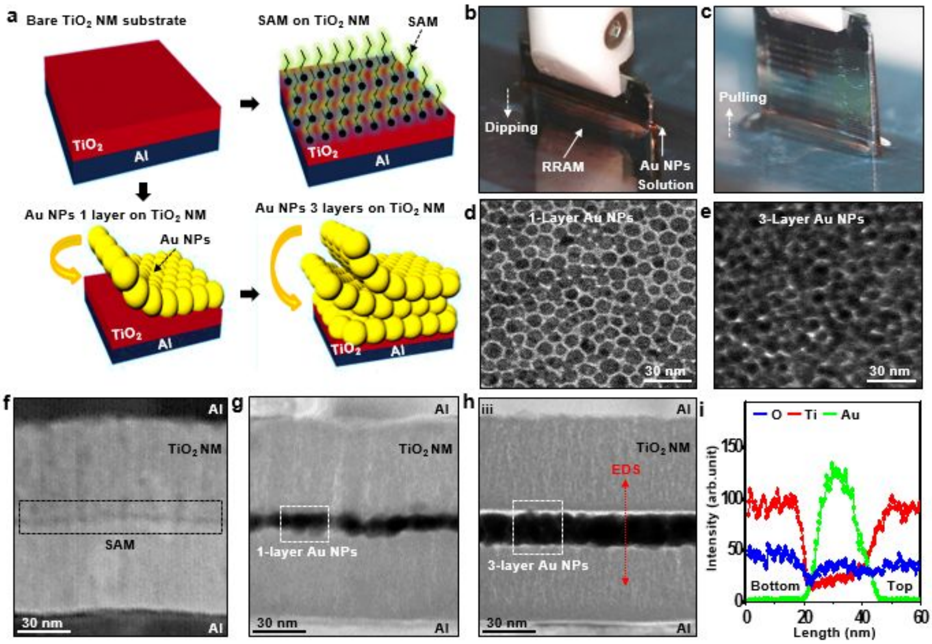

Figure 2.3 Langmuir-Blodgett assembly and SAM functionalization process. **a,** Schematic diagram for Langmuir-Blodgett assembly and SAM functionalisation. Au NPs are coated onto the switching TiO_2 NM via the Langmuir-Blodgett assembly process. The number of Au NP layers ranges from one to three. **b,** Images of Langmuir-Blodgett assembly process during dipping and **c,** pulling. **d,** Top-view TEM Images of 1-layer-Au NPs and **e,** 3-layers-Au NPs. **f,** Cross-sectional scanning TEM (STEM) image of MISIM. **g,** Cross-sectional TEM images of MINIM of 1-layer-Au NPs and **h,** MINIM of 3-layer-Au NPs. **i,** Energy-dispersive X-ray spectroscopy profile showing the thickness of 3-layers-Au NPs in MINIM.

Characterization of RRAM

To characterise electrical performance, we collected bipolar current – voltage (I-V) curves for the metal-insulator-metal (MIM), MISIM, and MINIM structures (Figure 1.4a). The inset in Figure 1.4a illustrates biasing sequences. The initial states are in the high-resistance state, while the application of negative voltage ("set") causes a shift to low-resistance state. Positive voltage ("reset") then switches the structures back to high-resistance state. I-V characteristics of MIM and MISIM are almost identical; while the incorporation of 1-layer-Au NPs in TiO_2 NM layer decreases the set and reset currents by nearly one order of magnitude relative to those of MIM. The current levels are further reduced (by three orders of magnitude) in 3-layers-Au NP MINIM. These results imply that uniform assembly of Au NPs in the active layer plays a critical role in reducing power consumption, and stearic acid ligands have little effect on the current reduction. This low power consumption property is important for the long-term operation of wearable devices.

Figure 1.4b shows a schematic diagram of the low current switching due to Au NP-induced traps; details are in Experimental section. Figure 1.4c shows log I – log V curves highlighting the negative voltage regions. The conduction mechanism in MINIM is similar to that of MIM (slopes of both MIM and MINIM vary from ~1 to ~2, and >2 with increasing voltages), which follows the trap-controlled space-charge-limited-current (SCLC) theory[31,32]. Figure 1.4d shows I-V curves with different compliance currents for MIM (left) and MINIM (right). MINIM exhibits better on/off ratios than MIM and MISIM (Figure 1.6a) with compliance currents < 100 μA. The reliability (endurance and retention) of MINIM, MIM, and MISIM is shown in Figure 1.4e and 1.6b-c, respectively. The endurance is reliable with little degradation in consecutive sweeping over 100 cycles (Figure 1.4e, left) and the good retention up to 1000 seconds is confirmed at room temperature (Figure 1.4e, right). Figure 1.4f shows the cumulative probability plot of MIM and MINIM, which shows uniform switching of the array. Although the on/off ratio in the current RRAM demonstrations can be further improved, data storage in a 10 × 10 matrix configuration was effective. Further improvements can be achieved by incorporating high quality Al_2O_3 instead of native alumina layer, or by depositing additional metal (tungsten or nickel) layers between Al (top electrode) and TiO_2 NM[33]. Multi-level-cell operations indicate the multi-data storage in a single cell with discrete compliance currents that result in discrete resistance levels (Figure 1.4d). Different resistances enable multiple information to be stored in a single cell (Figure 1.4g). Multi-level-cell with current levels below -100 μA is performed in MINIM and data are conserved over 100 read operations.

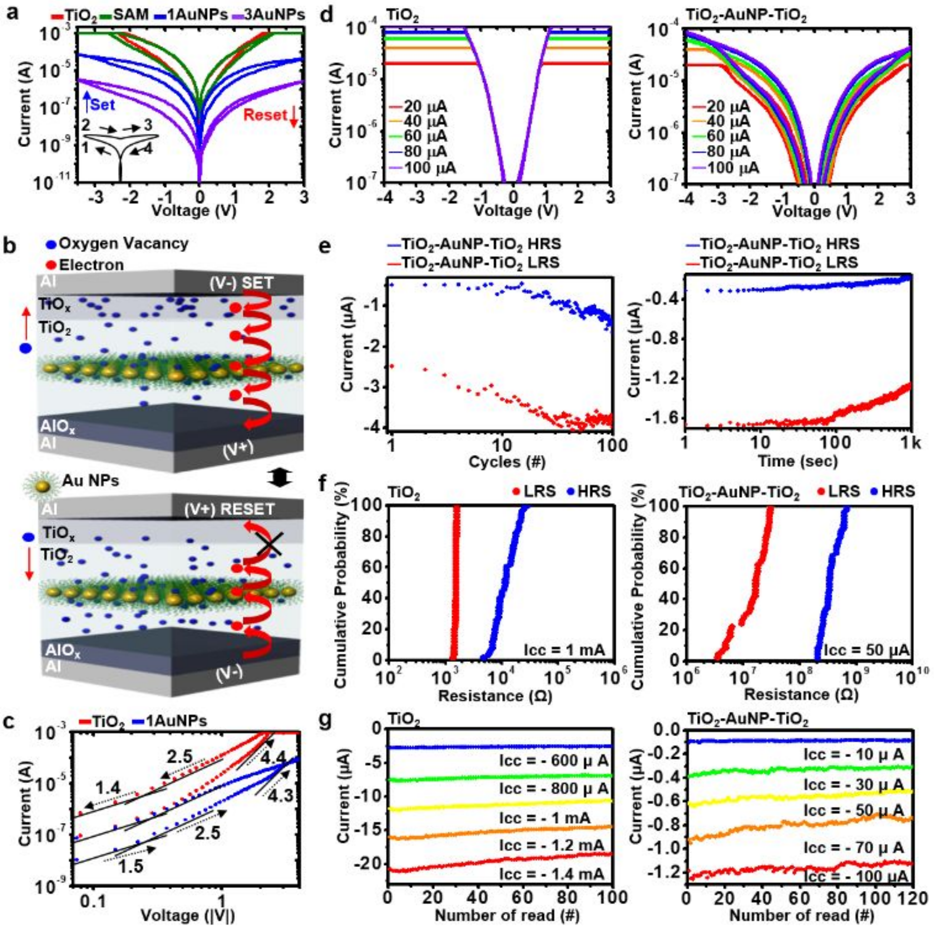

Figure 2.4 Electrical characteristics of RRAMs in MIM, MISIM and MINIM structures. a, I-V characteristics of the bipolar resistive switching of MIM, MISIM and MINIM structures. Inset shows the switching sequence. **b,** A schematic diagram of the low current resistive switching due to Au NP-induced

traps. The red curved arrows indicate electron flow in MINIM and the red flat arrows indicate oxygen vacancy flow. **c,** The double-logarithmic plots of I-V curve in MIM and MINIM. The numbers in the graph indicate the slope and the slope increases for larger voltages. **d,** I-V characteristics with compliance currents below ~100 μA in MIM and MINIM. **e,** Reliability test (endurance and retention; left and right, respectively.) of MINIM. Resistance values are measured at -0.5 V. **f,** Cumulative probability plot in MIM and MINIM, which shows the uniformity within the array**. g,** Multi-level-cell operation in MIM (left) and MINIM (right).

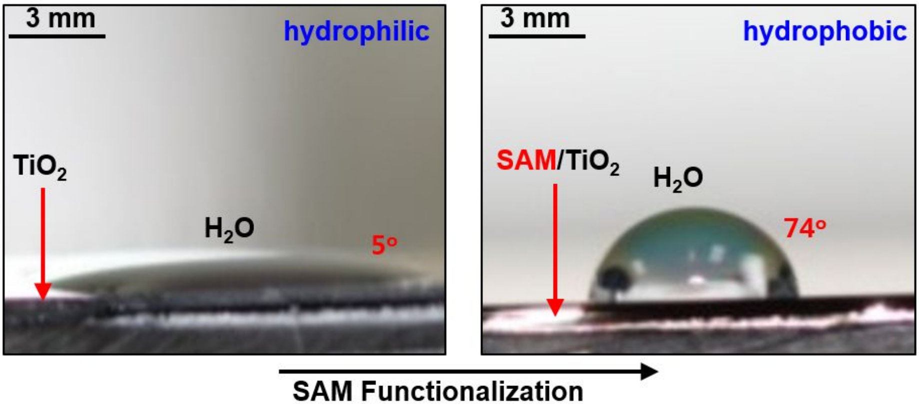

Figure 2.5 Contact angles of the native TiO_2 surface (left) and SAM-modified TiO_2 surface (right).

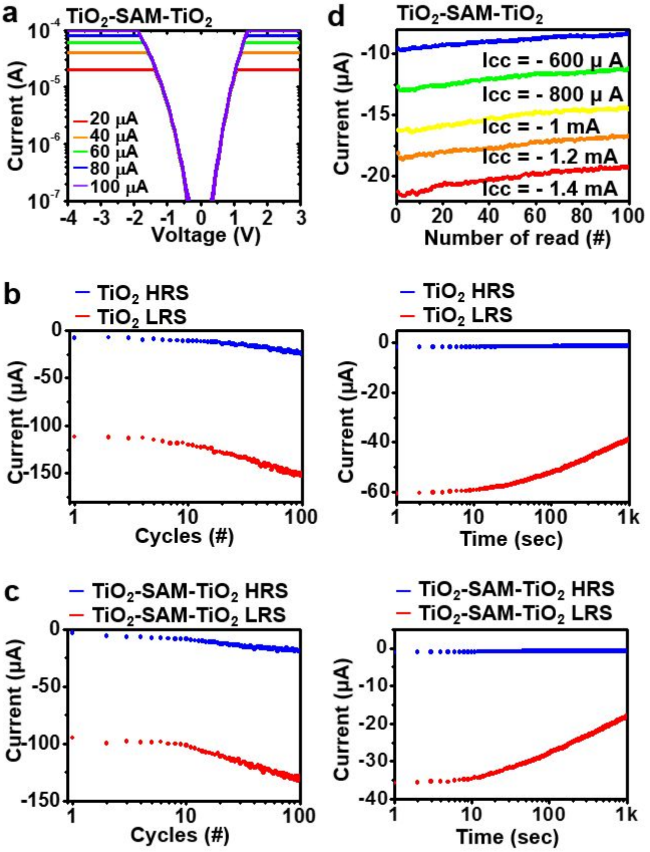

Figure 2.6 I-V characteristics and reliability data of the wearable memory. **a,** I-V characteristics of the MISIM structure with the compliance current < 100 atte**b,** Reliability (endurance and retention) measurement of MIM and **c,** MISIM structure. **d,** Multi-level cell (MLC) operation of the MISIM structure.

Reliability of wearable electronic system

The mechanical and chemical stability of wearable memory is demonstrated in Figure 1.7. Optical microscope images of the stretchable memory and corresponding characterisation data during stretching are shown in Figure 1.7a and b, respectively. When stretched up to ~25 % (the strain limitation of human epidermis is ~20 %[14]), the memory device shows stable electrical operation. The stretchable memory array can survive both bending (Figure 1.7c) and twisting (Figure 1.7d) and can conform to and deform with human skin (Figure 1.7e-h). Figure 1.7i and 1.8 show finite element modelling (FEM) results of the strain distribution of active layer (TiO_2 NM). By positioning the nanometre-thick membrane and NPs on the neutral mechanical plane and by using serpentine designs, the induced strain is kept below 0.1 % in switching layers and below 0.05% in the serpentine interconnects. The skin-conformable memory performs well with minimal signal degradation even after one thousands of stretching cycles (~30 % strain, Figure 1.7j). Figure 1.7k shows an image of the memory device immersed in phosphate buffered saline (PBS) solution without significant current variation (Figure 1.7l), indicating that the encapsulation layer is capable of blocking perspiration uptake.

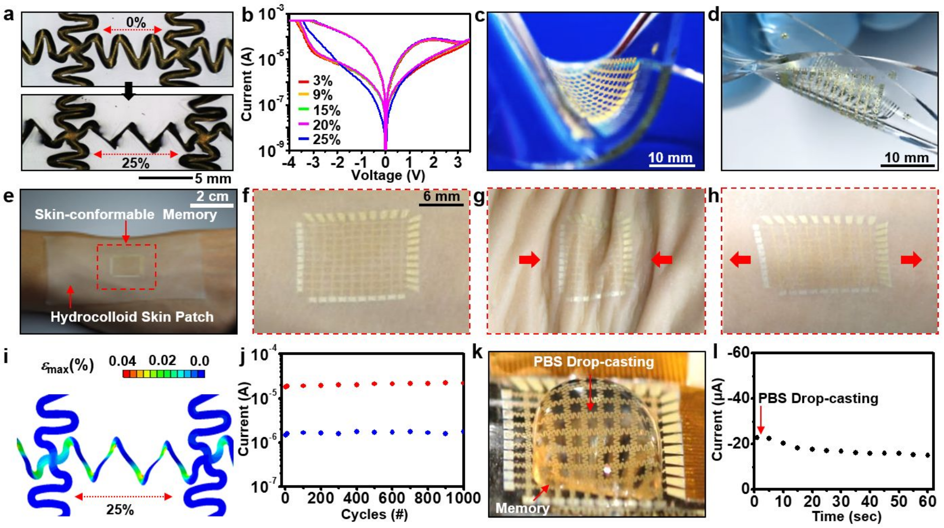

Figure 2.7 Skin-conformable RRAM array with mechanical stretchability and chemical stability. a, Microscope image of stretched memory (~25%) on the PDMS. **b**, I-V characteristics of the stretched memory at different strains (3% ~ 25%). **c**, Stretchable RRAM array in bent state, **d,** and twisted state. **e,** Skin-conformable memory devices on wrist and **f,** magnified views under no strain, **g,** compression, **h,** and tension. The red arrows indicate the direction of the strain. **i,** FEM of strain distribution in the stretched RRAM. **j**, Resistance change between low-resistance state (LRS, red dot) and high-resistance state (HRS, blue dot) at read voltage of -0.5 V during 1000 stretching cycles (~30%). **k**, Water-proof test under phosphate buffered saline (PBS) solution **l,** and read current.

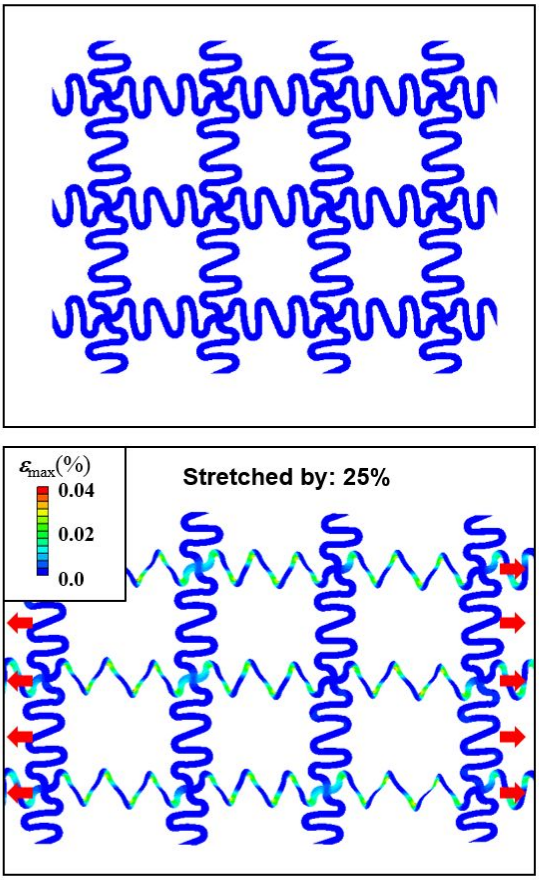

Figure 2.8 Finite element modelling (FEM) analysis of the strain distribution in active layer (TiO_2 NM) under ~25% external strain.

Recording muscle activity

Figure 1.9a shows an array of stretchable strain sensors based on Si NM (inset and Figure 1.10) as a representative example of wearable sensors in conjunction with collocated memory. The strain gauges have an effective gauge factor of ~0.5 (Figure 1.9b), consistent with gauge factor estimates derived analytically (see Experimental section). Because of the ultrathin serpentine interconnects, sensors conform well to skin during repeated exposure to tension and compression on human wrist (Figure 1.9c). This particular demonstration emulates tremor modes that manifest in epilepsy[2] and Parkinson's disease [3], which drive hand shaking at different frequencies (Figure 1.9d). The different tremor frequencies serve as a major tracking factor to monitor and diagnose these movement disorders. A data registering scheme is described in Figure 1.11, where the data captured from the movements is stored in separate memory cells every 10 seconds, using custom-made software programme. Representative frequencies corresponding to different frequency bands (0–0.5, 0.5–0.7, 0.7–0.9, and >0.9 Hz) are stored as four different levels (Figure 1.9e) on the basis of multi-level-cell operation (Figure 1.9g) of MINIM wearable memory. The written data are then read every 0.5 second, allowing physicians to monitor patient health conditions, analyze patterns and diagnose Figure 1.12.

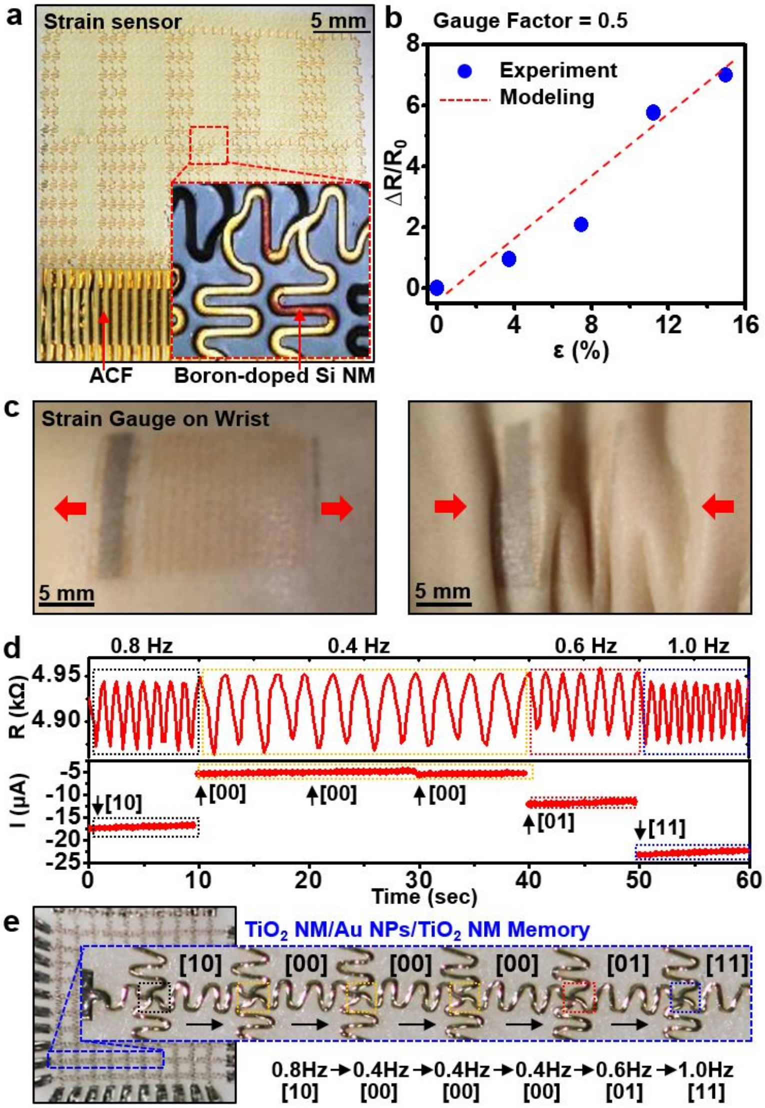

Figure 2.9 ***In-vivo* motion detection and data storage test. a,** Images of Si NM strain sensor. Boron-doped Si NM is positioned along x- and y-axis (inset). **b,** Percentage change in resistance versus strain plot for the calculation of gauge

factor. **c,** Images of strain measurement on the wrist under tension and compression. The red arrows indicate the direction of the strain. **d,** Plot of the time-dependent change in resistance in the Si strain gauge caused by simulated hand tremors at frequencies of 0.8, 0.4, 0.6, and 1 Hz (top). Plot illustrating the multi-level-cell operation of memory cells (bottom). **e,** The frequency of strain data is monitored and classified into 4 levels: [00], [01], [10], and [11]. The dotted rectangles with black, orange, red, and blue colours correspond to 4 levels: [00], [01], [10], and [11], respectively. Data are written on a MINIM memory cell and read repeatedly for 10 s.

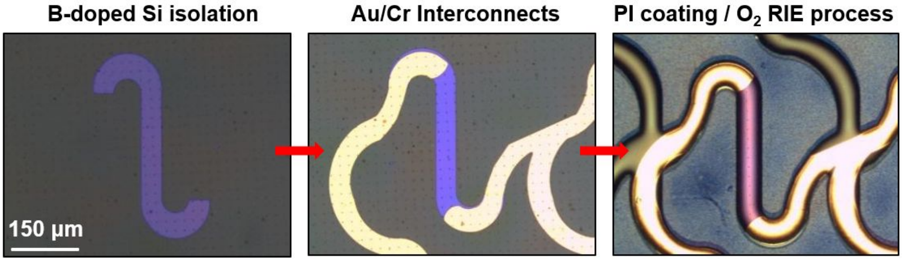

Figure 2.10 Microscope images of fabrication steps of the stretchable Si strain sensor.

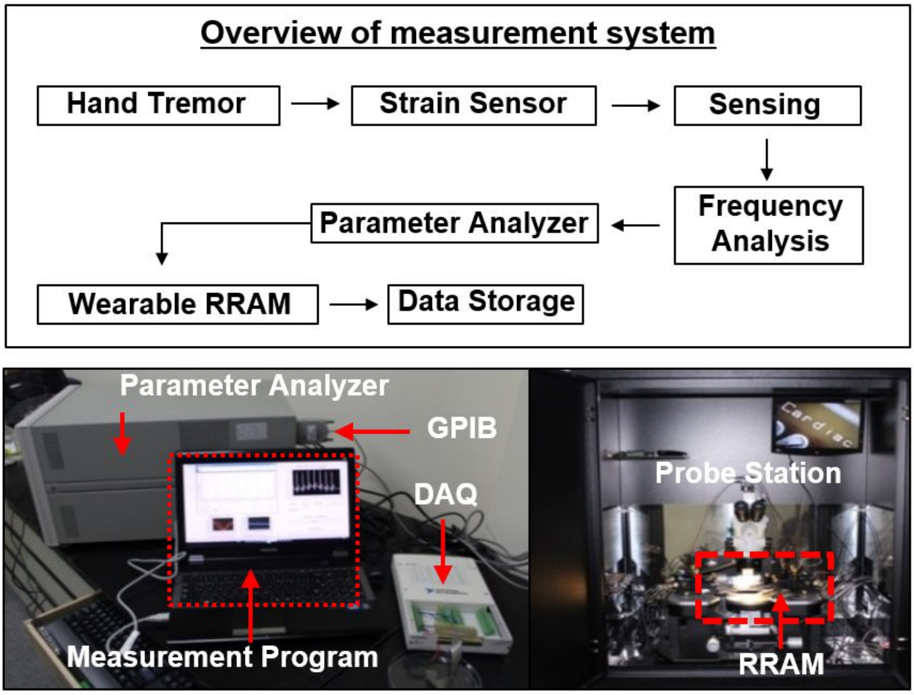

Figure 2.11 Overview of the custom-made data processing and storage system.

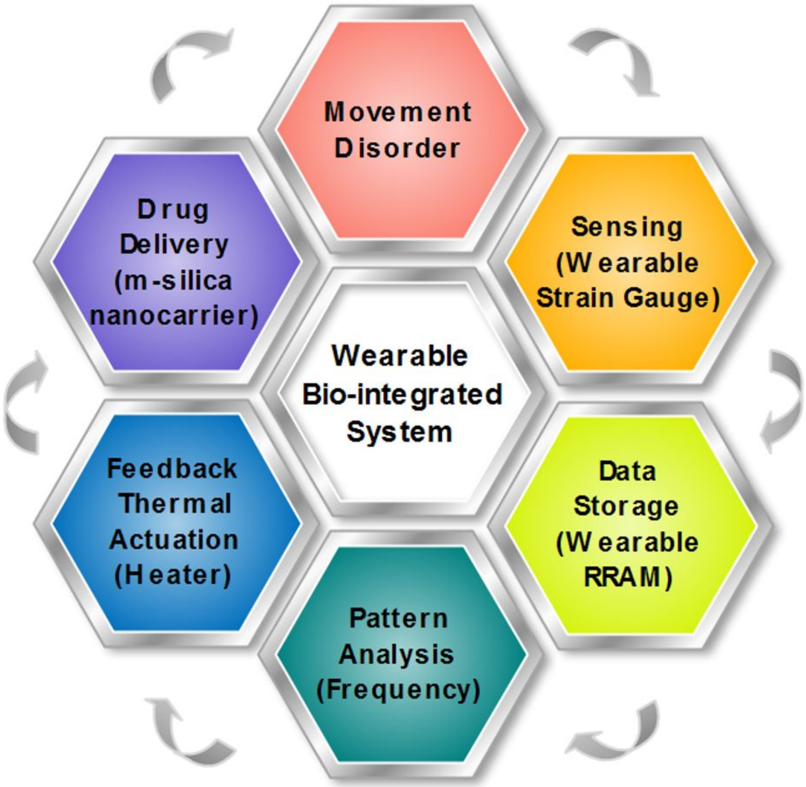

Figure 2.12 Schematic illustration of the operation process of the wearable bio-integrated system: wearable strain sensor detects movement disorders, the recorded data are stored in onboard memory modules, diagnostic patterns are analyzed on the basis of the stored data stream, thermal actuators apply heat to drug-loaded m-silica NPs, drugs are diffused transdermally, and movement disorders can be treated.

Controlled delivery of therapeutic agents

A compelling application for the sensing and data storage is to use the stored information to trigger the onset of therapy. One possible mode of use is to feed recorded data through a control circuit that recognises the characteristic patterns of disease, which in turn, triggers/controls the drug release (Figure 1.12, 1.13a,). We employ mesoporous silica nanoparticles (m-silica NPs) as a drug containing and delivery vehicle[34,35] (Figure 1.13d-f) and an electroresistive heater/temperature sensor as diffusion accelerating/temperature monitoring element (Figure 1.13b, c, g, h) for controlled transdermal drug delivery (Figure 1.13i)[25]. M-silica NPs loaded with drugs are transfer-printed on the sticky side of the patch (Figure 1.13d, 1.14a) by using structured polydimethylsiloxane (PDMS) stamp (Figure 1.14b). M-silica NPs containing nanopores (Figure 1.13e) have large surface area for drug adsorption (Figure 1.13f). Figure 1.13b shows the thermal gradient image (infrared camera measurements) of an electro-resistive heater on the patch surface. Figure 1.13c shows the corresponding FEM analysis emphasising the 3D thermal profile of the device on multilayered human skin, demonstrating the delivery of sufficient heat to the skin and NPs (Figure 1.15). The heat generated by the heater degrades the physical bonding between NPs and drugs and thereby pharmacological agents loaded in NPs are diffused transdermally. FEM simulation confirms the increase of diffusion rates by the heating (Figure 1.13g). The sensitivity of temperature sensor (Figure 1.13h) is ~0.086 Ω/ºC, which is similar to previous reports of thermal monitoring[36]. Further improvement in sensitivity can be achieved by optimising materials and designs of the thermistor. Also the high uniformity of the temperature sensor can be obtained by the precise control of metal evaporation process. The temperature sensor can monitor the maximum temperature on the epidermis. The skin can be protected from getting burnt (< 43 ºC) by a control unit programmed by the Labview software. The transdermal drug delivery can be indirectly visualised by fluorescence microscope imaging of the diffused dye (Rhodamine B) into the pig skin at room (25 ºC, Figure 1.13i-j) and elevated (40 ºC, Figure 1.13k-l) temperature. The penetration depth of the dye into the pig skin at room temperature is shallower than that at elevated temperature, implying the accelerated diffusion by the thermal actuation.

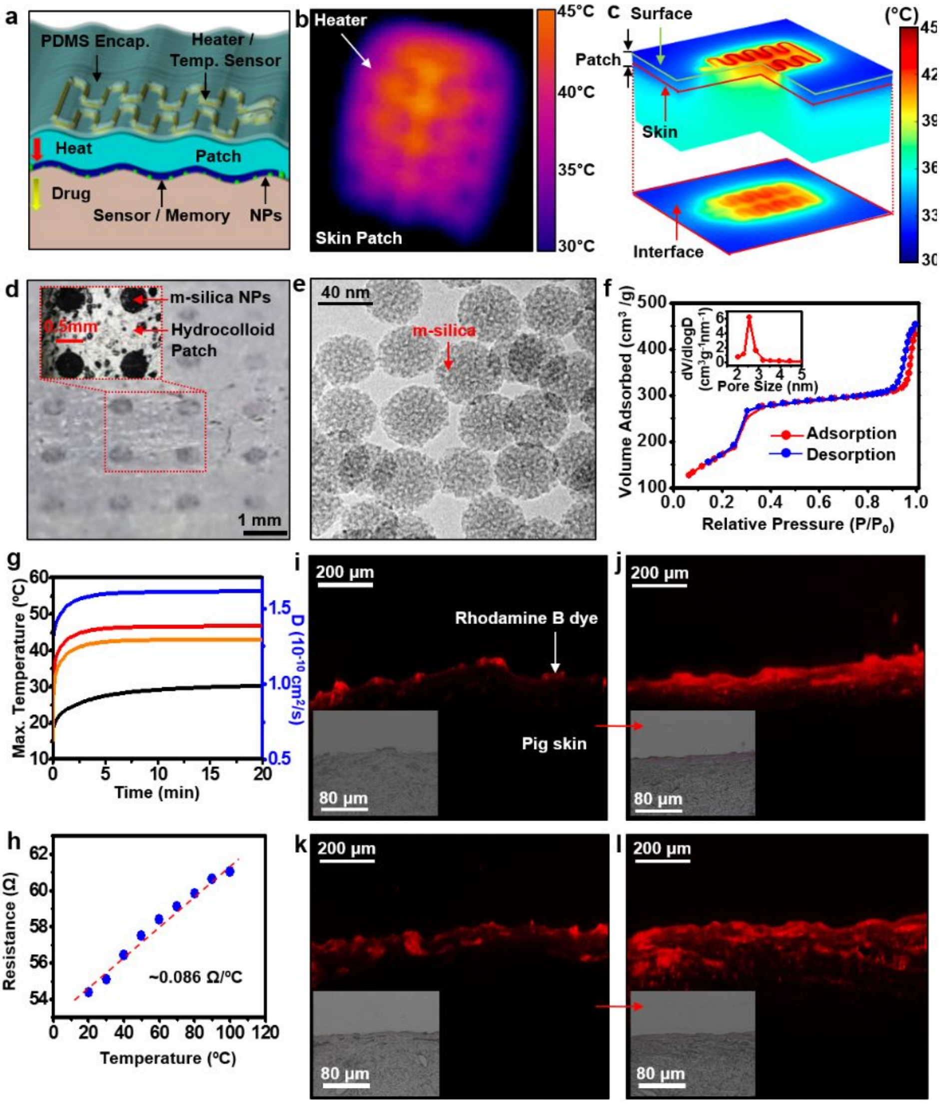

Figure 2.13 Controlled transdermal drug delivery by using the electroresistive heater and drug-loaded m-silica NPs. a, Schematic illustration of controlled transdermal drug delivery from hydrocolloid and m-silica NPs by the thermal actuation. **b**, Temperature distribution measurement of

the heater on the skin patch by using an infrared camera. **c**, FEM of the 3D thermal profile of a heater on the patch and at the interface between the patch and the human skin. **d**, High resolution camera image showing an array of m-silica NPs. Inset shows a microscope image. **e**, TEM image of m-silica NPs. **f**, Surface area calculation through the measurement of N_2 adsorption and desorption isotherms at 77K. The inset shows the pore volume of them-silica NPs by using Barrett-Joyner-Halenda (BJH) method. **g**, Plots of maximum temperature as a function of time on the heater surface (red), on the interface between the skin and patch (orange), and on the interface without heating (black). The right y-axis shows the diffusion coefficient exponentially increasing with the temperature (blue). **h**, Characterisation plot of the temperature sensor. The dashed red line implies linear approximation of the blue data points. **i**, Cross-sectional fluorescence images of the pig skin before the diffusion of Rhodamine B dyes at 25 ºC and **j,** after the diffusion. **k,** Cross-sectional fluorescence images of the pig skin before the diffusion of Rhodamine B dyes at 40 ºC and **l,** after the diffusion.

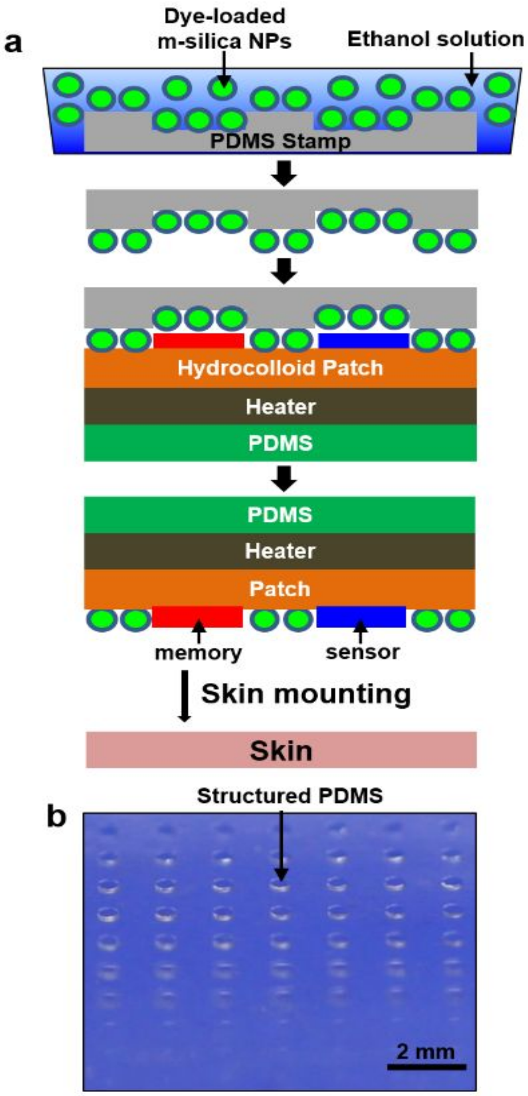

Figure 2.14 a, Schematic overview of transfer printing process of drug-loaded m-silica NPs, sensors and memory devices. **b,** Image of the structured PDMS stamp used in the transfer printing process.

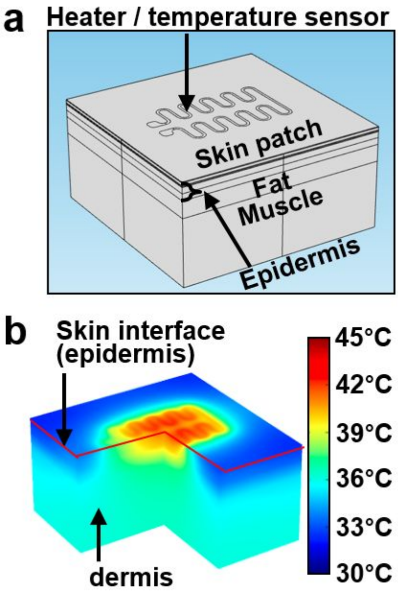

Figure 2.15 a, Schematic sectional view of the electronic patch mounted on the skin. **b,** FEM analysis of the temperature distribution at the skin/patch interface (on the skin).

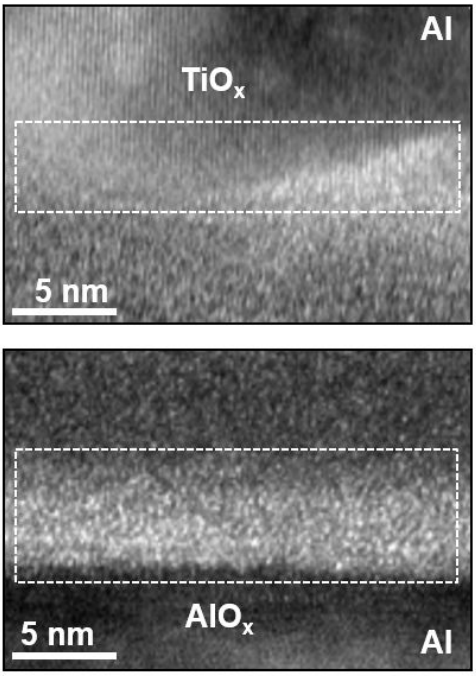

Figure 2.16 TEM images of switching layers: TiO_x between the top Al electrode and TiO_2 NM switching layer (top) and AlO_x between the bottom Al electrode and TiO_2 NM switching layer (bottom).

2.4 Conclusion

The materials, mechanics, and electronics strategies for wearable biomedical systems using stretchable designs and heterogeneous integrations of nanomembranes and nanoparticles provide opportunities for advanced diagnostics and drug delivery. This platform overcomes limitations of conventional wearable devices and has potential to improve compliance, data quality and efficacy of current clinical procedures. Analytical modelling and FEM analysis validate the mechanical, thermal, and kinetic functionalities of the individual components and lay the foundation for rationalised designs and analysis. Future work that enables complete wire-free devices can include energy storage units (e.g. battery or wireless power transmission), central control units (e.g. microprocessor), and additional wireless communication units as a stretchable format[18,36,37], along with the sensing, memory and therapeutic modules in the present work to realise the interactive and remote healthcare.

References

1. Lobodzinski, S. S. & Laks, M. M. New Devices for Very Long-Term ECG Monitoring. *Cardiol. J.* **2012**, 19, 210-214.
2. Stacey, W. C. & Litt, B. Technology insight: neuroengineering and epilepsy-designing devices for seizure control. *Nat. Clin. Pract. Neurol.* **2008**, 4, 190-201.
3. Lotharius, J. & Brundin, P. Pathogenesis of parkinson's disease: dopamine, vesicles and α-synuclein. *Nat. Rev. Neurosci.* **2002**, 3, 932-942.
4. Kringelbach, M. L., Jenkinson, N., Owen, S. L. F. & Aziz, T. Z. Translational principles of deep brain stimulation. *Nat. Rev. Neurosci.* **2007**, 8, 623-635.
5. Sekitani, T., Zschieschang, U., Klauk, H. & Someya, T. Flexible organic transistors and circuits with extreme bending stability. *Nat. Mater.* **2010**, 9, 1015-1022.
6. Kim, D.-H.*, et al.* Stretchable and foldable silicon integrated circuits. *Science* **2008**, 320, 507-511.
7. Sekitani, T.*, et al.* A rubberlike stretchable active matrix using elastic conductors. *Science* **2008**, 321, 1468-1472.
8. Kaltenbrunner, M.*, et al.* An ultra-lightweight design for imperceptible plastic electronics. *Nature* **2013**, 499, 458-463.

9. Kim, D. K., *et al.* Flexible and low-voltage integrated circuits constructed from high-performance nanocrystal transistors. *Nat. Commun.* **2012**, 3, 1216.
10. Viventi, J., *et al.* A conformal, bio-interfaced class of silicon electronics for mapping cardiac electrophysiology. *Sci. Transl. Med.* **2010**, 2, 24ra22.
11. Kim, D.-H., *et al.* Materials for multifunctional balloon catheters with capabilities in cardiac electrophysiological mapping and ablation therapy. *Nat. Mater.* **2011**, 10, 316-323.
12. Viventi, J., *et al.* Flexible, foldable, actively multiplexed, high-density electrode array for mapping brain activity in vivo. *Nat. Neurosci.* **2011**, 14, 1599-1605.
13. Khodagholy, D., *et al.* In vivo recordings of brain activity using organic transistors. *Nat. Commun.* **2013**, 4, 1575.
14. Kim, D.-H., *et al.* Epidermal electronics. *Science* **2011**, 333, 838-843.
15. Takei, K., *et al.* Nanowire active-matrix circuitry for low-voltage macroscale artificial skin. *Nat. Mater.* **2010**, 9, 821-826.
16. Chuan, W., *et al.* User-interactive electronic skin for instantaneous pressure visualization. *Nat. Mater.* **2013**, 12, 899-904.

17. Lipomi, D. J., *et al.* Skin-like pressure and strain sensors based on transparent elastic films of carbon nanotubes. *Nat. Nanotech.* **2011**, 6, 788-792.
18. Farra, R., *et al.* First-in-human testing of a wirelessly controlled drug delivery microchip. *Sci. Transl. Med.* **2012**, 4, 122ra121-122ra121.
19. Waser, R. & Aono, M. Nanoionics-based resistive switching memories. *Nat. Mater.* **2007**, 6, 833-840.
20. Kwon, D.-H., *et al.* Atomic structure of conducting nanofilaments in TiO_2 resistive switching memory. *Nat. Nanotech.* **2010**, 5, 148-153.
21. Borghetti, J., *et al.* `Memristive' switches enable `stateful' logic operations via material implication. *Nature* **2010**, 464, 873-876.
22. Sekitani, T., *et al.* Organic nonvolatile memory transistors for flexible sensor arrays. *Science* **2009**, 326, 1516-1519.
23. Kang, N.-G., *et al.* Structural and electrical characterization of a block copolymer-based unipolar nonvolatile memory device. *Adv. Mater.* **2012**, 24, 385-390.
24. Rogers, J. A., Lagally, M. G. & Nuzzo, R. G. Synthesis, assembly and applications of semiconductor nanomembranes. *Nature* **2011**, 477, 45-53.
25. Prausnitz, M. R. & Langer, R. Transdermal drug delivery. *Nat. Biotech.* **2008**, 26, 1261-1268.

26. Sungho, K. & Choi, Y.-K. A comprehensive study of the resistive switching mechanism in Al/TiO_x/TiO_2/Al-structured RRAM. *IEEE Trans. Electron Devices* **2009**, 56, 3049-3054.

27. Tao, A. R., Huang, J. & Yang, P. Langmuir-Blodgettry of nanocrystals and nanowires. *Acc. Chem. Res.* **2008**, 41, 1662-1673.

28. Talapin, D. V., Lee, J.-S., Kovalenko, M. V. & Shevchenko, E. V. Prospects of colloidal nanocrystals for electronic and optoelectronic applications. *Chemical Reviews* **2009**, 110, 389-458.

29. Lu, X., Tuan, H.-Y., Korgel, B. A. & Xia, Y. Facile synthesis of gold nanoparticles with narrow size distribution by using AuCl or AuBr as the precursor. *Chem. Eur. J.* **2008**, 14, 1584-1591.

30. Yamada, Y.*, et al.* Nanocrystal bilayer for tandem catalysis. *Nat. Chem.* **2011**, 3, 372-376.

31. Shang, D. S.*, et al.* Effect of carrier trapping on the hysteretic current-voltage characteristics in Ag $La_{0.7}$ $Ca_{0.3}$ MnO_3 Pt heterostructures. *Phys. Rev. B* **2006**, 73, 245427.

32. Kim, K. M., *et al.* A detailed understanding of the electronic bipolar resistance switching behavior in Pt/TiO_2/Pt structure. *Nanotechnology* **2011**, 22, 254010.

33. Jeong, H. Y., et al. Interface-engineered amorphous TiO_2-based resistive memory devices. *Adv. Funct. Mater*. **2010**, 20, 3912-3917.

34. Lee, J, E., *et al.* Multifunctional mesoporous silica nanocomposite nanoparticles for theranostic applications. *Acc. Chem. Res.* **2011**, 44, 893-902.

35. Peer, D.*, et al.* Nanocarriers as an emerging platform for cancer therapy. *Nat. Nanotech.* **2007**, 2, 751-760.

36. Kim, T.-i.*, et al.* Injectable, cellular-scale optoelectronics with applications for wireless optogenetics. *Science* **2013**, 340, 211-216.

37. Sekitani, T.*, et al.* A large-area wireless power-transmission sheet using printed organic transistors and plastic MEMS switches. *Nat. Mater.* **2007**, 6, 413-417.

Chapter 3. Stretchable Carbon Nanotube Charge-Trap Floating-Gate Memory and Logic Devices for Wearable Electronics

3.1 Introduction

Along with the increasing interests in wearable electronics, significant advancements have been achieved in technologies for flexible and stretchable devices, such as flexible displays,[1,2] skin-based electronics,[3-6] high-sensitivity deformable sensors,[7-11] wearable human-machine interfaces,[12-14] and compliant energy devices[15-19]. These unconventional electronic, optoelectronic, and energy devices are core components for next-generation wearable electronic systems. Although previous breakthroughs have dramatically advanced related technologies, current electronic devices still suffer from practical problems. One of the most significant concerns is the use of inorganic layers for the active channels and dielectric of conventional electronic devices which may incur mechanical cracks and/or breakdown in repetitive deformations and consequent accumulation of fatigues[4]. The mechanical mismatch between human tissues and inorganic semiconductors aggravates this problem, particularly in skin-based wearable devices.

Extensive research has been conducted to dissipate the induced strain in the channel and active regions, such as ultrathin thickness design approaches[20], neutral mechanical plane layouts[21,22], and stretchable interconnections[23-25]. More fundamental changes have been proposed to replace channel materials with soft ones, including graphene[26-28] and carbon nanotubes (CNT)[29-37]. Graphene may have issues in terms of the on/off ratio owing to its zero band gap, which is critical for digital circuits. Networks of semiconducting single-walled CNT (s-SWNT) are a promising candidate owing to their potential for high speed/performance electronics by the intrinsically high carrier mobility[38-43], although challenges in terms of device structures/designs, material optimization, and fabrication/integration strategies exist. Therefore, efforts to develop stretchable/wearable types of memory modules and other electronic device components for advanced electronic circuits/systems are important. Here, we present materials and device design/fabrication strategies for an array (17 × 15) of s-SWNT-based stretchable electronic devices consisting of capacitors, charge-trap floating-gate memory (CTFM) units, and logic gates (inverters and NAND/NOR gates). Detailed material, electrical, and mechanical characterizations and theoretical analysis in mechanics provide useful insights in the design and development of s-SWNT-based wearable electronic systems.

***The contents of this chapter were published in ACS Nano (2015, 9, 5585-5593)**

3.2 Experimental Section

Fabrication of s-SWNT-based wearable electronic devices: The detailed fabrication processes and materials used in the devices are described in the Results and Discussion section, supplemented by Figures 3.1, 3.2-3. Before the devices are transferred onto a human skin, the entire system is picked up from an SiO_2 temporary supporting substrate using water-soluble tape (3M, USA) and transferred onto a thin layer of polydimethylsiloxane ((PDMS), Dow Corning, USA). The water-soluble tape is dissolved using DI water to release the devices, which are subsequently transfer-printed on the skin.

Characterization of the device structures: The top-view images of the CTFMs, inverters, NAND/NOR gates, and capacitors are captured using an optical microscope (BX51 M, Olympus, USA). The density of the s-SWNT networks is examined using an atomic force microscope (Dimension Icon, Bruker, UK). The TEM images and the corresponding EDS data are taken using an electron microscope (JEM-2010, JEOL, Japan) operated at an acceleration voltage of 200 kV. For the cross-sectional analysis, the samples are cut using a focused ion beam (Quanta 3D FEG, FEI, USA) in the channel/trap region.

Characterization of the electrical properties: The *C*-*V* measurements are conducted at a 100-kHz frequency at ±10 V using a parameter analyzer (B1500A, Agilent, USA) equipped with an LCR meter and a probe station (MSTECH, Republic of Korea). The *I*-*V* curves are obtained using the same setup. The stretching tests are conducted using an automatic stretching stage that applies compressive and tensile strains in the *x* and *y* directions.

FEA of the CTFMs and inverters: Finite element simulations are used to analyze the strain distribution of the CTFMs and inverters during the stretching (Figures 3.13b and d) and bending tests (Figure 3.15b). The CTFMs and inverters are modeled using four-node composite shell elements. The devices/substrates are modeled using eight-node solid elements. We assume perfect bonding (no-slip condition) between the devices and substrates. To simulate stretching, stretching boundary conditions are applied at the bottom surface of the substrate. To simulate bending, rotation boundary conditions corresponding to the given radius of curvature are applied at the bottom of the substrate. The isotropic linear elasticity represents the behavior of the materials of the flash memory devices and inverters. The Young's moduli of the CNT, Au, Al_2O_3, SiO_2, and PI are 1 TPa, 77.2 GPa, 463 GPa, 73.1 GPa, and 2.5 GPa, respectively. The Poisson's ratios of CNT, Au, Al_2O_3, SiO_2, and PI are 0.22, 0.42, 0.22, 0.17, and 0.34, respectively. The incompressible neo-Hookean model is used to represent the substrate: $W = C_1(I_1 - 3)$ where W is the strain energy potential, I_1 is the first invariant of the left Cauchy-Green tensor, and C_1 (=3 kPa for the PDMS substrate) is a material parameter.

3.3 Result and Discussion

System description

Figure 3.1 left depicts a schematic illustration of the wearable array of s-SWNT-based (99.9%-sorted s-SWNT, NanoIntegris Inc., USA) electronic devices composed of capacitors, CTFMs/transistors, and digital circuit components. The circuit diagrams (top) and layer information of the CTFM (bottom) are shown on the right. The ultrathin (< ~3 μm) and stretchable system design enables conformal integration of electronics onto the human skin. For mechanical robustness, the entire system is sandwiched between polyimide (PI, Sigma Aldrich, USA; ~1 μm) ultrathin films. The detailed description of the fabrication processes and an exploded schematic illustration are shown in Figure 3.3, and the corresponding large-scale view in Figure 3.4. First, a PI layer (~1 μm) is spin-coated on a silicon oxide (SiO_2) wafer, followed by the deposition of Cr/Au (~5 nm/~50 nm) back-gate electrodes using thermal evaporation. All electrodes and charge-trap layers are formed using photolithography and lift-off techniques. After the deposition of a blocking oxide (B_{ox}) layer (~35-nm-thick aluminum oxide (Al_2O_3)) by plasma enhanced atomic layer deposition (PEALD), ~10 nm of gold (Au) is deposited for the charge-trap layer of flash memories. Two consecutive layers of tunneling oxides (Al_2O_3/SiO_2, ~5 nm/~3 nm) are deposited by PEALD (Al_2O_3) and e-beam evaporation (SiO_2). Even though the use of organic dielectric layers would have been advantageous in terms of mechanical flexibility than the chosen inorganic dielectrics, Al_2O_3 is used in this work due to its excellent thickness controllability and uniformity using PEALD, which in turn results in high performance of the CTFM devices. The top surface of SiO_2 is functionalized to form an amine-terminated surface by immersing it into a poly-L-lysine solution (0.1 wt%, aqueous solution; Sigma Aldrich, USA) for 5 min. Then, random networks of SWNTs (whose average diameter and length are 0.8 ~ 1.2 nm and 100 ~ 1,000 nm, respectively) are deposited by dipping them into an s-SWNT solution (0.01 mg/mL, aqueous solution) for a few hours, followed by thorough rinsing using deionized (DI) water and isopropanol alcohol[1]. After annealing in a globe box at 200 °C for 1 h, isolation of the oxide layers and formation via connections follow. The fabrication of the other electronic devices uses similar procedures. But other devices, such as transistors in the logic circuits, do not contain the Au charge-trap layers and fabricated by using different patterns. The entire process is completed by depositing source/drain electrodes (Cr/Au, ~7 nm/70 nm), spin coating the top PI layer (~1 μm), and patterning the final serpentine/island layout by using photolithography and dry etching. Such design of island arrays connected with serpentine-shaped interconnects, with the assist of neutral mechanical plane designs, successfully protected the channel, dielectrics, and contacts during different bending and stretching modes, as will be confirmed later in Figure 3.13.

Figure 3.2a represents high-resolution camera images of wearable s-SWNT electronic devices, consisting of CTFMs/transistors (10 × 15 array), inverters (1 × 15 array), NAND/NOR gates (2 × 15 array), and capacitors (4 × 15 array). The inset at the bottom left (black box) shows the conformal lamination on the skin during bending deformations. The inset at the top right (red-dashed box) confirms the conformal contacts of the array through magnified observation. The use of ultrathin PI films with serpentine structures, along with the van der Waals forces, successfully dissipates the induced strains during motions, and maintains intimate contacts. The detailed mechanical and electrical characterizations of these devices under reversible deformations with induced strains (~20%) are discussed later in Figure 13. Further deformations that can possibly occur during daily life activities are shown in Figure 3.2b. The devices show no delamination and/or mechanical fractures during poking, compression, and stretching (top, middle, and bottom of the figure, respectively).

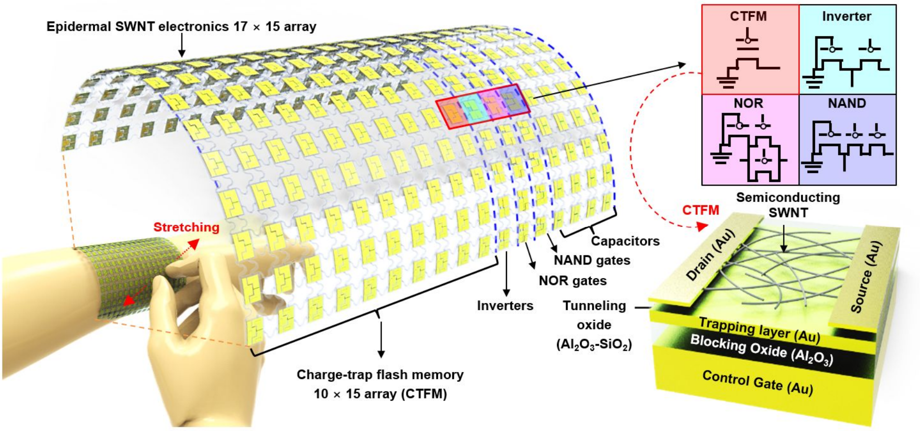

Figure 3.1 Schematic illustration of the s-SWNT-based electronic devices as a wearable array platform, which consists of memory units, capacitors, and logic circuits (left). Simple circuitry schematics (CTFM, inverter, and NAND/NOR gates) are shown in the top right colored sections. The bottom right frame shows the cross-sectional layer information of the CTFM.

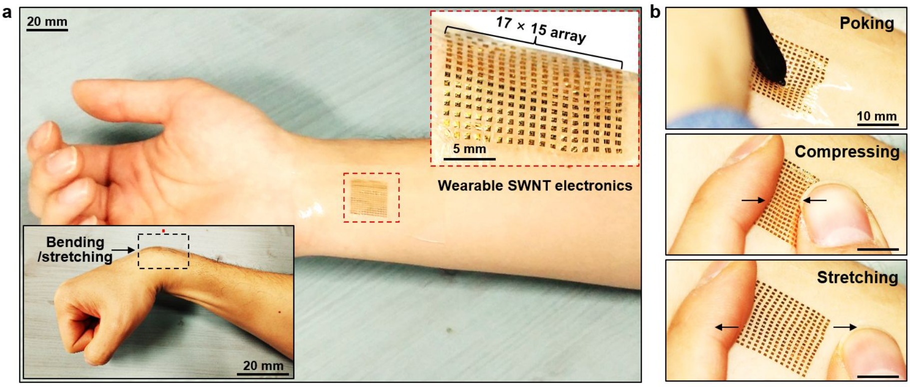

Figure 3.2 **a,** Optical camera image of the array of s-SWNT electronic devices (17 × 15) composed of CTFMs, inverters, NAND/NOR gates, and capacitors. Conformal contacts are well made with a human skin. The insets show a magnified image (top right) and bending/stretching deformations (bottom left). **b,** Deformed wearable s-SWNT devices under poking (top), compression (middle), and stretching (bottom).

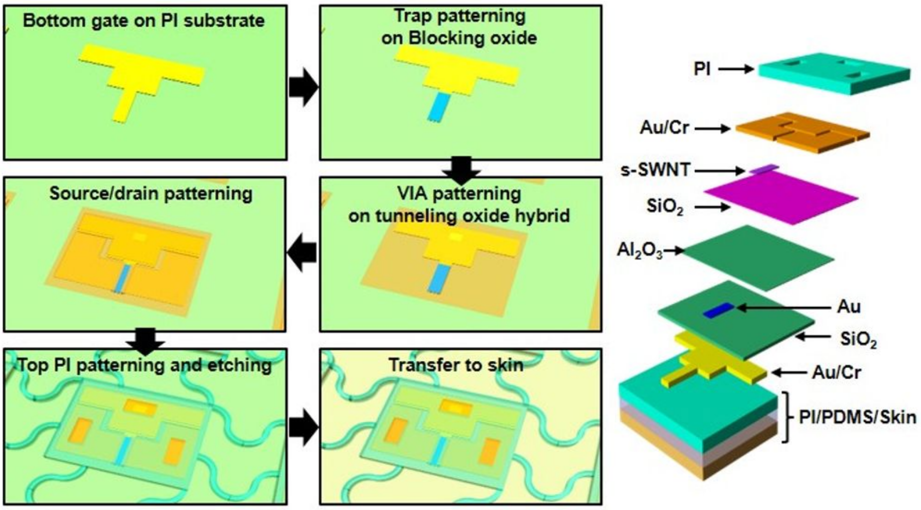

Figure 3.3 (Left) Schematic illustration of the fabrication process and (right) exploded layer view of the wearable s-SWNT-based CTFM (right).

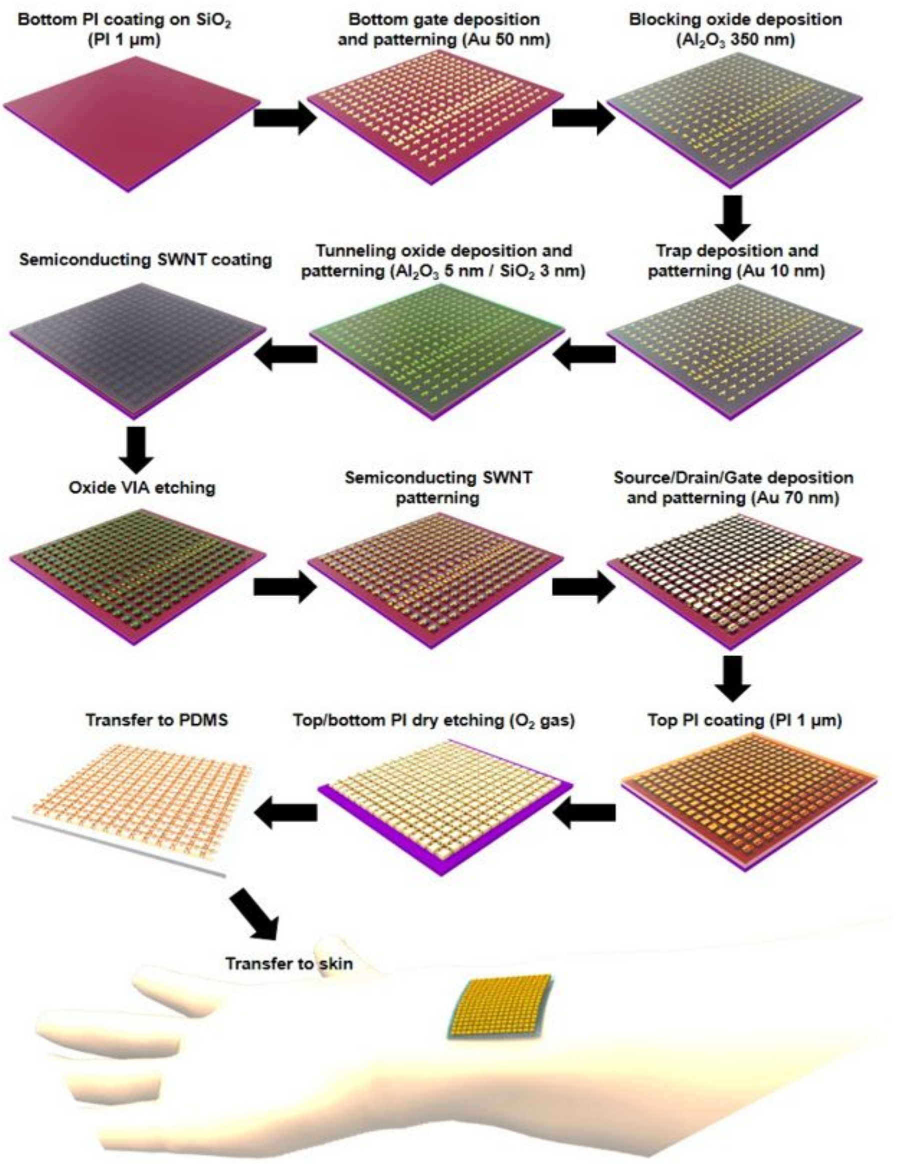

Figure 3.4 Schematic illustration of the overall fabrication process in a large-scale view.

Materials characterization

Figure 3.5a shows an optical microscope image (top view) of the CTFM with the s-SWNT channel and Au thin-film trap layer. The red-dashed box highlights the active area. The atomic force microscopy (AFM) image shows the magnified view of the s-SWNT networks in the channel (Figure 3.5b). It has been reported that random networks of SWNTs are well percolated if the density of the connected SWNTs exceeds a certain threshold[44]. This percolation threshold can be approximately quantified by using the number density (per unit area; ρ), in which the average distance between SWNTs, $1/\rho^{1/2}$, equals to their average lengths, i.e., $\rho_{\mathrm{th}} \sim 1/\langle\text{SWNT length}\rangle^2$. The estimated unit density of the s-SWNT networks is approximately 30 ~ 40 tubes/μm^2: given the density, length, and device dimensions (channel lengths of 20, 30, and 40 μm), it can be concluded that the percolation of SWNTs is successfully formed to constitute an electrically conductive path between the source and drain electrodes[45]. Further improvements in the percolation of SWNT networks can be achieved by scaling down the channel length using industry facilities. To understand the structural compositions of the CTFMs, cross-sectional transmission electron microscopy (TEM) and energy-dispersive X-ray spectroscopy (EDS) images are presented in Figures 3.5c and d, respectively. The magnified TEM image (Figure 3.5c, right) shows the source/drain (Cr/Au) electrodes (~7 nm/70 nm), hybrid tunneling oxides composed of ~3 nm SiO_2 ($T_{ox}1$) and ~5 nm Al_2O_3 ($T_{ox}2$), ~10-nm Au thin-film trap, and ~35 nm B_{ox}, from top to bottom. The TEM images of the CTFM show no visible cracks or voids. The elements in each layer are confirmed by EDS data (Figure 3.5d).

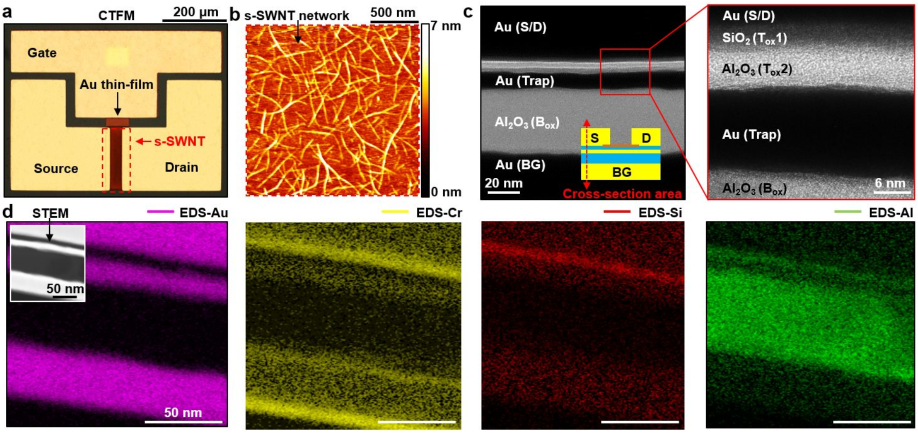

Figure 3.5 a, Optical microscope image of a CTFM (top view). The red-dashed box indicates the active channel region composed of a random network of s-SWNTs. **b,** AFM image of the 99.9%-sorted s-SWNTs layer showing high density of percolated s-SWNT networks. **c,** (Left) Cross-sectional TEM image of the CTFM and (right) its magnified view. **d,** EDS images showing the elements of each layer: Au, Cr, Si, and Al, from left to right, respectively.

Electrical characterization of CTFM

Figure 3.6a shows two schematic illustrations describing the band bending of the CTFMs under applied positive/negative biases on the gate (program/erase (PGM/ERS) operation of CTFM; top/bottom, respectively). Electrons are trapped in the Au thin-film by tunneling (the band gap of SiO_2 ($T_{ox}1$) and Al_2O_3 ($T_{ox}2$) are ~9 eV and ~8.8 eV, respectively) through the ultrathin oxide hybrids (~3 nm/~5 nm for $T_{ox}1/T_{ox}2$) under a positive gate bias (PGM operation)[46-48]. The ERS operation (negative gate bias) discharges electrons from the Au floating gate to the SWNTs by tunneling through the $T_{ox}1/T_{ox}2$ layers. This charge capturing and releasing behavior of the CTFM is closely related to its junction capacitance, characterized in detail using capacitors. Figure 3.6b plots the statistical normalized junction capacitance-voltage (*C*-*V*) characteristics (at 2 kHz) with a voltage sweep from -10 V to 10 V. A large hysteresis can be observed, which is a well-known phenomenon in SWNT-based devices that mainly results from the hydroxyl groups (–OH) at the interface between the gate dielectric and the SWNTs; the SWNTs in the channel region can be electrostatically modulated by carrier charging and discharging of –OH groups. The *C*-*V* curves with Au thin-film trap (red) exhibit larger hysteresis than that without the trap layer (blue), which proves that the Au thin film serves as a charge-trap layer of the non-volatile memory unit. The non-overlapped gate/source structures with different channel lengths/areas (Figure 3.6c) are used to extract the gate capacitance per unit area (C_{ox}; Figure 3.6d), while minimizing the parasitic capacitance. A C_{ox} value of ~7.60 × 10^{-8} F/cm^2 is extracted from the linear slope of the capacitance versus area plot (Figure 3.6e).

The electrical performance of the transistors that compose the CTFMs is characterized under ambient conditions (Figure 3.7). Figure 3.7a illustrates the transfer curves (I_d-V_g; drain current-gate voltage) of the transistors in the CTFMs with different channel lengths (L = 20 μm, 30 μm, and 40 μm) at the applied drain voltage (V_d) of -5 V. A typical transfer curve of a field-effect transistor (FET, without a charge-trap layer) with L = 20 μm is shown in Figure 3.8, for comparative analysis. Owing to the better control of s-SWNTs in the channel area by the gate, the FET exhibits a higher performance in terms of on/off currents. The I_d-V_d and I_d-V_g characteristics of the transistors at L = 30 μm under different V_g are shown in Figures 3.9a,b, respectively. The 150 transistors (10 × 15 array) whose channel lengths (L) range from 20 to 40 μm effectively function without significant variations in the on/off ratio and on-current density. Figure 3.7b shows the cumulated I_d-V_g curves of the 50 transistors in the CTFMs at L = 30 μm, exhibiting high device-to-device uniformity. We can further validate these through statistical analysis of the on-current density per unit width (I_{on}/W; Figure 3.7c), on/off ratio (I_{on}/I_{off}; Figure

3.7d), transconductance per unit width (g_m/W; Figure 3.7e), and carrier mobility at V_d = -5 V (μ; Figure 3.7f). In summary, the averages of I_{on}/W, I_{on}/I_{off}, g_m/W, and μ are 0.36 ± 0.16 μA/μm, > 10^5, 0.057 ± 0.021 μS/μm, and 4.51 ± 1.67 cm^2/Vs, respectively. For the estimation of μ, the equation for the parallel-plate model[20] is used, namely, $\mu = Lg_m/(V_dC_{ox}W)$, where $C_{ox} = 7.60 \times 10^{-8}$ F/cm^2 (from Figure 3.6e).

The typical memory switching characteristics of the CTFMs as a function of the pulse time at different gate voltages ranging from ±15 V to ±25 V are plotted in Figures 3.10a,b. The drain current is the current measured at a read voltage of 0 V. For both PGM/ERS operations, increase/decrease in the drain current can be observed even for a short pulse period of 10^{-6}. This result indicates the effective charging/discharging of the carriers into/from the trap layer. Larger change in the drain current can be observed by increasing the duration of the pulse time for both PGM/ERS operations. The CTFM at L = 30 μm is characterized in two read-out PGM and ERS operations at the gate voltage/pulse time of +25 V/1 s and -25 V/1 s, respectively (Figure 3.10c). The window margin that corresponds to the difference in the drain current at $V_g = 0$ and the device-to-device uniformity of the 50 CTFMs are appropriate for unambiguous read-out (Figure 3.10d). Figure 3.10e shows the endurance characteristics of the CTFMs under the operating condition of ±25 V/100 μs.

The CTFMs maintain substantial window margins even after PGM/ERS operations of 10,000 cycles. The retention test (Figure 3.10f) also verifies the reasonable window margin maintained after approximately 10,000 s.

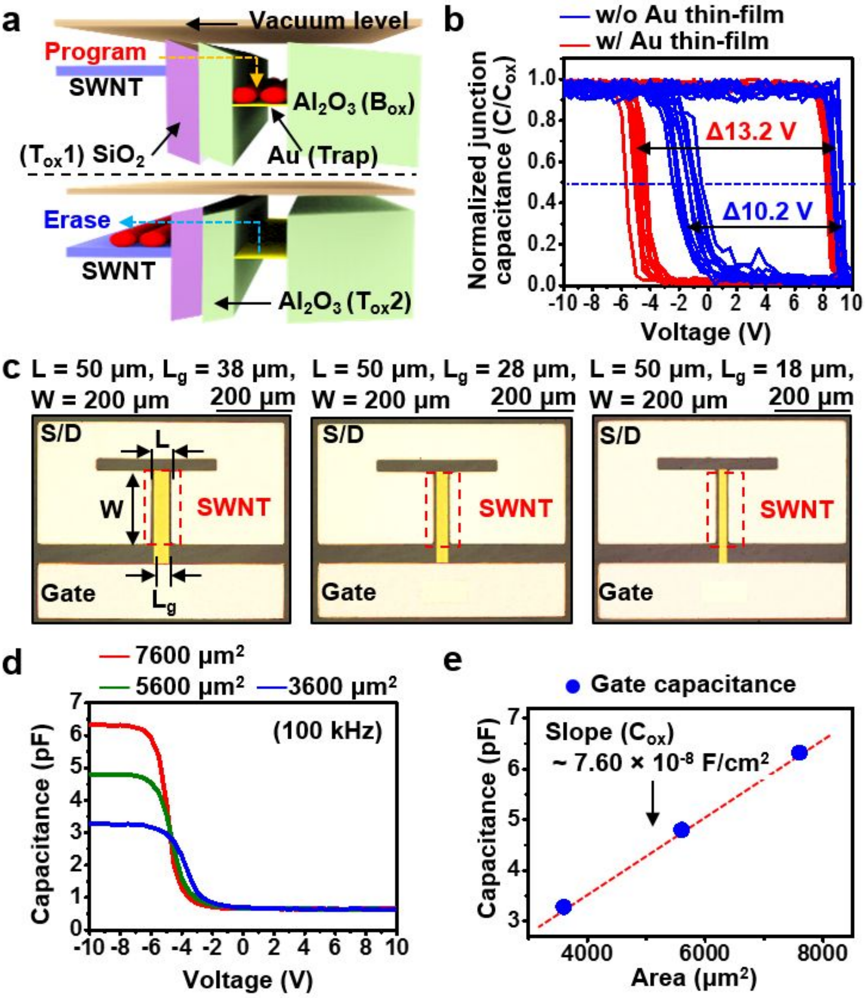

Figure 3.6 a, Band bending of the CTFM in the electron charging/discharging process through the $T_{ox}1$ and $T_{ox}2$ layers in the PGM/ERS operations. **b,** *C-V c*haracteristics showing different voltage hystereses (~13.2 V with trap layer (red) and ~10.2 V without trap layer (blue)) with a voltage sweep from -10 V to 10 V. **c,** Optical microscope images of the non-overlapped gate/source

structures with different gate lengths (L_g) of 38, 28, and 18 μm. **d,** Plot of the gate capacitance per unit area. **e,** Plot of the capacitance versus area with a linear slope (C_{ox}) of ~7.60 × 10^{-8} F/cm^2.

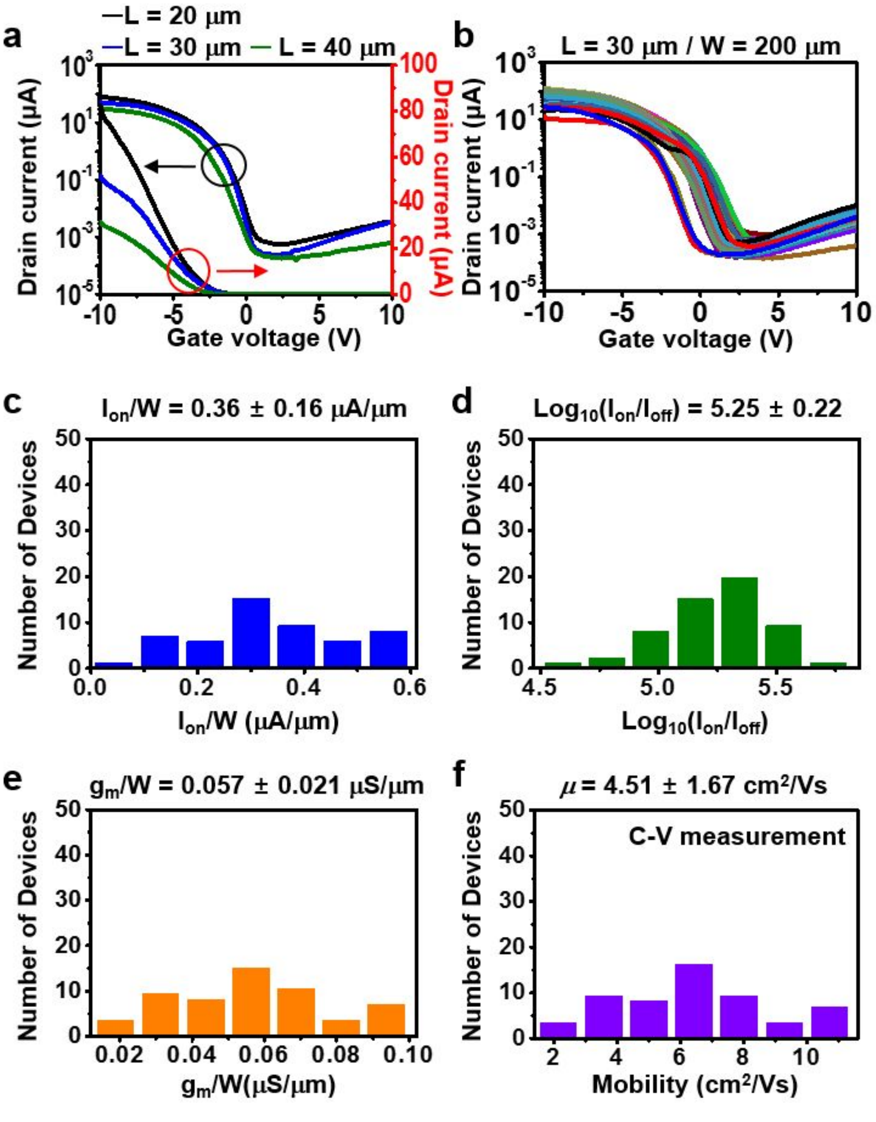

Figure 3.7 a, I_d-V_g curves of the transistors that compose the CTFMs with different channel lengths (L = 20, 30, and 40 μm). **b,** Cumulative I_d-V_g characteristics of 50 transistors with L = 30 μm. **c,** On-current density per unit

width at V_d = -5 V. **d,** On/off ratio at V_d = -5 V. **e,** Transconductance per unit width at V_d = -5 V. **f,** Mobility at V_d = -5 V.

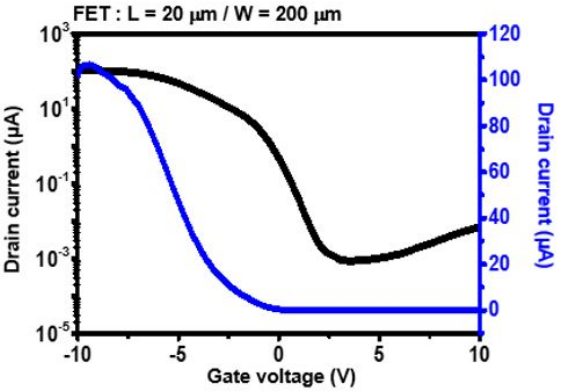

Figure 3.8 Typical I_d-V_g curve of an s-SWNT field-effect transistor with $L = 20$ μm and $W = 200$ μm.

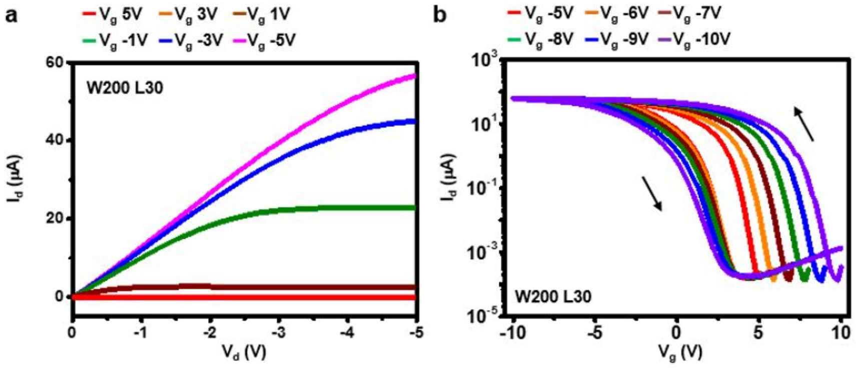

Figure 3.9 a, I_d-V_d characteristics and **b,** I_d-V_g characteristics of CTFM under different V_g (L = 30 μm).

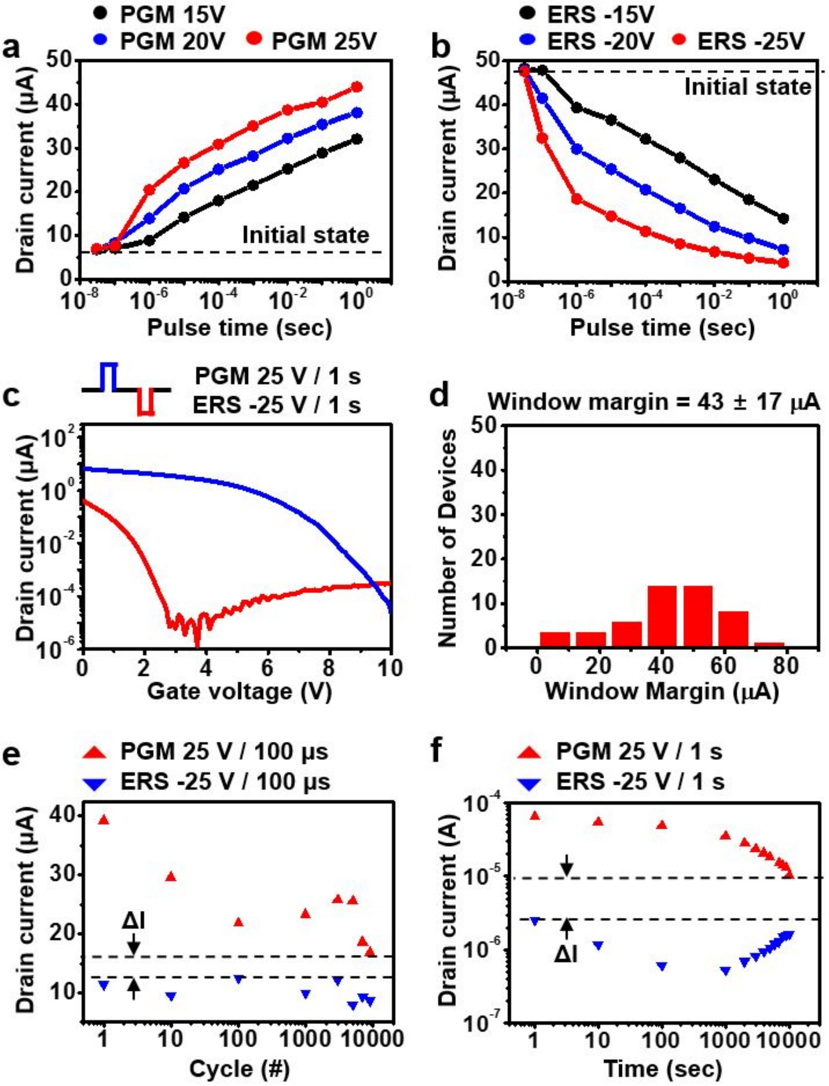

Figure 3.10 a, Memory switching characteristics as a function of the pulse time with applied gate voltages of 15 V, 20 V, and 25 V for the PGM operation. **b,** Memory switching characteristics for the ERS operation with inverse gate

voltages of -15 V, -20 V, and -25 V. **c,** Plot of the two read-out operations. PGM and ERS at +25 V/1 s and -25 V/1 s, respectively. **d,** Statistics of the window margins of the 50 CTFMs after PGM/ERS operations at ±25 V/1 s. **e,** Endurance characteristics of the CTFMs during 10,000 PGM/ERS cycles with ±25 V/100 μs. **f,** Retention characteristics of the CTFMs under PGM/ERS at ±25 V/1 s.

Electrical characterization of logic gates

In addition to the capacitors, transistors, and CTFMs, logic gates are important components in digital circuits. The voltage transfer curves (VTCs) and output characteristics of the logic gates (inverters and NAND/NOR gates) are shown in Figure 3.11. An optical microscope image of an inverter and its VTCs (V_{DD} ranging from -5 V to -10 V) are shown in Figures 3.11a,b, respectively. The VTCs show typical input/output behavior of the logic inverter, *i.e.*, V_{OUT} decreases from 0 to V_{DD} as V_{IN} increases from V_{DD} to 0. The voltage gains at each V_{DD} are shown in Figure 3.11c and their summary is shown in Figure 3.11d (top). An important factor in the characterization of inverter performance is the noise margins *i.e.*, the high- and low-state noise margins (NM_H and NM_L). NM_H and NM_L are estimated as $NM_H = V_{OH} - V_{IH}$ and $NM_L = V_{IL} - V_{OL}$, where V_{OH}, V_{OL}, V_{IH}, and V_{IL} denote the output high voltage, output low voltage, input high voltage, and input low voltage, respectively. The measured noise margins with respect to different V_{DD} are plotted at the bottom of Figure 3.11d. The detailed values are listed in Figure 3.12. The average noise margin for the applied V_{DD} is $0.190 \times V_{DD}$, which shows the reliable and robust operation of the inverters. The inverter is successfully extended for more advanced logic gates (two-input NAND and NOR; Figures 3.11e,g), as shown in their output characteristics (Figures 3.11f,h). V_{DD} of -5 V is used along with input voltages of -5 V and 0 V for logic “1” and “0”, respectively.

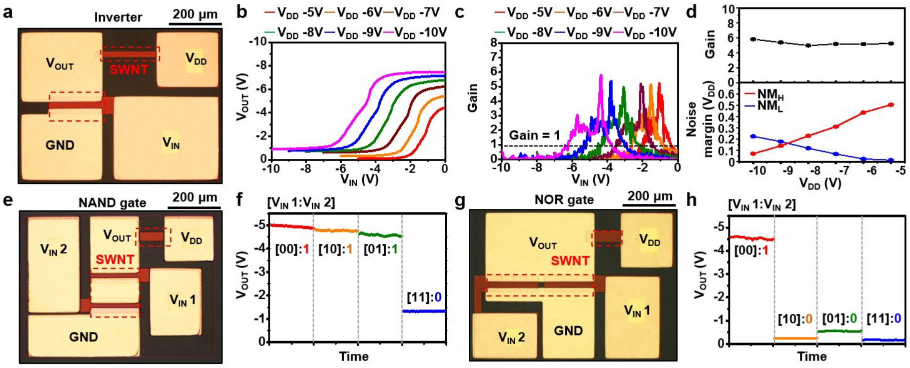

Figure 3.11 **a,** Optical microscope image of an inverter. The red-dashed box indicates the random network of s-SWNTs in the active channel region. **b,** VTCs showing the input and output behavior of the inverter. V_{DD} varies from -5 V to -10 V. **c,** Voltage gain of the inverter. **d,** (Top) Summary of voltage gains and (bottom) noise margins with respect to different V_{DD} ranging from -5 V to -10 V. **e,** Optical microscope image of a two-input NAND logic gate. **f,** Output characteristics of a two-input NAND logic gate with V_{DD} of -5 V and input voltages of -5 V and 0 V. **g,** Optical microscope image of a two-input NOR logic gate. **h,** Output characteristics of a two-input NOR logic gate with V_{DD} of -5 V and input voltages of -5 V and 0 V.

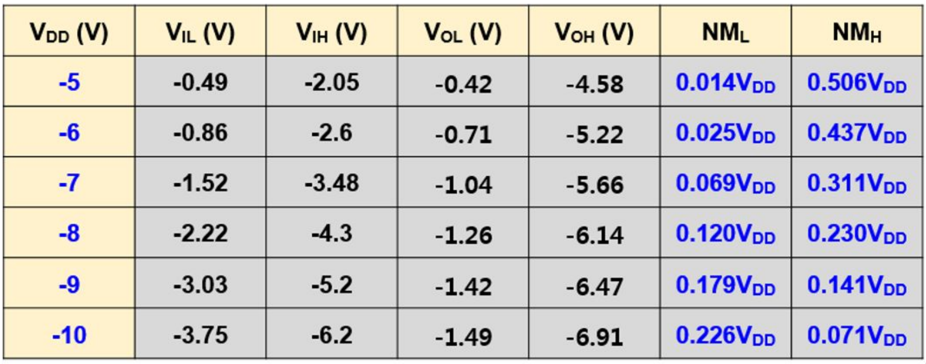

V_{DD} (V)	V_{IL} (V)	V_{IH} (V)	V_{OL} (V)	V_{OH} (V)	NM_L	NM_H
-5	-0.49	-2.05	-0.42	-4.58	0.014V_{DD}	0.506V_{DD}
-6	-0.86	-2.6	-0.71	-5.22	0.025V_{DD}	0.437V_{DD}
-7	-1.52	-3.48	-1.04	-5.66	0.069V_{DD}	0.311V_{DD}
-8	-2.22	-4.3	-1.26	-6.14	0.120V_{DD}	0.230V_{DD}
-9	-3.03	-5.2	-1.42	-6.47	0.179V_{DD}	0.141V_{DD}
-10	-3.75	-6.2	-1.49	-6.91	0.226V_{DD}	0.071V_{DD}

Figure 3.12 High- and low-state noise margins of the inverter at different V_{DD}

Stretching analysis of CTFM and inverter

In wearable electronics, a stable electrical operation of devices under external applied strains is important. The electrical performance results of s-SWNT CTFMs and inverters with different uniaxial strains (up to ~20%; typical maximum strain induced in a human skin[5]) are characterized and compared with theoretical analyses, as shown in Figure 3.13. The island-shape active and serpentine-shape interconnection designs, together with the neutral mechanical plane layout[16], enable the devices to endure an ~20% applied strain while minimizing the deformations/strains in the channels and active regions (Figures 3.13a,c; see strain distributions obtained by Finite Element Analysis (FEA) under each applied strain in Figures 3.13c,d). It can also be inferred that the disconnection issues of SWNT network percolations and/or extraction of SWNTs from the metal source/drain contacts is effectively avoided by unwanted movements of the SWNTs due to the applied strain. The maximum induced strain in the active (~0.001) and interconnection (~0.036) regions is below the typical fracture strain of the device components. The corresponding electrical characterizations of the CTFMs and inverters during the stretching tests are shown in Figures 3.13e,f, respectively. The PGM and ERS curves of the CTFM (PGM and ERS at +25 V/1 s and -25 V/1 s) and VTCs of the inverter under external strains show no visible variations and/or signs of electrical degradations. Even after stretching for 1,000 times with ~20% applied strain, the device performance shows minimal changes (Figure 3.14). In addition, the bending test of the inverter is conducted at different radii of curvature between infinite (flat) and ~5-mm bending radii (Figure 3.15). The induced strains on the inverter (FEA; Figure 3.15b) are negligible. The stable electrical characterization results confirm the effectiveness of the material and design strategies (Figure 3.15c).

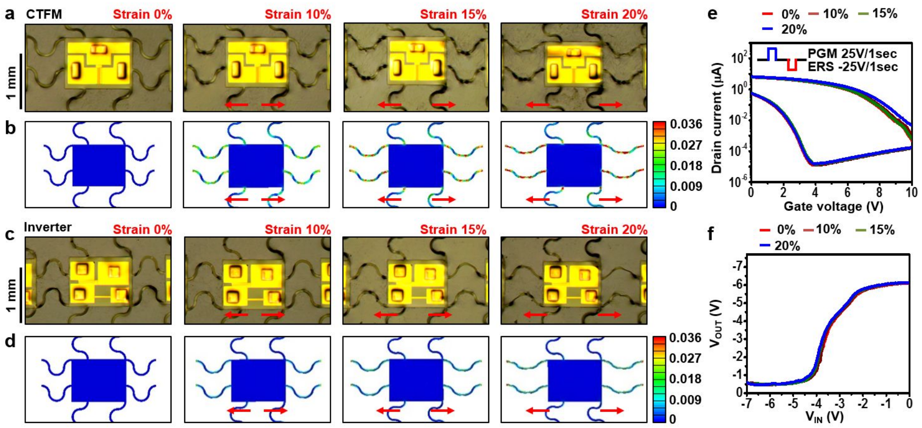

Figure 3.13 **a,** Optical microscope image and **b,** FEA strain distribution results of the CTFM under applied strains between 0% and 20%. The red arrows indicate the strain direction. **c,** Optical microscope image and **d,** FEA strain distribution results of the inverter under applied strains between 0% and 20%. **e,** Electrical characteristics of the CTFM under applied strains between 0% and 20% (PGM and ERS at -25 V/1 s and +25 V/1 s, respectively). **f,** VTCs of the inverter showing stable operation under applied strains between 0% and 20%.

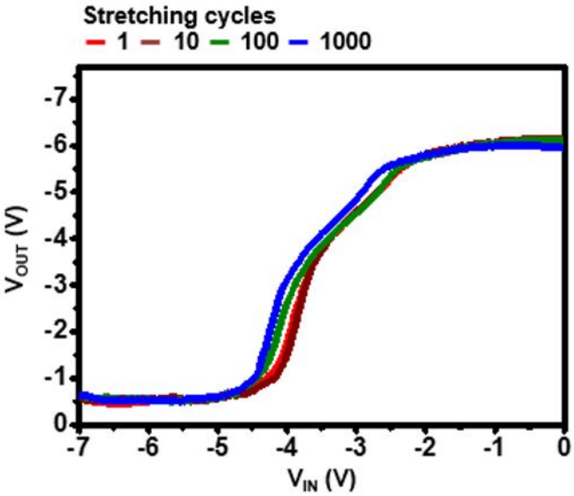

Figure 3.14 VTCs of the inverter after cycled stretching tests. The number of stretching cycles and applied strain are 1, 10, 100, and 1000 times and 20%, respectively.

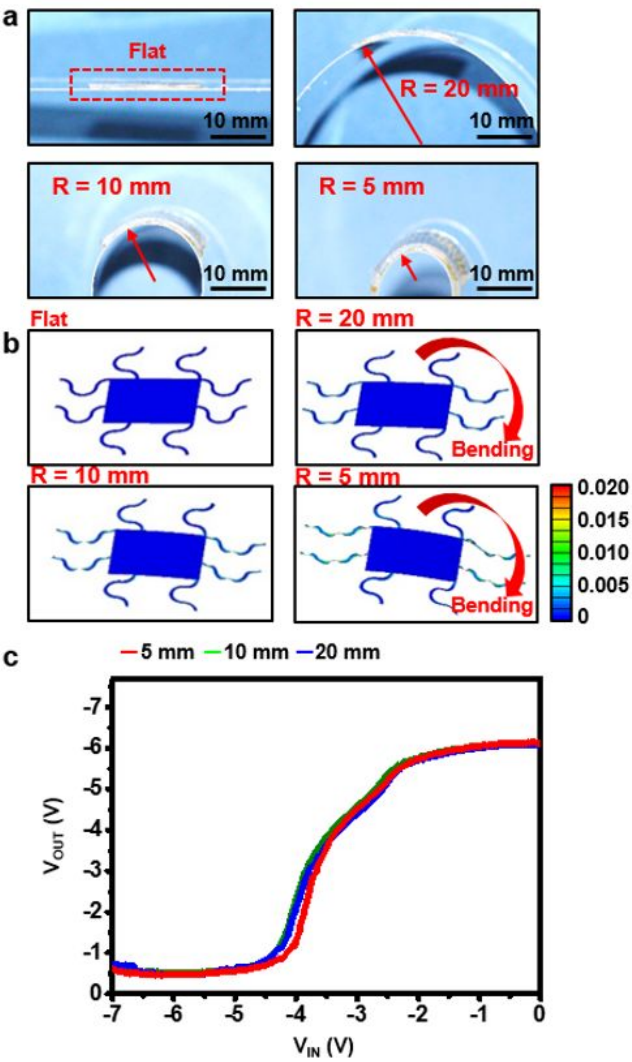

Figure 3.15 a, Optical camera images and **b,** corresponding induced strain distributions by FEA of the inverter in bending tests. The radius of curvature ranges from infinite (flat) to ~5 mm. **c,** VTCs of the inverter that show stable electrical operation at different radii of curvature (5, 10, and 20 mm).

3.4 Conclusion

In summary, we have reported stretchable s-SWNT-based electronic devices, such as capacitors, transistors, nonvolatile memory units, and logic gates. The arrayed stretchable devices are conformally laminated on a curvilinear and soft human skin. Deformations including poking, compression, and stretching do not cause delamination or mechanical fractures. The detailed material analyses using electron and elemental microscopies as well as the theoretical explanations based on numerical mechanic modeling/simulations validate the electrical characterizations, *i.e.*, the reliable device operations. The performance of the memory and logic devices is well maintained even after repetitive stretching/fatigue tests. These soft electronic devices based on s-SWNTs can provide novel opportunities for wearable electronics.

References

1. Wang, C.; Hwang, D.; Yu, Z.; Takei, K.; Park, J.; Chen, T.; Ma, B.; Javey, A. User-interactive electronic skin for instantaneous pressure visualization. *Nat. Mater.* **2013,** 12*,* 899-904.
2. White, M. S.; Kaltenbrunner, M.; Glowacki, E. D.; Gutnichenko, K.; Kettlgruber, G.; Graz, I.; Aazou, S.; Ulbricht, C.; Egbe, D. A. M.; Miron, M. C.; Major, Z.; Scharber, M. C.; Sekitani, T.; Someya, T.; Bauer, S.; Sariciftci, N. S. Ultrathin, highly flexible, and stretchable PLEDs. *Nat. Photonics* **2013**, 7, 811-816.
3. Xu, S.; Zhang, Y.; Jia, L.; Mathewson, K. E.; Jang, K. -I.; Kim, J.; Fu, H.; Huang, X.; Chava, P.; Wang, R.; Bhole, S.; Wang, L.; Na, Y. J.; Guan, Y.; Flavin, M.; Han, Z.; Huang, Y.; Rogers, J. A. Soft microfluidic assemblies of sensors, circuits, and radios for the skin. *Science* **2014**, 344, 70-74.
4. Kaltenbrunner, M.; Sekitani, T.; Reeder, J.; Yokota, T.; Kuribara, K.; Tokuhara, T.; Drack, M.; Schwodiauer, R.; Graz, I.; Bauer-Gogonea, S.; Bauer, S.; Someya, T. An ultra-lightweight design for imperceptible plastic electronics. *Nature* **2013**, 458-463.
5. Son, D.; Lee, J.; Qiao, S.; Ghaffari, R.; Kim, J.; Lee, J. E.; Song, C.; Kim, S. J.; Lee, D. J.; Jun, S. W.; Yang, S.; Park, M.; Shin, J.; Do, K.; Lee, M.; Kang, K.; Hwang, C. S.; Lu, N.; Hyeon, T.; Kim, D. -H. Multifunctional

wearable devices for diagnosis and therapy of movement disorders. *Nat. Nanotechnol.* **2014**, 9, 397-404.

6. Kim, J.; Lee, M.; Shim, H. J.; Ghaffari, R.; Cho, H. R.; Son, D.; Jung, Y. H. Soh, M.; Choi, C.; Jung, S.; Chu, K.; Jeon, D.; Lee, S. -T.; Kim, J. H. ; Choi, S. H.; Hyeon, T.; Kim, D. -H. Stretchable silicon nanoribbon electronics for skin prosthesis. *Nat. Comm.* **2014**, 5, 5747.
7. Zhang, X.; Yu, Z.; Wang, C.; Zarrouk, D.; Seo, J. -W. T.; Cheng, J. C.; Buchan, A. D.; Takei, K., Zhao, Y.; Ager, J. W.; Zhang, J.; Hettick, M.; Hersam, M. C.; Pisano, A. P.; Fearing, R. S.; Javey, A. Photoactuators and motors based on carbon nanotube with selective chirality distrbutions. *Nat. Comm.* **2014**, 5, 2983.
8. Pang, C.; Koo, J. H.; Nguyen, A.; Caves, J. M.; Kim, M.-G.; Chortos, A.; Kim, K.; Wang, P. J.; Tok, J. B.-H.; Bao, Z. Highly skin-conformal microhairy sensor for pulse signal amplification. *Adv. Mater.* **2015**, 27, 634-640.
9. Dagdeviren, C.; Su, Y.; Joe, P.; Yona, R.; Liu, Y.; Kim, Y. -S; Huang, Y.; Damadoran, A. R.; Martin, L. W.; Huang, Y.; Rogers, J. A. Conformable amplified lead zirconate titanate sensors with enhanced piezoelectric response for cutaneous pressure monitoring. *Nat. Comm.* **2014**, 5, 4496.

10. Sekitani, T.; Yokota, T.; Zschieschang, U.; Klauk, H.; Bauer, S.; Takeuchi, K.; Takamiya, M.; Sakurai, T.; Someya, T. Organic nonvolatile memory transistors for flexible sensor arrays. *Science* **2009**, 326, 1516-1519.
11. Park, Y. J.; Lee, S. -K.; Kim, M. -S.; Kim, H.; Ahn, J. -H. Graphene-based conformal devices. *ACS Nano* **2014**, 8, 7655-7662.
12. Jeong, J. -W.; Yeo, W. -H.; Akhtar, A.; Norton, J. J. S.; Kwack, Y. -J.; Li, S.; Jung, S. -Y.; Su, Y.; Lee, W.; Xia, J.; Cheng, H.; Huang, Y.; Choi, W. -S.; Bretl, T.; Rogers, J. A. Materials and optimized designs for human-machine interfaces via epidermal electronics. *Adv. Mater.* **2013**, 25, 6839-6846.
13. Lim, S.; Son, D.; Kim, J.; Lee, Y. B.; Song, J. -K.; Choi, S.; Lee, D. J.; Kim, J. H.; Lee, M.; Hyeon, T.; Kim, D. -H. Transparent and stretchable interactive human machine interface based on patterned graphene heterostructures. *Adv. Funct. Mater.* **2015**, 25, 375-383.
14. Jung, S.; Kim, J. H.; Kim, J.; Choi, S.; Lee, J.; Park, I.; Hyeon, T.; Kim, D. -H. Reverse-micelle-induced porous pressure-sensitive rubber for wearable human-machine interfaces. *Adv. Mater.* **2014**, 26, 4825.
15. Wang, S.; Xie, Y.; Niu, S.; Lin, L.; Wang, Z. L. Freestanding triboelectric-layer-based nanogenerators for harvesting energy from a moving object or human motion in contact and non-contact modes. *Adv. Mater.* **2014**, 26, 2818-2824.

16. Jung, S.; Lee, J.; Hyeon, T.; Lee, M.; Kim, D. -H. Fabric-based integrated energy devices for wearable activity monitors. *Adv. Mater.* **2014**, 26, 6329.

17. Kim, D.; Shin, G.; Kang, Y. J.; Kim, W.; Ha, J. S. Fabrication of a stretchable solid-state micro-supercapacitor array. *ACS Nano* **2014**, 7, 7975-7982

18. Bae, S. -H.; Kahya, O.; Sharma, B. K.; Kwon, J.; Cho, H. J.; Özyilmaz, B.; Ahn, J. -H. Graphene-P(VDF-TrFE) multilayer film for flexible applications. *ACS Nano* **2013**, 7, 3130-3138.

19. Lim, Y.; Yoon, J.; Yun, J.; Kim, D.; Hong, S. Y.; Lee, S. -J.; Zi, G.; Ha, J. S. Biaxially stretchable, integrated array of high performance microsupercapacitors. *ACS Nano* **2014**, 8, 11639-11650

20. Webb, R. C.; Bonifas, A. P.; Behnaz, A.; Zhang, Y.; Yu, K.J.; Cheng, H.; Shi, M.; Bian, Z.; Liu, Z.; Kim, Y. S.; Yeo, W.-H.; Park, J. S.; Song, J.; Li, Y.; Huang, Y.; Gorbach A. M.; Rogers, J. A. Ultrathin conformal devices for precise and continuous thermal characterization of human skin. *Nat. Mater.* **2013**, 12, 938-944.

21. Kim, D. -H.; Song, J.; Choi, W. M.; Kim, H. -S.; Kim, R. -H.; Liu, Z.; Huang, Y. Y.; Hwang, K. -C.; Zhang, Y. -w.; Rogers, J. A. Materials and noncoplanar mesh designs for integrated circuits with linear elastic

response to extreme mechanical deformations. *Proc. Natl. Acad. Sci. U.S.A.* **2008**, 105, 18675-18680.

22. Sekitani, T.; Zscieschang, U.; Klauk, H.; Someya, T. Flexible organic transistors and circuits with extreme bending stability. *Nat. Mater.* **2010**, 9, 1015-1022.
23. Kim, D. -H.; Lu, N.; Ma, R.; Kim, Y. -S.; Kim, R. -H.; Wang, S.; Wu, J.; Won, S. M.; Tao, H.; Islam, A.; Yu, K. J.; Kim, T. -I.; Chowdhury, R.; Ying, M.; Xu, L.; Li, M.; Chung, H. -J.; Keum, H.; McCormick, M.; Liu, P.; Zhang, Y. -W.; Omenetto, F. G.; Huang, Y.; Coleman, T.; Rogers, J. A. Epidermal electronics. *Science* **2011**, 333, 838-843.
24. Shin, G.; Bae, M. Y.; Lee, H. J.; Yoon, C. H.; Zi, G.; Rogers, J. A.; Ha, J. S. SnO_2 nanowire logic devices on deformable nonplanar substrates *ACS Nano* **2011**, 5, 10009-10016
25. Fan, J. A.; Yeo, W. -H.; Su, Y.; Hattori, Y.; Lee, W.; Jung, S. -Y.; Zhang, Y.; Liu, Z.; Cheng, H.; Falgout, L.; Bajema, M.; Coleman, T.; Gregoire, D.; Larsen, R. J.; Huang, Y.; Rogers, J. A. Fractal design concepts for stretchable electronics. *Nat. Comm.* **2014**, 5, 3266.
26. Kim, K. S.; Zaho, Y.; Jang, H.; Lee, S. Y.; Kim, J. M.; Kim, K. S.; Ahn, J. -H.; Kim, P.; Choi, J. -Y.; Hong, B. H. Large-scale pattern growth of

graphene films for stretchable transparent electrodes. *Nature* **2009**, 457, 706.

27. Lee, W. H.; Park, J.; Kim, Y.; Kim, K. S.; Hong, B. H.; Cho, K. Control of graphene field-effect transistors by interfacial hydrophobic self-assembled monolayers. *Adv. Mater.* **2011**, 23, 3460-3464.
28. Park, J.; Jo, S. B.; Yu, Y. -J.; Kim, Y.; Yang, J. W.; Lee, W. H.; Kim, H. H.; Hong, B. H.; Kim, P.; Cho, K.; Kim, K. S. Single-gate bandgap opening of bilayer graphene by dual molecular doping. *Adv. Mater.* **2012**, 24, 407-411.
29. Arnold, M. S.; Green, A. A.; Hulvat, J. F.; Stupp, S. I.; Hersam, M. C. Sorting carbon nanotubes by electronic structure using density differentiation. *Nat. Nanotechnol.* **2006**, 60-65.
30. Jin, S. H.; Dunham, S. N.; Song, J.; Xie, X.; Kim, J. H.; Lu, C.; Islam, A.; Du, F.; Kim, J.; Felts, J.; Li, Y.; Xiong, F.; Wahab, M. A.; Menon, M.; Cho, E.; Grosse, K. L.; Lee, D. J.; Chung, H. U.; Pop, E.; Alam, M. A.; King, W. P.; Huang, Y.; Rogers, J. A. Using nanoscale thermocapilary flows to create arrays of purely semiconducting single-walled carbon nanotubes. *Nat. Nanotechnol.* **2013**, 8, 347-355.
31. Park, S.; Lee, H. W.; Wang, H.; Selvarasah, S.; Dokmeci, M. R.; Park, Y. J.; Cha, S. N.; Kim, J. M.; Bao, Z. Highly effective separation of

semiconducting carbon nanotubes verified *via* short-channel devices fabricated using Dip-Pen nanolithography. *ACS Nano* **2012**, 6, 2487-2496.

32. Chae, S. H.; Yu, W. J.; Bae, J. J.; Duong, D. L.; Perello, D.; Jeong, H. Y.; Ta, Q. H.; Ly, T. H.; Vu, Q. A.; Yun, M.; Duan, X.; Lee, Y. H. Transferred wrinkled Al_2O_3 for highly stretchable and transparent graphene-carbon nanotube transistors. *Nat. Mater.* **2013**, 12, 403-409.
33. Ding, L.; Zhang, Z.; Liang, S.; Pei, T.; Wang, S.; Li, Y.; Zhou, W.; Liu, J.; Peng, L.-M. CMOS-based carbon nanotube pass-transistor logic integrated circuits. *Nat. Comm.* **2012**, 3, 677.
34. Pei, T.; Zhang, P.; Zhang, Z.; Qiu, C.; Liang, S.; Yang, Y.; Wang, S.; Peng, L.-M. Modularized construction of general integrated circuits on individual carbon nanotubes. *Nano Lett.* **2014**, 14, 3102-3109.
35. Ding, L.; Zhang, Z.; Pei, T.; Liang, S.; Wang, S.; Zhou, W.; Liu, J.; Peng, L.-M. Carbon nanotube field-effect transistors for use as pass transistors in integrated logic gates and full subtractor circuits. *ACS Nano*, **2012**, 6, 4013-4019.
36. Shulaker, M. M.; Hills, G.; Patil, N.; Wei, H.; Chen, H.-Y.; Wong, H.-S. P.; Mitra, S. Carbon Nanotube Computer. *Nature* **2013**, 501, 526-530.
37. Shulaker, M. M.; Rethy, J. V.; Wu, T. F.; Liyanage, L. S.; Wei, H.; Li, Z.; Pop, E.; Gielen, G.; Wong, H.-S. P.; Mitra, S. Carbon nanotube circuit

integration up to sub-20 nm channel lengths. *ACS Nano* **2014**, 8, 3434-3443.

38. Takahashi, T.; Takei, K.; Gillies, A. G.; Fearing, R. S.; Javey, A. Carbon nanotube active-matrix backplanes for conformal electronics and sensors. *Nano Lett*. **2011**, 5408-5413.
39. Wang, H.; Koleilat, G. I.; Liu, P.; Jimènez-Osès, G.; Lai, Y. -C.; Vosgueritchian, M.; Fang, Y.; Park, S.; Houk, K. N.; Bao, Z. High-yield soring of small-diameter carbon nanotubes for solar cells and transistors. *ACS Nano* **2014**, 8, 2609-2617.
40. Sun, D.; Timmermans, M. Y.; Tian, Y.; Nasibulin, A. G.; Kauppinen, E. I.; Kishimoto, S.; Mizutani, T.; Ohno, Y. Flexible high-performance carbon nanotube integrated circuits. *Nat. Nanotechnol.* **2011**, 6, 156-161.
41. Wang, H.; Mei, J.; Liu, P.; Schmidt, K.; Jiménez-Osés, G.; Osuna, S.; Fang, L.; Tassone, C. J.; Zoombelt, A. P.; Sokolov, A. N.; Houk, K. N.; Toney, M. F.; Bao, Z. Scalable and selective dispersion of semiconducting arc-discharged carbon nanotubes by dithiafulvalene/thiophene copolymers for thin film transistors. *ACS Nano* **2013**, 7, 2659-2668.
42. Wang, C.; Chien, J. -C.; Takei, K.; Takahashi, T.; Nah, J.; Niknejad, A. M.; Javey, A. Extremely nendable, high-performance integrated circuits using

semiconducting carbon nanotube networks for digital, analog, and radio-frequency applications. *Nano Lett.* **2012**, 12, 1527-1533.

43. Yeom, C.; Chen, K.; Kiriya, D.; Yu, Z.; Cho, G.; Javey, A. Large-area compliant tactile sensors using printed carbon nanotube active-matrix backplanes. *Adv. Mat.* **2015**, 27, 1561-1566.
44. Snow, E. S.; Novak, J. P.; Campbell, P. M.; Park, D. Random networks of carbon nanotubes as an electronic material. *Appl. Phys. Lett.* **2003**, 82, 2145-2147.
45. Jang, H.-K.; Jin, J. E.; Choi, J. H.; Kang, P.-S.; Kim, D.-H.; Kim, G. T. Electrical percolation thresholds of semiconducting single-walled carbon nanotube networks in field-effect transistors. *Phys. Chem. Chem. Phys.* **2015**, 17, 6784-6880.
46. Olmedo, M.; Wang, C.; Ryu, K.; Zhou, H.; Ren, J.; Zhan, N.; Zhou, C.; Liu, J. Carbon nanotube memory by the self-assembly of silicon nanocrystals as charge storage nodes. *ACS Nano* **2011**, 7972-7977.
47. Yu, W. J.; Kang, B. R.; Lee, I. H.; Min, Y. -S.; Lee, Y. H. Majority carrier type conversion with floating gates in carbon nanotube transistors. *Adv. Mat.* **2009**, 21, 4821-4824.

48. Chan, M. Y.; Wei, L.; Chen, Y.; Chan, L.; Lee, P. S. Charge-induced conductance modulation of carbon nanotube field effect transistor memory Devices. *Carbon* **2009**, 47, 3063-3070

Chapter 4. Bioresorbable Electronic Stent Integrated with Therapeutic Nanoparticles for Endovascular Diseases

4.1 Introduction

Balloon angioplasty and stent placement procedures have helped shape patient care across a broad range of cardio-,[1] neuro-[2] and peripheral[3] vascular diseases. Approximately six million patients[4] receive percutaneous coronary interventions (PEI) to treat arterial obstructions and endothelial injuries annually. While PEI using bare metal stents has been demonstrated to restore blood flow, there are key limitations in which neointimal hyperplasia and smooth muscle cells (SMC) may accumulate near the stent.[5] These limitations are thought to arise because of a complex interplay of turbulent blood flow and inflammatory reactions around the stent.[1,5] To overcome drawbacks of bare metal stents, several approaches have been reported, including bioresorbable stents[6] and drug-eluting stents,[7] which provide physical disappearance and deliver pharmacological agents, respectively, to mitigate risks of in-stent restenosis (ISR).

Although these existing classes of endovascular implants have enormous utility with minimal health risks, they do not provide diagnostic feedbacks on the state of hemodynamics and active controls of localized delivery of advanced therapeutic agents due to the absence of onboard sensors, data storage, and therapeutic actuation. Bioresorbable electronic stents that combine sensing of blood flow and temperature *via* integrated electronics coupled with data storage modules[8] represent a fundamentally new set of functionality onboard otherwise inert bioresorbable implants. High performance flexible[9-11] and bioresorbable[12,13] electronics provide unique solutions for the integration of active electronics onto the inflatable and bioresorbable stent. Besides, advanced therapeutics *via* functionalized nanoparticles[14-16] hold promise to further advance PEI through controlled drug release and long-term inflammation suppression. Inorganic nanoparticles have been explored as therapeutic platforms because of their high surface-to-volume ratio,[17] scavenging reactive oxygen species (ROS),[18] and photoactivation properties.[19]

Here, we describe bioresorbable/bioinert nanomaterials designs and their integration strategies with bioresorbable electronic stent (BES), fitted with nanomebrane-based flexible flow/temperature sensors and memory storage devices, anti-inflammatory nanoparticles, and drug-loaded core/shell nanospheres that are activated by an external optical stimulus. Additionally, antenna characteristic of BES for wireless power/data communication is evaluated. The mode of operation is as follows: the flow sensor measures blood flow, which is stored into the embedded memory module for pattern analysis and diagnosis. Catalytic ROS scavenging and hyperthermia-based drug release can be used as advanced therapies. First, the ceria nanoparticles (ceria NPs)[20] scavenge ROS generated in the perfusion by PEI and reduce inflammations that can cause in-stent thrombosis.[21] Secondly, the gold nanorod core/mesoporous silica nanoparticle shell (AuNR@MSN)[22,23] design is able to control the drug loading and its release photothermally. The hyperthermia is regulated through the temperature feedback. The hyperthermia, which is regulated *via* feedback temperature sensing, controls localized drug delivery as well as provides thermal therapy. This suite of sensors and actuators provides mechanical, photothermal, diagnostic and therapeutic functionality on bioresorbable stent substrates.

***The contents of this chapter were published in ACS Nano.**

(2015, DOI: 10.1021/acsnano.5b00651, Article ASAP)

1.2 Experimental Section

Fabrication of Mg/MgO/Mg memory on the Mg alloy stent: For the fabrication of Mg alloy stents, we first laser-cut and polish ZM21 Mg alloy ingot. AZ4620 photoresist (Clariant, USA) is then spin-coated with 3000 rpm (for 30 s) on both sides of the ZM21 Mg alloy substrate (~200 μm). The Mg alloy substrate is then patterned using photolithography and wet etching processes with custom-made Mg etchant (70% Ethylene glycol, 20% de-ionized water, 10% nitric acid). After the etching step, the Mg alloy mesh is dipped into boiling acetone to remove the AZ4620 photoresist. Then, an insulating MgO layer (~50 nm) is deposited on the stent by the electron beam evaporation. Thermal evaporation of Mg (~60 nm) is then applied to create the bottom electrode (base pressure of 1×10^{-6} Torr, ~0.5 Å/sec). The switching layer (MgO, 12 nm) is deposited *via* the sputtering process (base pressure of 5×10^{-6} Torr, Ar 20 sccm, 5 mTorr, 150 W RF power). Next, the top electrode (Mg, ~60 nm) is deposited onto the MgO film through another thermal evaporation step. Another encapsulating layer of MgO (~80 nm) layer is added to the top surface of the Mg/MgO/Mg (RRAM) construct using electron beam evaporation. Finally, the entire RRAM device on the stent is coated with PLA (M_w ~ 160,000, M_w/M_n ~

1.5, Sigma Aldrich, USA) solution, containing ceria NPs and AuNR@MSN (3 wt% in chloroform) *via* a dip-coating technique.

Fabrication of temperature/flow sensor on the Mg alloy stent: Mg temperature and flow sensors are composed of an adhesion layer, a long filamentary Mg resistor (sensing unit), and an outer encapsulation layer (MgO and PLA). First, the adhesion layer (~60 nm thick ZnO) is sputtered (base pressure of 5×10-6 Torr, Ar 20 sccm, 5 mTorr, 150 W RF power) on a ~15 µm thick PLA film. The metal line (Mg, ~100 nm) is thermally evaporated through a shadow mask. For encapsulation, ~400 nm thick MgO is deposited using an electron beam evaporation. Additional 2 layers of PLA (~15 µm) are then laminated on top and exposed to chloroform vapour to make the PLA surface sticky. Finally, the sensor film is transfer-printed onto the sticky surface of the polymer on the stent.

***In vitro* ROS scavenging experiment:** Mouse cardiac muscle cells (HL-1) are incubated in Claycomb medium (Sigma Aldrich, USA) supplemented with 10% Fetal bovine serum (Wisent, Canada), 1% Penicillin/Streptomycin (Gibco, USA), 0.1 mM Norepinephrine (Sigma Aldrich, USA), and 2 mM L-Glutamine (Gibco, USA). Separately, HUVECs are incubated in EGMTM-2 BulletKitTM

(Lonza, Switzerland) at 37°C with 5% CO_2 and 95% air. For *in vitro* ROS scavenging experiments, HL-1 cells and HUVECs are placed in 24-well plates and cultured again for 3 days. After removing the cell media, PLA film embedded with ceria NPs (1 cm × 1 cm, ~0.16 g) is placed in the well plate. Reactive oxygen species (50 µM H_2O_2, Sigma Aldrich, USA) are then added to well plates and stored for 5, 10, 15, and 30 min to see oxidative stress effects. Cells are washed with the Dulbecco's Phosphate Buffered Saline (DPBS) and the cell viability is assessed with a Live/Dead® Cell viability/cytotoxicity kit (Invitrogen, USA). Fluorescence images are captured with a fluorescence microscope (Nikon, Eclipse Ti, Japan) and the Image-Pro plus software (MediaCybernetics, USA) kit provides quantitative estimates of living and necrotic cells.

***In vitro* Hyperthermia experiment:** To monitor the cell injury caused by hyperthermia, we first applied photothermal hyperthermic treatments to HUVECs cultured for 3 days in 24-well plates, in which AuNR@MSN-PLA film (5 mm × 5 mm) is placed (Figure 4.16h-k). Cell viability/cytotoxicity kit solution is added to the media to visualize live and dead cells. For the photothermal hyperthermia treatment, 800 nm-pulsed laser light (Mai Tai eHP deepsee, Spectra-Physics, USA) is delivered for 10 min at different powers with the irradiation area of 760 μm × 760 μm. The average irradiance rates are in the range of 1.7 ~ 4.0 W/cm^2 and total energy of 1020 ~ 2400 J/cm^2. After the NIR irradiation, cells are imaged using the confocal microscope (LSM-780, Carl Zeiss, Germany).

Bioresorbable and biocompatible materials in the bioresorbable electronic stent (BES): All materials used in the bioresorbable electronic stent (BES) are either bioinert or biodegradable by the hydrolysis reactions, which result in biocompatible products (Figure 4.3a). Magnesium (Mg) is the bioresorbable metal and is decomposed into magnesium hydroxide ($Mg(OH)_2$). Mg is applied in various system components, such as the temperature/flow sensors and switching electrodes of the resistance random access memory (RRAM). Also Mg is the main component of the magnesium alloy based stent framework (ZM21; Mg 97%, Zn 2%, Mn 1%). Magnesium oxide (MgO; switching layer of RRAM), zinc oxide (ZnO; adhesion layer for the temperature/flow sensor), and mesoporous silica (SiO_2; therapeutic nanoparticles for the drug delivery) are hydrolyzed into their respective bioresorbable metal hydroxides ($Mg(OH)_2$, $Zn(OH)_2$, $Si(OH)_4$). Poly-(lactic acid) (PLA) slowly hydrolyzes into the lactic acid without the enzymatic activity.[1] Due to its slow degradation rate, it can be used as a bioresorbable encapsulation layer (Figure 4.4a) to protect active electronic components that rapidly dissolve in the biofluid such as phosphate buffered solution (PBS) (Figure 4.4b). Small amount of therapeutic nanoparticles, such as ceria (CeO_2) nanoparticles (NPs) and gold nanorods (AuNR), and others (such as Mn in ZM21) are bioinert (Figure 4.3b).

***In vivo* pharmacokinetics, biodistribution, and biocompatibility studies of functional nanoparticles with the mouse model:** For the pharmacokinetic study, 8 weeks BALB/c mice are divided into 3 groups (n = 3) for AuNR, AuNR@MSN, and ceria NPs. The mice are injected with NPs (5 mg Au/kg and 2.5 mg Ce/kg) *via* the tail vein. Blood is collected at different time periods of 1 min, 30 min, 1 h, 3 h, 6 h, 1 day, and 2 days. For the biodistribution analysis, mice are prepared and injected with same manner. After 2 days, organs are dissected and treated with aqua regia to homogenize the organs and dissolve nanoparticles. Supernatants are collected and the concentration is measured by an inductively coupled plasma mass spectrometer (ICP-MS, 820-MS, Varian, Australia).

AuNR, AuNR@MSN, and ceria NPs are injected into the mice to estimate their biocompatibility. Ten days after the injection of nanoparticles, the heart and kidney, liver, lung, pancreas, spleen, and lymph node (at axillary, brachial, and inguinal areas) are extracted and fixed in 10% neutral buffered formalin (10% NBF) for one week. For hematoxylin and eosin (H&E) staining, formalin fixed tissues are embedded into paraffin, and then sectioned with 4 μm thickness. The sectioned tissues are then dewaxed and hydrated, and standard H&E staining is performed to evaluate morphological features of each organ. Stained images are acquired with optical microscope (DM2500, Leica, Germany).

Switching mechanism of the Mg/MgO/Mg memory: The pristine state Mg/MgO/Mg RRAM cell exhibits insulating behavior which reveals the high insulating quality of MgO layer. Set current values that are independent of the memory cell area (Figure 4.7c) suggest that the RRAM operation is based on the repeated formation and rupture of local conducting filaments (CFs) in MgO layer (Figure 4.8). Oxygen vacancies (V_o) can be produced in the electroforming step and the generated V_o form CFs. According to the previous reports regarding the shape and the inhomogeneity of CFs in oxide thin films,[2,3] the shape of the CFs after the electroforming step is assumed to be conical where the diameter of CF near bottom electrode is larger than that near top electrode as shown in Figure 4.8c. With this model of CFs, the actual switching occurs at the weakest part of CFs along its length direction, where the repeated reduction (set) and the oxidation (reset) occur. Such an asymmetric shape of

CFs explains the bipolar resistive switching (BRS) behavior. Two interfaces between the MgO and Mg electrodes (top and bottom) are dissimilar, which also enhances the possibility of the BRS behavior. When the switching layer (MgO) is sputtered on the bottom Mg electrode, the deficient oxygen exists and thereby the MgO layer becomes relatively defect-rich.[4]

FEM of strain distribution of the BES: We used commercial FEM software ABAQUS v6.12 to simulate the mechanical deformation of the stent under the pure bending and to obtain the strain distribution in the active layer (MgO) of memory cells. According to the thickness, the stent and flow sensors are modeled by solid elements whereas all the other much thinner layers are modeled by shell elements. The perfect adhesion is assumed between layers and a fine mesh is adopted. The multilayer stent structure is modeled to be initially flat and then gets bent into two radii, 1 mm and 2 mm, to mimic the deflated and inflated state of the balloon catheter, respectively. FEM results are offered in Figure 4.7g and it is obvious that maximum strains in the MgO layer always occurs at the edges that are close to the serpentine intersections. The maximum strain decreases from 4.6% to 2.2 % with the stent switching from a deflated state with a bending radius of 1 mm to an inflated state with a bending radius of

2 mm, which are both below the fracture strain of MgO (~8%).[5]

Computational fluid dynamics (CFD) simulation of bioresorbable electronic stent: The CFD simulation is performed through COMSOL4.2 to study the flow pattern and wall shear stress (WSS) which is considered to be relevant with the restenosis process.[6] For simplicity, the deformation of the stented artery is neglected and modeled as a cylindrical artery with stent embedded against the inner wall (see the 3D CAE model in Figure 4.11a). The average flow velocity (105 mm/s)[7] is imposed as the constant inlet flow rate and the blood flow is modeled as incompressible flow of a Newtonian fluid with a density of 1,060 kg/m^3 and viscosity of 3.7 cP[8] since the corresponding Mach number and Reynolds number are

$$Ma = \frac{|\boldsymbol{u}|}{a} = 6.69 \times 10^{-5} \ll 1$$

$$Re = \frac{\rho|\boldsymbol{u}|d}{\mu} = 165$$

where $|\boldsymbol{u}| =$ 105 mm/s is the average speed of blood flow, $a =$ 1570 m/s[9] is the speed of sound in blood, ρ is the blood density, $d =$ 5.5 mm is the artery diameter and μ is the blood viscosity. The additional length: $AL = 0.06 \cdot Re \cdot d \approx 10d$ is added to ensure fully developed flow.

The wall shear stress is defined as

$$WSS = 2\mu\gamma$$

where γ is the shear rate and is expressed as

$$\gamma = \sqrt{2\left[\left(\frac{\partial u}{\partial x}\right)^2 + \left(\frac{\partial v}{\partial y}\right)^2 + \left(\frac{\partial w}{\partial z}\right)^2\right] + \left(\frac{\partial u}{\partial y} + \frac{\partial v}{\partial x}\right)^2 + \left(\frac{\partial v}{\partial z} + \frac{\partial w}{\partial y}\right)^2 + \left(\frac{\partial u}{\partial z} + \frac{\partial w}{\partial x}\right)^2}$$

where u, v and w are velocity components in x, y and z directions, respectively. The distributions of WSS throughout the artery is shown in Fig. S8b. As we assume no blood can flow between the stent-artery interface, there is no WSS on such interface. Low WSS was observed in the localized stented area and the immediate downstream of the stent while high WSS was generated in the immediate upstream of the stent.

In vivo, ex vivo **experiment of wireless power/data transmission using BES strut as an antenna unit:** The current BES strut is suitable for a 900 MHz ISM (Industrial, scientific medical) band. The wavelength of 900 MHz decreases from 33.3 cm in the air to 4.1 cm in the human body environment because of the high permittivity and conductivity of body tissues. The current BES, which has an electrical size of 0.317 λ, can be utilized as an effective radiation structure inside the human body at 900 MHz. Figure 4.12a shows *ex vivo* experiment setup for the power/data transmission. The center of the coaxial cable was connected to the end of the stent (Fig. 4.12b). This feeding method enabled the stent antenna to operate as a monopole antenna. The biofluid can be used for the ground.

The simulation was conducted using CST Microwave Studio. The stent antenna is enclosed by homogeneous materials which have electric properties of blood (ε_r = 61.36, σ = 1.538 S/m) (Figure 4.12c). Figure 4.12d shows that the expected radiation pattern of the stent antenna is similar to a conventional monopole antenna. The omni-directional radiation patterns of the monopole antenna are suitable for the stent. The simulated antenna gain was -34.44 dB inside the blood environment.

The measurement setup for the wireless power transfer is shown in Figure 4.12e. The dipole antenna was used as a transmitting antenna. The port 1 and 2 of the network analyzer (E5071C, Agilent, USA) were connected to the stent and transmitting antenna, respectively. S-parameters of the 2-port network was measured using the network analyzer. Figure 4.12f shows measured reflection coefficients of two antennas at the port impedance of 50 Ω. The transmission coefficient (S_{21}) between the stent and transmitting antenna with the distance of 4 cm is plotted in Figure 4.12g. The measured S_{21} was -20.16 dB at 900 MHz, which means that about 10 mW power can be transmitted to the stent antenna when the incident power of the transmitting antenna is 1 W.

Data transmission through the proposed stent structure was demonstrated at 900 MHz. The 900 MHz ASK (Amplitude Shift Keying) modulated pattern signal was generated from the vector signal generator (N5182A, Agilent, USA) and transmitted to the BES antenna. The transmitting power was set to 0 dBm, and the data rate was 1 Mbps. The stent antenna is connected to the 50 Ω terminated oscillator. The transmitted and received signal were confirmed using oscilloscope (MSO-X 6004A, Agilent, USA) as shown in Figure 4.12h.

In vivo wireless power and data transmission from the transmitting antenna to the stent antenna is measured inside a canine common carotid artery. The stent connected to the coaxial cable is deployed into the common carotid artery. All the experiments are carried out after the blood flow is recovered. The results show the feasibility of the stent antenna for wireless power/data transfer applications.

FEM of temperature distribution near the stent during the NIR laser exposure: Multiphysics FEM simulation is also performed *via* COMSOL4.2 to study the temperature distribution of layers near the stent during NIR-induced photothermal heating with and without the blood flow. Since only a small part (1.3 mm × 1.7 mm) of the bottom PLA layer with AuNR@MSN can generate heat during NIR laser exposure due to the small NIR laser beam spot size, instead of modeling the whole stent inserted into blood vessel, we only model the part around the heated AuNR@MSN/PLA layer in a cylindrical coordinate system (Figure 4.23a) and assign infinite elements along both blood flowing direction and tissue thickness direction (Figure 4.23b). For the part covered by the stent, there are 6 layers in total from inner to outer radius: blood, top ceria NP/PLA layer, ZM21 alloy, bottom AuNR@MSN/PLA layer, intima and subendothelial tissue; for the part not covered by the stent, there are only 3 layers: blood, intima and subendothelial tissue. Except for the blood, all the materials are treated as solid such that the governing equation of heat transfer in PLA, ZM21, intima and tissue is

$$\rho C \frac{\partial T}{\partial t} = k \nabla^2 T \qquad \text{(S1)}$$

where T is the temperature field, ρ denotes the mass density, C the specific heat capacity, and k the thermal conductivity of the materials in each layer as listed in Table S1. The blood is modeled as a fluid, the governing equation of heat transfer is

$$\rho C\left(\frac{\partial T}{\partial t} + \boldsymbol{v} \cdot \nabla T\right) = k\nabla^2 T \quad \text{(S2)}$$

where $\boldsymbol{v}$ is the blood flowing speed which can be simplified as

$$\boldsymbol{v} = v\boldsymbol{n} = 2v_{avg}\left(1 - \frac{r^2}{R^2}\right)\boldsymbol{n} \qquad \text{(S3)}$$

where $\boldsymbol{n}$ is a unit vector pointing in the axial direction of the blood vessel, v_{avg} is the average flow rate of blood, R is the vessel inner radius and r is the radial coordinate. The thermophysical properties and the thickness of each layer are summarized in Table S1.

Table S1. Thermophysical property values and layer thickness

	h (μm)	C (J kg^{-1} K^{-1})	k (W m^{-1} K^{-1})	ρ (kg m^{-3})
Blood	1780 or 2000*	3617	0.52	1050
Top PLA	10	1800	0.13	1250
ZM21 alloy	200	1025	159	1780
Bottom PLA	10	1800	0.13	1250
Intima	600	3306	0.46	1102
Subendothelial Tissue	3000+infinite element	3421	0.49	1090

*Thickness for the part with or without stent.

Assuming the temperature of PLA layer with AuNR@MSN is 47 °C during NIR exposure and body temperature is 37 °C (i.e. boundary condition for these infinite elements is T = 37 °C), we obtain the temperature distribution in equilibrium state with different blood flowing rate: v_{avg}=120 mm/min and 0 mm/min and the overall temperature distribution when the system reach equilibrium state for each v_{avg} as shown in Figure 4.23c,d, respectively. Comparing the two figures, it is concluded that blood flow is effective in reducing the temperature in the blood itself and the neighboring stent area but not so effective in reducing the temperature of the intima which is directly covered by the stent because this part of the intima is not in direct contact with the blood.

BES deployment into the canine common carotid artery: These experiments are approved by the animal care committee at Seoul National University Hospital. An adult mongrel dog is used in this study. Surgery, angiography and stent deployment are performed with sterile techniques under general anesthesia. All the procedures are performed *via* the transcarotid route. After dissecting the neck area, the common carotid artery is exposed and a 8 Fr angiosheath is inserted into the common carotid artery to deliver the stent. The BES is loaded on the balloon catheter (Hyperglide, Covidian, Irvine, California, USA), move to the target site, and is deployed by the inflation of the balloon catheter. The radius and length of the deflated stent is 2.0 mm and 12.7 mm, respectively. The radius becomes ~3 times larger when the stent is inflated.

Computed tomography (CT) scan of the BES in the canine model: After stent deployment, computed tomography (CT) scan is performed by using High-Definition CT (HDCT: Discovery CT750 HD, GE Healthcare, WI, USA) under the following scanning conditions: 120 kVp, 350 mAs, 0.625 mm, 0.16 helical pitch, and 0.35 s gantry rotation speed. After pre-contrast CT acquisition, post-contrast CT is also obtained with injection of 60 mL of a noniodine contrast medium (Ultravist 370; Schering, Berlin, Germany) into an antecubital vein and this was followed by 40 mL of normal saline, both at a flow rate of 4 mL/s. Volume rendering CT images are reconstructed using 2.5 mm-thick axial images.

Reliability tests (retention, endurance) of RRAM: In the set/reset retention measurement, each resistance state is programmed and the current levels are measured at the read voltage of 0.2 V. Both HRS and LRS are well preserved for 10^3 s (Figure 4.7e). The read/write endurance measurement is conducted by the consecutive DC voltage sweeping from -2 V to 2 V. HRS and LRS current values measured at the voltage of 0.2 V are stable (Figure 4.7f).

Characterization of RRAM: The current-voltage measurement of RRAM is carried out in both the pristine and deformed condition on the balloon catheter. The electrical measurements are performed with the probe station and parameter analyzer (B1500A, Agilent, USA). I-V characteristics show no severe change when the stent is inflated (Figure 4.9b).

Characterization of temperature/flow sensor: The percent resistance change of the temperature/flow sensor is measured by a data-acquisition (DAQ) board run by the Labview software (National Instruments, USA). The plot of the percent resistance change as a function of the temperature change shows a linear function whose slope is 0.08%/°C (Figure 4.22b). Resistance changes at constant current induced by various flow rates (Thermal mass flow sensing) are measured in the extracted canine artery (*ex vivo*) by using a digital multi-meter (DMM) run by the Labview software. The temperature/flow sensors are encapsulated by MgO and PLA layers to prevent the leakage current in the fluid.

Custom-made data analysis and storage system: The measurement, data analysis, and data storage process begin with measuring the flow rate by using the flow sensor. Then, the Labview software (Figure 4.10a,b) is used to process and store the recorded data in RRAM cells. For example, in case of flow sensing for the cardiovascular model (Figure 4.3h-j), the flow rates are recorded by the onboard flow sensor, then the data ($\Delta R/R_0$) are classified into four different bands (0–0.03 mL/min, 0.03–0.5 mL/min, 0.5–0.8 mL/min, and >0.8

mL/min). The software determines the appropriate compliance currents and biasing voltages to write a specific two digit code ([00], [10], [01], and [11]), which is assigned to each band, to the RRAM cell.

Synthesis of ceria nanoparticles (NPs): The ceria NPs are synthesized by following previously reported literature.[10] Cerium (III) acetate (0.4 g, 98%, Sigma Aldrich, USA) and oleylamine (70%, 3.2 g, Acros, USA) are added to 15 mL of xylene (98.5%, Sigma Aldrich, USA). The solution is stirred for 2 hours at room temperature and then heated to 90 °C (2 °C/min). A 1 mL of deionized water is injected into the solution at 90 °C under vigorously stirring. The solution color then changes to the off-white color, showing that the reaction has occurred. The mixture is stored at 90 °C for 3 hours and then turns into a light-yellow colloidal solution, which is then cooled down to room temperature. Acetone is added to precipitate ceria NPs for washing and the ceria NPs are dispersed in chloroform. To make bioinert ceria NPs, organic-dispersed ceria NPs are coated by a PEG-phospholipid. 50 mg of mPEG-2000 PE (Avanti, USA) dissolved in 5 mL of $CHCl_3$ is added to 5 mL of ceria NPs solution (10 mg/mL in $CHCl_3$). Solvent is evaporated by rotary evaporator and products are aged at 80 °C in vacuum oven for another 1 h. Then, 5 mL of solvent (deionized water or $CHCl_3$, depend on usage) is added to the products, and excess amount of PEG-phospholipid is removed by ultracentrifugation.

Characterization of ceria NPs: TEM images are collected by using a JEM-2010 (JEOL, Japan) electron microscope operated at an accelerating voltage of 200 kV. The samples for the TEM analysis are prepared by dipping the copper grid coated with the amorphous carbon film in a solution containing the ceria NPs. Elemental analysis is performed by using an inductively coupled plasma atomic emission spectrometer (ICP-AES, ICPS-7500, Shimadzu, Japan).

Reactive oxygen species (ROS) scavenging activity of ceria NPs: The ROS scavenging activity of ceria NPs embedded in the PLA films are measured by a superoxide dismutase assay kit (Sigma Aldrich, USA) (Fig. 4c). The procedure is as follows: Ceria NPs solutions of various concentrations are mixed with PLA solution (45 mg/mL) and poured into a stainless dish, followed by drying over 24 h at room temperature. 200 μL of the assay kit solution and 20 μL of the xanthine oxidase solution are added to ceria NPs/PLA film. The sample is then incubated at 37 °C for 1 hour. After the centrifugation, the absorbance of the supernatant at 450 nm is measured using a micro plate reader (Victor x4, Perkins Elmer, USA).

Synthesis of gold nanorods (AuNR): The AuNR are prepared by following a previously reported literature.[11] The Au seed particles are prepared by adding 0.25 mL of 10 mM aqueous solution of $HAuCl_4 \cdot 3H_2O$ (99.9%, Strem, USA) to 7.5 mL of 100 mM cetyltrimethylammonium bromide (CTAB, 99+%, Acros, USA) under the mixing condition. Adding 0.6 mL of ice-cooled 10 mM $NaBH_4$ solution and stirring for 2 min results in a pale-brown seed solution. The AuNR growth solution is prepared by mixing 160 mL of 100 mM CTAB, 6.8 mL of 10 mM $HAuCl_4 \cdot 3H_2O$ and 1 mL of 10 mM $AgNO_3$ (99%, Sigma Aldrich, USA). Then, 1.08 mL of 100 mM L-ascorbic acid (99%, Sigma Aldrich, USA) is added, which changes the solution's color from the yellowish brown to colorless. To initiate the growth of nanorods, 1.68 mL of the seed solution is added to the growth solution and left still for 3 hours. To make PEGlyated AuNR for the *in vivo* experiment, AuNR are centrifuged twice and dispersed in 10 mL of water. Then, 100 mg of mPEG-SH 5000 (Sulfhydryl terminated, Sunbio, Korea) is added and stirred for 12 h. Excess amount of mPEG-SH is removed by centrifugation, and AuNR are filtered and redispersed in water.

Characterization of gold nanorods (AuNR): Transmission electron microscopy (TEM) images are collected by using a JEM-2010 (JEOL, Japan) electron microscope operated at an accelerating voltage of 200 kV. The samples for the TEM analysis are prepared by dipping a copper grid coated with the amorphous carbon film in a solution containing the AuNR. The UV-Vis absorption spectra are taken with the Cary 5000 UV-VIS-NIR (Agilent, USA) spectrophotometer.

Synthesis of gold nanorod@mesoporous silica nanoparticles (AuNR@MSN): The core/shell structure of AuNR@MSN is based on the modification of a previous report.[12] As the synthesized AuNR solution is centrifuged, washed and redispersed in 40 mL of water. CTAB (0.08 g, > 99%, Acros, USA) and 0.24 mL of NaOH solution (2 M) are added to the solution. Then, the solution is heated up to 70 °C, followed by adding 1.2 mL of mesitylene (99%, Sigma Aldrich, USA), 0.4 mL of tetraethyl orthosilicate (TEOS, 98%, Acros, USA), and 2.4 mL of ethyl acetate, sequentially. After stirring for 3 hours, the resulting AuNR@MSN is collected through centrifugation and washed with copious amounts of water and ethanol. Then, the pore-generating template, CTAB, is removed by stirring in an acidic ethanol solution. For the surface functionalization, AuNR@MSN is redispersed in 25 mL of ethanol. After the addition of 0.1 mL of 3-aminopropyltriethoxysilane (APTES, 99%, Sigma Aldrich, USA), the solution is refluxed for 3 hours.

Amine-functionalized AuNR@MSN (AuNR@MSN-NH_2) is centrifuged and redispersed in 5 mL anhydrous ethanol. To introduce PEG encapsulation onto the surface of AuNR@MSN, 100 mg of mPEG-SG 5000 (Succinimidyl glutarate terminated, Sunbio, Korea) is added and stirred for 12 h. After reaction, excess amount of mPEG-SG is removed by centrifugation, and product is dispersed in $CHCl_3$. The final concentration of Au measured by ICP-AES is 2.878 mg/mL.

Characterization of AuNR@MSN: TEM images are collected by using a JEM-2010 (JEOL, Japan) electron microscope operated at an accelerating voltage of 200 kV. Nitrogen adsorption/desorption isotherms are measured at 77 K using a gas sorption analyzer (ASAP 2020, Micromeritics, USA). The optical absorption spectrum is obtained using a UV-VIS-NIR spectrophotometer (Cary 5000e, Agilent, USA).

Hyperthermia activity of AuNR@MSN: When the NIR laser is exposed to trigger the hyperthermia activity, AuNR@MSN embedded in the PLA layer generates the heat. The increase of the temperature is measured by using the integrated bioresorbable Mg temperature sensor. Since the exposed area to the NIR laser spot is a part of the sensor, the temperature-resistance relationship needs to be corrected by multiplying with the areal factor, $A = \frac{Area_{\exp osed}}{Area_{total}}$.

The exposed region is 18% of total area (Figure 4.22a) in consideration of entire area of temperature sensor and the area of NIR laser spot. Since A=0.18 and α =0.08%/°C (Temperature sensitivity, Figure 4.22b), the modified temperature sensitivity factor (α ′) is A×α = 0.014%/°C.

***In vivo* experiment of NIR- and RF magnetic field-induced heat generation and heat-induced acceleration of drug diffusion:** After an 8 Fr angiosheath is inserted into the common carotid artery to deliver the stent, the BES is loaded on the balloon catheter, delivered to the target site, and is deployed by the inflation of the balloon catheter. To examine photothermal effect using optical-fiber-guided NIR, dye (Nile red, Sigma Aldrich, USA) and AuNR@MSN-coated stent were prepared and the NIR laser was irradiated onto the stent. Temperature of the stent was measured by IR camera and set to 40 °C. To demonstrate heat-induced dye diffusion *in vivo* the guided NIR laser beam was irradiated for 10 minutes. Series of experiment were also performed using RF induction heating system (Easyheat 0112, Ambrell, USA).

1.3 Result and Discussion

Multifunctional bioresorbable electronic stent (BES)

Figures 4.1a,b show a schematic diagram and a corresponding image of a representative bioresorbable electronic stent (BES) that includes magnesium alloy stent integrated with ceria NPs (catalytic ROS scavenging), AuNR@MSN (photothermal therapy), drugs (*e.g.* Rapamycin; well-known drug for the treatment of restenosis[3] with some dysfunctions[24]), flow/temperature sensors (physiological signal sensing) and RRAM array (data storage). These components consist of bioresorbable and bioinert materials (see Fig. 4.3a). Although the Mg alloy stent has rapid erosion problems,[25] the degradation time can be prolonged by multi-stacked encapsulation layers. Moreover, it is necessary to use conductive Mg-based stent strut for the system which acts as an antenna unit for wireless electronics. Details of the fabrication processes, materials, geometrical information, and images of the BES are included in Supporting Information (SI) and Figure 4.2a. Figure 4.1b shows the BES (in deflated state) ready to be deployed in a canine common carotid artery *in vivo via* arterial access. The bottom inset is a magnified image of the BES, showing RRAM and a temperature sensor, coated with nanoscale therapeutic agents. Figure 4.1c shows x-ray images of a deflated (left) and inflated (right) balloon catheter used to deploy the BES. The inflated BES mechanically supports the artery. An optical image (Figure 4.1d) and a volume-rendered computed tomography (CT) image (Figure 4.1e) highlight the expanded BES deployed inside the targeted artery.

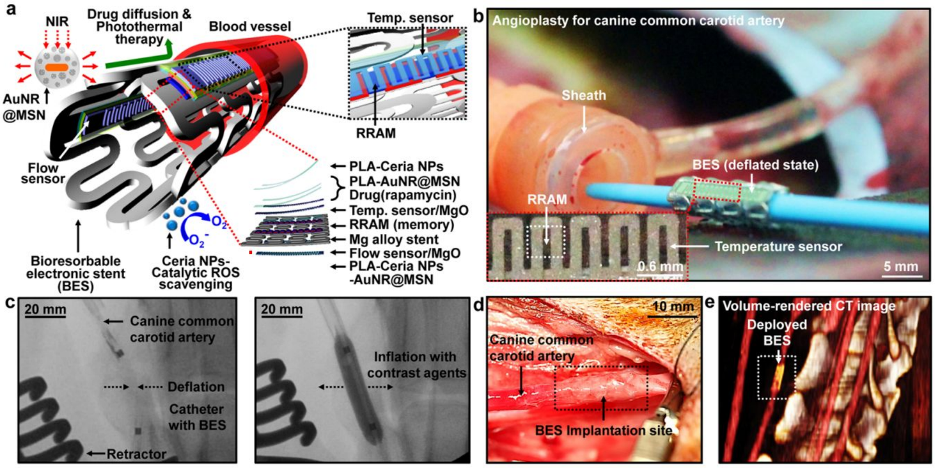

Figure 4.1 Bioresorbable electronic stent (BES). a, Schematic illustration of the BES (left), its top view (top right), and the layer information (bottom right). The BES includes bioresorbable temperature/flow sensors, memory modules and bioresorbable/bioinert therapeutic nanoparticles. The therapeutic functions are either passive (ROS scavenging) or actively actuated (hyperthermia-based drug release) by the NIR exposure. **b,** Image of the BES installed on the balloon catheter during the deployment into a canine common carotid artery *in vivo*. Inset (bottom) shows the RRAM (white dotted box) and the temperature sensor on the BES. **c,** X-ray images of the balloon catheter and the BES in the canine model before (left) and after (right) the inflation of the balloon catheter. **d,** Image of the deployed BES in the canine common carotid artery *in vivo*. **e,** Volume-rendered X-ray computed tomography (CT) image of the deployed BES in the canine common carotid artery.

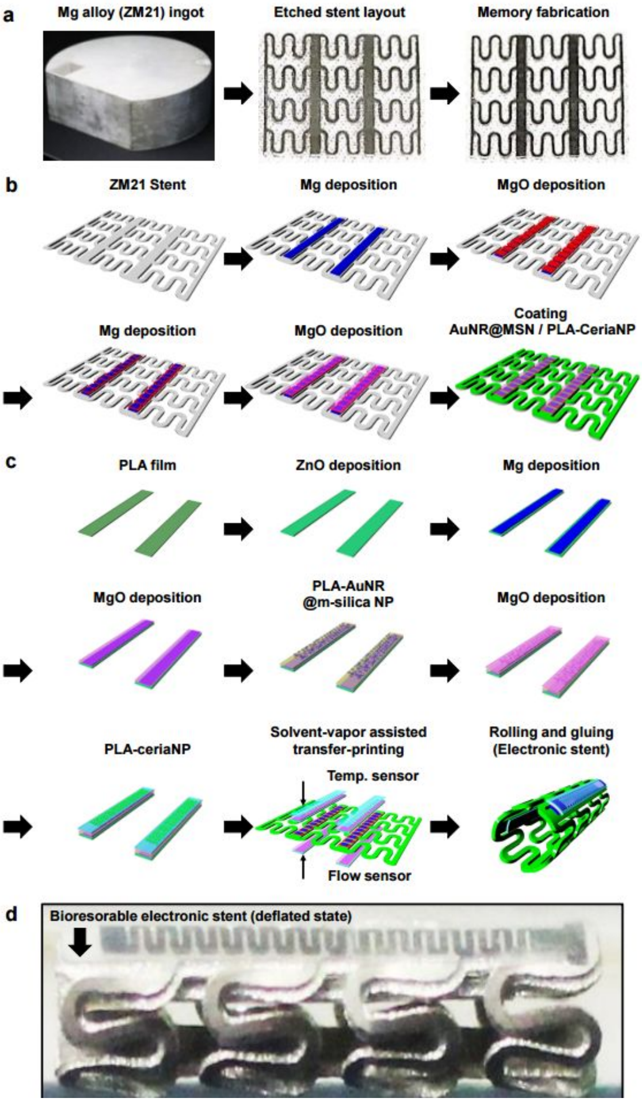

Figure 4.2 a, Optical images of the stent strut during the fabrication from an Mg alloy ingot. **b,** Schematic diagrams illustrating the fabrication process of the bioresorbable RRAM array on the stent. **c,** Schematic diagrams illustrating the

fabrication process of the temperature/flow sensors on the stent. d, Magnified image of fabricated bioresorbable electronic stent (BES).

Materials biocompatibility and structure of the bioresorbable electronic stent (BES)

Most of bioresorbable stents for endovascular diseases lack the multifunctionality, such as continuous monitoring, data storage, and instantaneous therapy, due to unavailability of integration processes of multifunctional device components. Specifically, the integration of bioresorbable active/passive devices on the stent has not been feasible, because the fabrication process of the bioresorbable electronics is incompatible with the conventional microfabrication processes. Figures 4.3a shows an illustrative enumeration for bioresorbable and bioinert stacks of active electronics and therapeutic nanoparticles on a Mg-Zn-Mn alloy (ZM21; Mg 97%, Zn 2%, Mn 1%) strut. These electronic components consist of bioresorbable (Mg,[12,26-28] MgO,[12,27] Zn,[26,28] ZnO[29] and poly-(lactic acid) (PLA)[30]) and bioinert (Mn[28]) materials (see Experimental section). Therapeutic nanoparticles (ceria NPs and AuNR@MSN) and drugs are also incorporated in the PLA layers of the stent coated with dissolution-rate-controllable oxide/polymer, which plays a crucial role in reducing the fast corrosion rate of the stent strut and active electronic components (Figure 4.2a). All the used nanoparticles are either bioresorbable (SiO_2[31]) or bioinert (CeO_2,[18] Au,[32]). Detailed average amount of each component is as follows: 27.4 mg of ZM21 stent strut, 3.4 mg of electronic devices on PLA films, 0.51 mg of ceria nanoparticles, 0.16 mg of gold nanorod core and 0.54 mg of silica shell. The amount of electronic devices on the stent is less than 0.1 mg. The rate of degradation of the active agents (in response to biofluid immersion) is illustrated in Figure 4.2b, which can be controlled by tuning the geometry and materials of encapsulating oxides (*e.g.* MgO) and polymers (*e.g.* PLA, silk[33,34]).

Besides the bioresorbability, a key criterion for effective clinical treatments is the compatibility of bioinert nanomaterials with *in vivo* models. Although bioinert nanoparticles are slowly released from the PLA polymer, overdosed nanoparticles are used to confirm their biocompatibility. Bioinert nanoparticles in excess amounts (5 mg Au/kg and 2.5 mg Ce/kg) are injected through the tail vein of the normal mice to evaluate the effect to the internal organs. *In vivo* pharmacokinetic studies in mice show that ceria NPs, AuNR@MSN and AuNR have half-lives of 1.9 h, 5.5 h, and 1.2h (Figure 4.3b), which are similar with previous reports.[35] These results show that nanoparticles do not exhibit severe interactions with proteins and plaques that shorten half-lives in the bloodstream. Biodistribution studies show the accumulation of bioinert nanoparticles in the reticuloendothelial system such as the spleen, liver, and lymph node rather than in lung and other organs, as commonly observed[36,37] (Figure 4.3c). The histological analysis (Figures 4.5,6) shows the biocompatibility of nanoparticles.[38] These corroboratively show that the influence of bioinert nanoparticles to *in vivo* system is minimal. The mechanical strength and structural integrity of bioresorbable stent mainly depends on the mechanical property of the stent strut. The current bioresorbable stent is composed of ZM21 alloy which is known to its reliable corrosion resistance. The alloy that composes the strut can be changed with other Mg alloy (*e.g.* WE43) to further strengthen the mechanical and chemical properties. We found that the mechanical strength and structural integrity was maintained for a week *in vivo*.

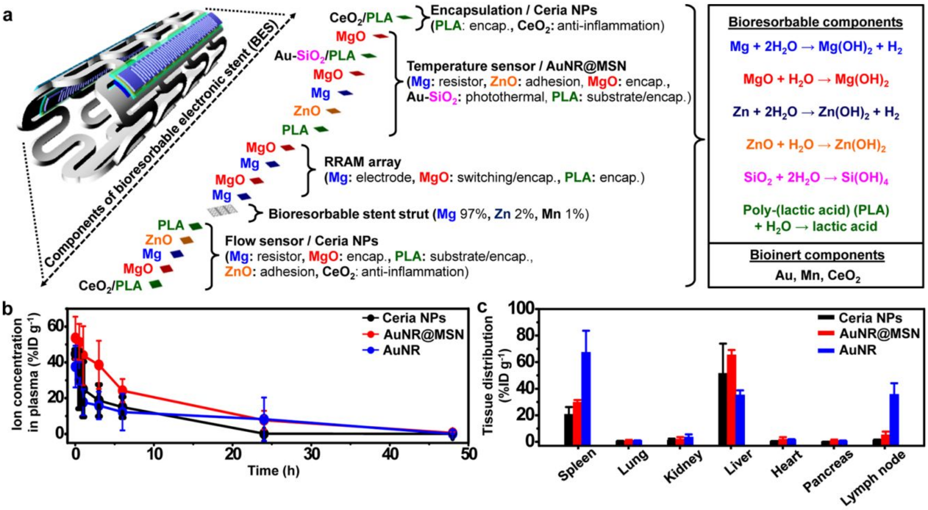

Figure 2.3 Bioresorbable and bioinert materials of the BES. a, Bioresorbable and bioinert components of the BES, shown as exploded view (left) and their hydrolysis (right). **b,** Blood circulation data (ion concentration in plasma *versus* time) of ceria NP, AuNR@MSN, and AuNR injected into 8 weeks-old BALB/c mice (n = 3 for each nanoparticle group, 5 mg of Au or 2.5 mg of Ce per kg of mouse body weight). **c,** Biodistribution profiles of ceria NP, AuNR@MSN, and AuNR injected into 8 weeks-old BALB/c mice (n = 6 for each nanoparticle group, 0.0625 mg of Ce or 0.125 mg of Au per mouse).

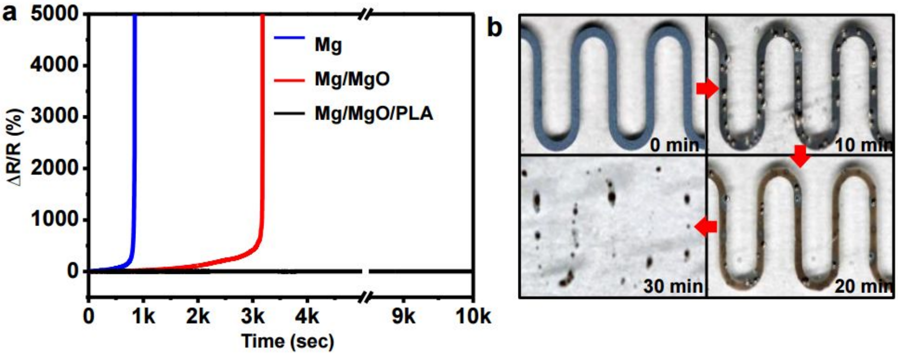

Figure 2.4 a, Plot of the percent resistance change of the Mg metal line (100 nm) as a function of time, in a phosphate-buffered solution (PBS) with different encapsulation materials (blue: No encapsulation, red: MgO 300 nm, black: MgO 300 nm / PLA 120 mm). The one with the PLA encapsulation maintains the original conductivity for several tens of days. **b,** Optical images of serpentine shaped Mg (50 nm) metal interconnects in PBS for every 10 minutes.

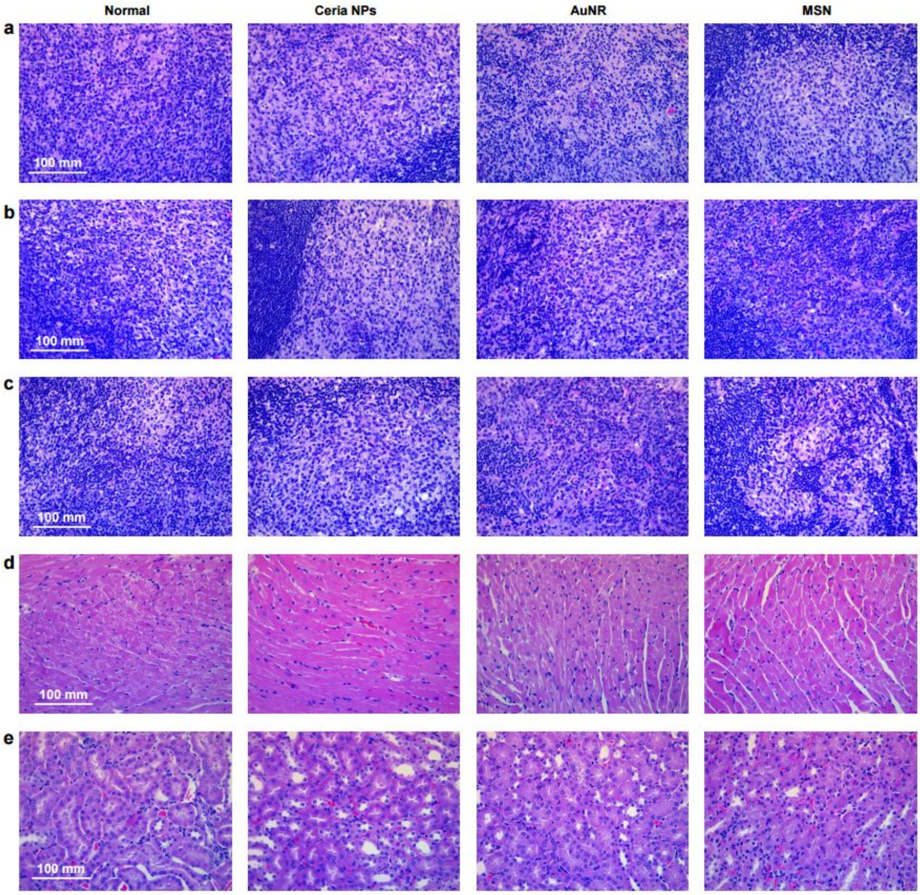

Figure 2.5 Hematoxylin and eosin (H&E) stained histological image of the various organs of the mice, which the bioinert nanoparticles in excess amounts are injected via the tail vein. **a,** axillary lymph node **b,** brachial lymph node **c,** inguinal lymph node **d,** heart **e,** kidney.

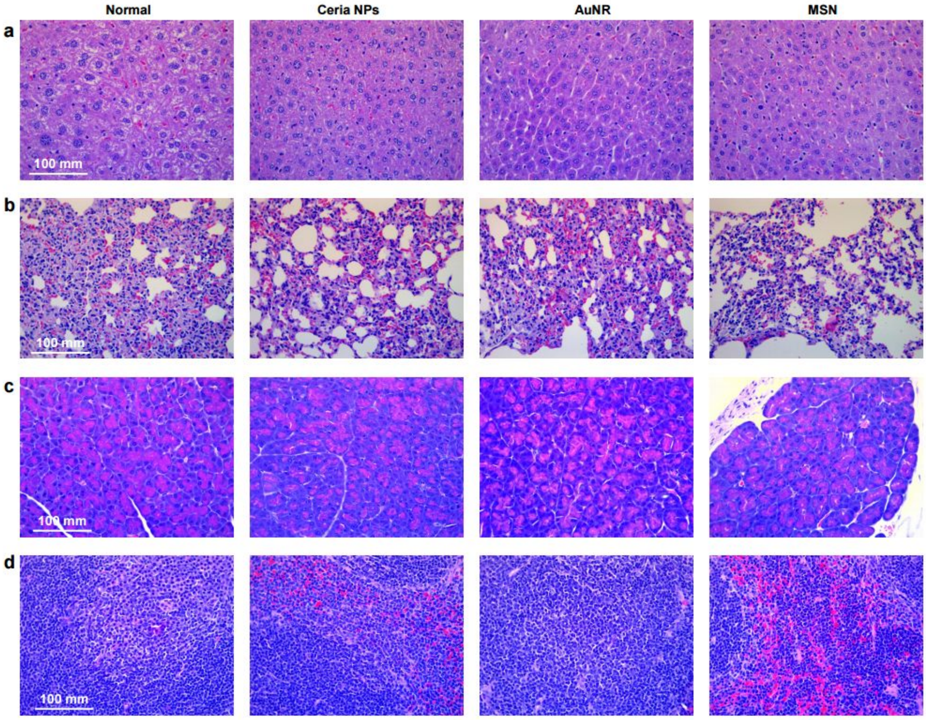

Figure 2.6 Hematoxylin and eosin (H&E) stained histological image of the various organs of the mice, which the bioinert nanoparticles in excess amounts are injected via the tail vein. a, liver b, lung c, pancreas d, spleen.

Electrical function of the bioresorbable electronic stent (BES)

Figure 4.7 shows results of active electronics in sensing, storing data from the BES. A bipolar I-V curve for the bioresorbable Mg/MgO/Mg nanomembrane resistance memory device shows how the device bi-directionally switches between a low-resistance state (LRS) and a high-resistance state (HRS) (Figure 4.7a). The resistive switching is achieved by applying a positive voltage ("reset" of 0.7 V) or a negative voltage ("set" of -0.8 V). The low reset and set voltages enable low-power operations of the memory. The inset of Figure 4.7a shows the switching sequence. Figure 4.7b is a transmission electron microscope (TEM) image of a memory module, highlighting the MgO nanomembrane switch layer (~12 nm) and interfaces to Mg electrodes. A switching mechanism of the RRAM is detailed in Experimental section. The area-independent current values for both the LRS and HRS suggest that the conducting mechanism is driven by the filamentary connection (Figure 4.7c).[39] The Mg/MgO/Mg RRAM is characterized by bipolar resistive switching behaviors typically observed in a memristor. Figure 4.7d shows uniform resistive switching in the RRAM array, where both the HRS and LRS are stable. The retention property of these devices can be extrapolated for up to several years (Figure 4.7e) with switching cycles exceeding 1,000 times (Figure 4.7f). The multi-level cell (MLC) operation and its mechanism are shown in Figure

4.8a-b and c, respectively. Mechanical robustness during expansion of the BES is confirmed using finite element modeling (FEM) analysis. We estimate the strain in the switching layer (MgO nanomembrane) of the BES (Figure 4.7g), less than the fracture strain of MgO (~8%).[40] Nanometer-thick active layers and serpentine designs incorporated in the BES (Figure 4.9a) minimize the effect of induced strains and the flexibility is not affected, allowing for stable I-V characteristics under deformations (Figure 4.9b).

The bioresorbable RRAM is coupled with a sensor module on the BES in order to store sensing data. Figure 4.7h shows the BES in an *ex vivo* intravascular flow/perfusion model. A canine aorta (Figure 4.7h) is resected and the BES is inserted in the path of simulated blood flow. The thermo-resistive flow sensor on the stent is operated by measuring changes of resistance, which in turn correlate with changes in fluid velocity (Figure 4.7i). The RRAM modules store this flow data based on 4-level data groups that correspond to flow rate changes. These rate changes are stored *via* the MLC operation (Figure 4.7j, 4.8b). Each fluid velocity is stored in a different cell of the memory in real time by using the custom-made Labview software (Figure 4.10). Furthermore, the wall shear stress distributions, which are related to the restenosis process,[41] are simulated by 3D computational fluid dynamics (CFD) (Figure 4.11).

For wireless power/data transmission, we first investigate the reflection coefficients of a stent antenna at the port impedance of 50 ohm (Figure 4.7k). S_{11} of the BES strut at telecommunication band (900 MHz) is -15 dB. Since the BES strut is composed of highly conductive magnesium alloy, majority of the oscillating electric power is radiated to the external space, and thereby the stent strut can be used as the bioresorbable antenna.

With the stent and the transmitting antenna, Power transfer efficiency (S_{21}) from the transmission antenna to the stent antenna when they are separated by ~1 cm is -20.16 dB (*ex vivo,* Figure 4.12g) and -21.80 dB (*in vivo,* Fig. Figure 4.7l) at 900 MHz (detailed antenna characteristics and corresponding simulations for the analysis are included in the Experimental section). S_{21} varies from -21.80 to -29.86 dB for the distance of 1 ~ 5 cm. The wireless data transmission is also tested. The 900 MHz ASK (Amplitude Shift Keying) modulated pattern signal (1 Mbps) is generated and successfully transmitted to the BES antenna *ex vivo* (Figure 4.12h) and *in vivo* (Figure 4.7m). The power[12,27,42] and the data[43-45] can be transmitted more efficiently by impedance matching *via* the on-chip implementation of bioresorbable circuit components, such as lumped inductors and capacitors. In addition, more complex bioresorbable circuit components, such as rectifiers, oscillators and modulators, can be integrated to establish the passive RF-communications. A bioresorbable battery[46] can also be used for the energy storage. The BES equipped with functional sensors, memory modules, wireless units are very important to facilitate practical PEI applications.

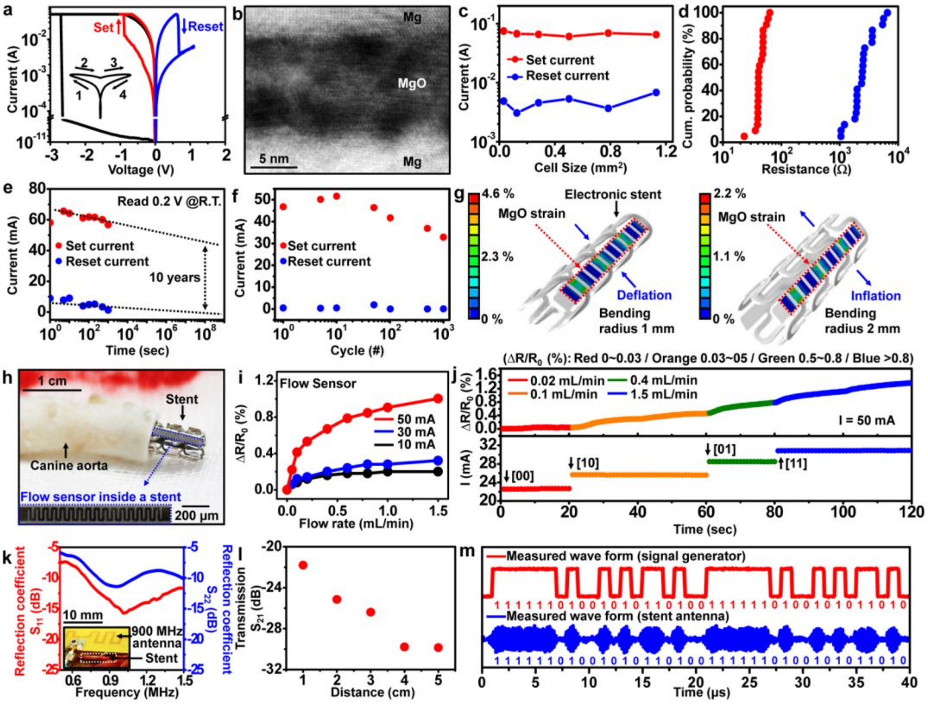

Figure 2.7 Electrical, mechanical and wireless characteristics of the BES. a, Current-voltage (I-V) characteristics of the bipolar resistance memory of the Mg/MgO/Mg structure. **b,** Cross-sectional TEM image of the Mg/MgO/Mg memory cell. **c,** Dependency of the Set/Reset current on the size of the memory cell. **d,** Plot of the cumulative probability as a function of the Set/Reset resistance. **e,** Retention characteristics of the memory. LRS and HRS current data are obtained at +0.2 V. **f,** Endurance characteristics of the memory measured at +0.2 V. **g,** Finite element modeling (FEM) of the strain distribution at the active layer (MgO) of the memory. **h**, Image of the BES in the canine aorta for the *ex vivo* experiment of the blood flow sensing and the data storage in integrated memory devices. **i,** Plot of the percent resistance change of the flow sensor *versus* the flow rates at three different current levels of the flow

sensor. **j,** Plot of the percent resistance change of the flow sensor (top) (measured with the 50 mA constant current). The measured flow rates are converted into digital signals and then stored into memory cells through the multi-level cell (MLC) operation. **k**, Reflection coefficients of a stent antenna and a transmitting antenna in canine common carotid artery *in vivo*. Inset image shows wireless power/data experimental setup using a stent antenna and a transmitting antenna (900 MHz). **l**, *In vivo* transmission coefficient S_{21} between a stent antenna and a transmitting antenna at different distances. **m**, *In vivo* data transmission (1 Mbps) between a stent antenna and a transmitting antenna.

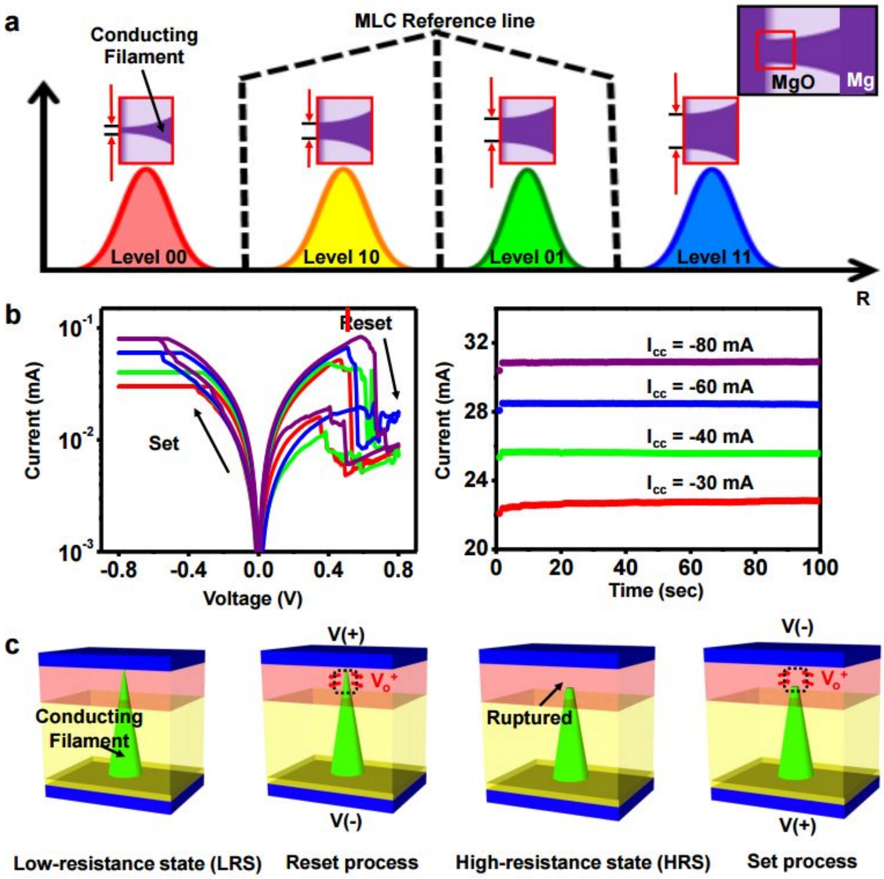

Figure 2.8 **a,** Schematic diagram describing the principle of conducting filament-based multi-level cell (MLC) operation. **b,** Current-voltage characteristics with different compliance currents (Icc) in Mg/MgO/Mg RRAM cells. **c,** Schematic diagram describing the resistive switching mechanism.

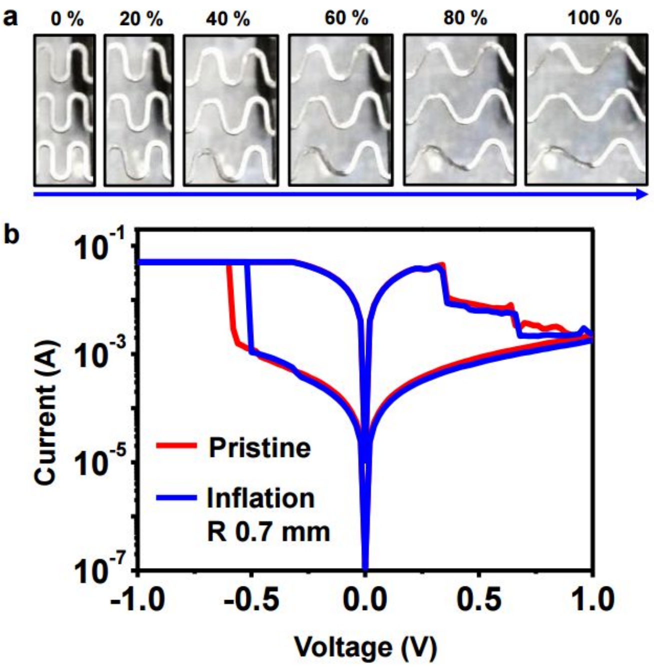

Figure 2.9 a, Stretched serpentine interconnections at various strains ranging from 0% to 100%. **b,** Current-voltage characteristics of the RRAM carried out in both the pristine (red) and deformed (blue) condition on the balloon catheter.

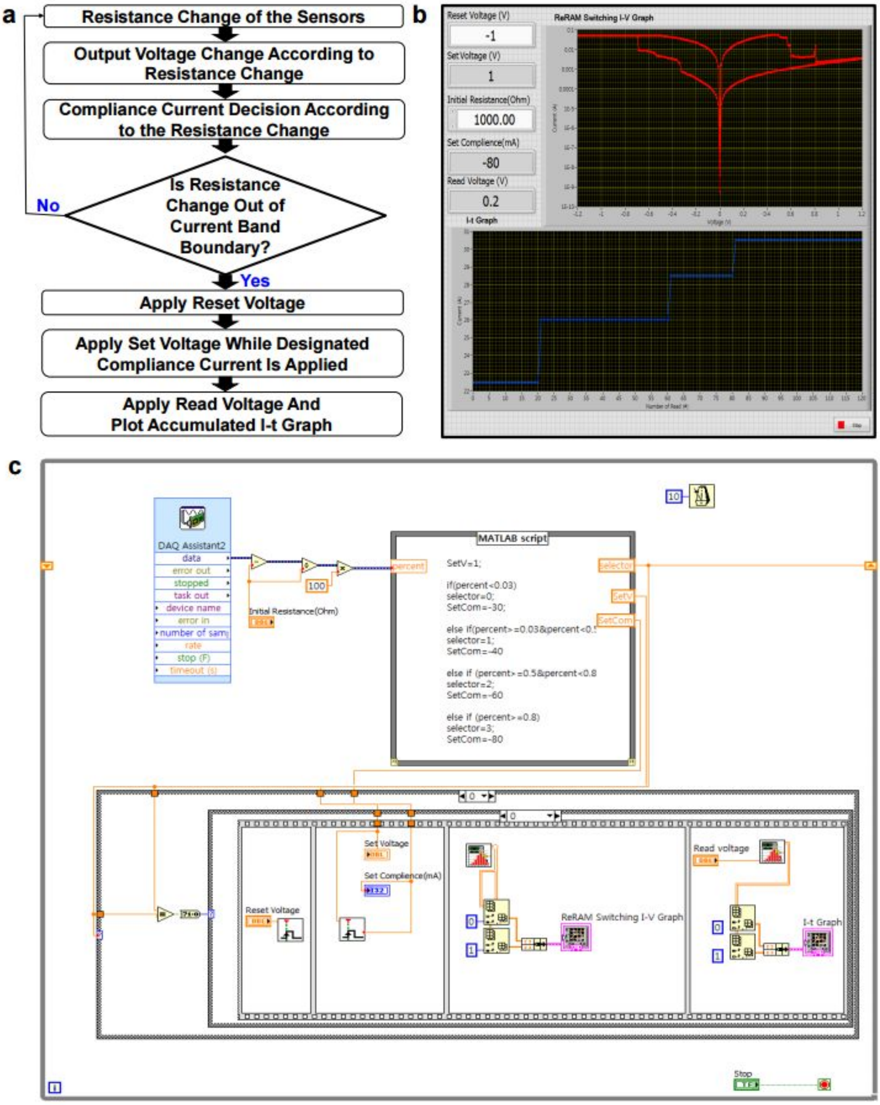

```
SetV=1;

if(percent<0.03)
selector=0;
SetCom=-30;

else if(percent>=0.03&percent<0.
selector=1;
SetCom=-40

else if (percent>=0.5&percent<0.8
selector=2;
SetCom=-60

else if (percent>=0.8)
selector=3;
SetCom=-80
```

Figure 2.10 a, Block diagram describing the sequences of the data sensing, processing and storage. **b,** Screen capture image of custom-made Labview software**. c,** Front panel of the custom-made Labview software.

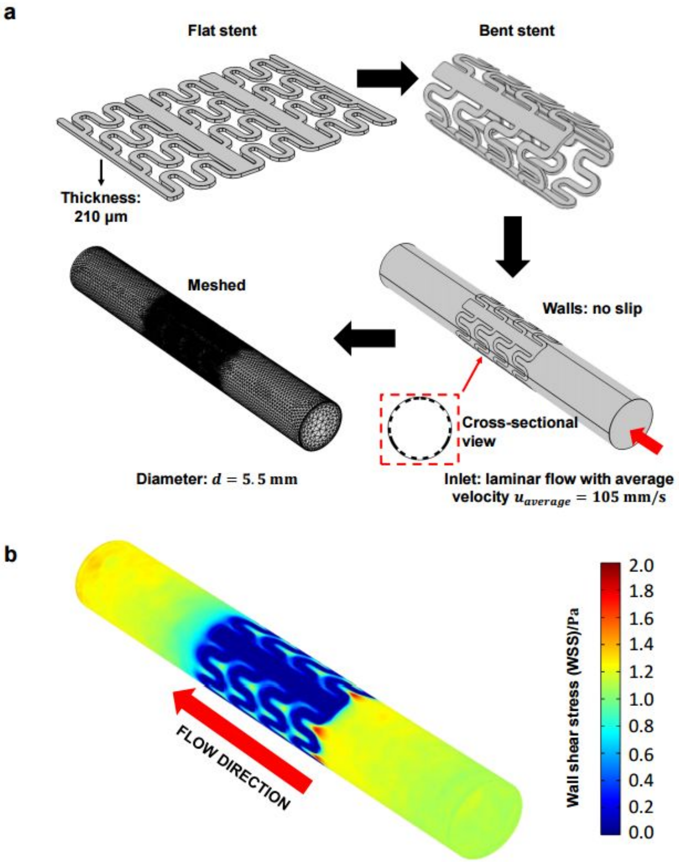

Figure 2.11 a, Modeling process for computational fluid dynamics (CFD) modeling. **b,** Shear stress distributions of blood vessel wall for an indicator of the flow pattern.

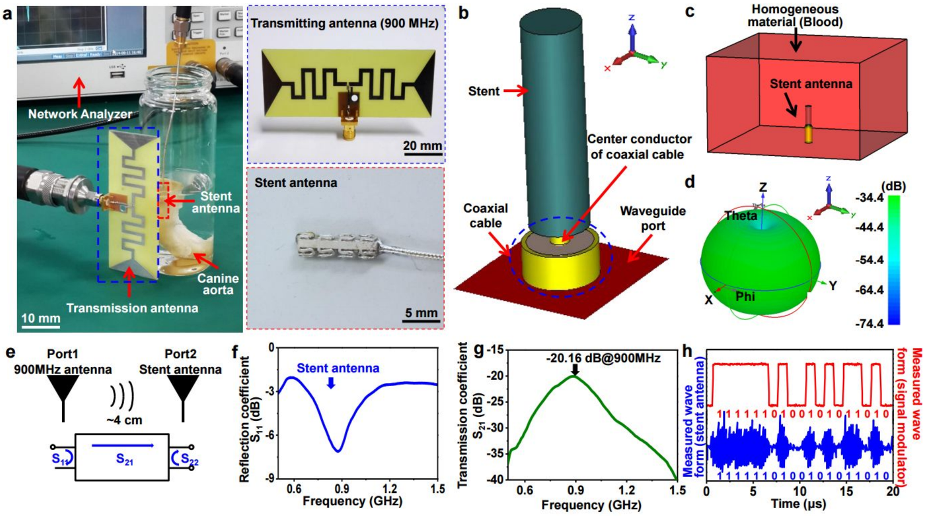

Figure 2.12 **a,** Ex vivo experimental images for wireless power/data transmission using the BES strut as an antenna. Magnified images of a 900 MHz transmission antenna with (blue dashed box, top right) and a stent antenna connected to the coaxial cable (red dashed box, bottom right). **b,** Schematic diagrams of the stent antenna connection. **c,** Simulation model for a stent antenna with the homogeneous metal (Mg) with surrounding blood**.** **d,** Estimated radiation pattern of the stent antenna**.** **e,** Schematic for the measurement setup of wireless power transfer efficiency**.** **f,** Reflection coefficient of a stent antenna in 1 M Phosphate buffered solution (PBS) which has similar electrical properties of the blood **g,** Transmission coefficient between a stent antenna and an external transmission antenna in 1M PBS

solution surrounded by dog’s aorta. **h,** Data transmission between the stent and the external transmission antenna ex vivo.

Reactive oxygen species scavenging effect

To deliver the therapy, we incorporated ceria NPs (Figure 4.13a and its inset for the magnified view) in the outermost encapsulation layer of the BES (Figures 4.1a and 4.13b left). Typically ROS near the implantation site promotes apoptosis of endothelial cells and ROS-induced inflammatory responses,[20,47,48] one of major causes of restenosis. It also causes the death of cardiomyocytes.[48] The presence of oxygen vacancies on the surface of ceria NPs induces the binding of ROS to ceria NPs. And then self-regenerative redox cycles between Ce^{3+} and Ce^{4+} oxidation states[18] allow the continuous catalytic scavenging of the endovascular ROS (Figure 4.13b right), suppressing ROS-induced inflammations. We used superoxide and hydrogen peroxide molecules to mimic increased ROS levels in cardiovascular systems during the angioplasty procedure.[48] Ceria NPs embedded in PLA film exhibit ROS scavenging activity in a dose-dependent manner (Figure 4.13c). We evaluated the antioxidative effects of ceria NPs *in vitro* by exposing human umbilical vein endothelial cells (HUVECs) to oxidative stresses (Figure 4.13d, 4.14). Once media containing ROS is added to the bath of the HUVECs, cell viability (in the absence of ceria NPs) decreases rapidly (Figure 4.13d left, 4.13e black curve). In contrast, the addition of ceria NPs embedded in PLA film improves the cell viability under oxidative stress (Figure 4.13d right and 13e red curve), indicating endothelial cells are protected by ceria NPs from ROS. Exposure of cardiac muscle cell lines, HL-1, in conjunction with ceria NPs yields similar reduction in oxidative stress, as in HUVECs (Figures 4.13f and g). We investigated the protective effect of ceria NPs in animal models by assessing anti-inflammation *in vivo*. Immunohistochemical analysis (Figure 4.15) following the BES implantation in the canine common carotid artery shows the suppression of inflammatory responses and macrophage migration in the presence of ceria NPs (Figure 4.13h) without other therapeutic agent, whereas microphage recruitment is observed in the absence of ceria NPs (Figure 4.13i).

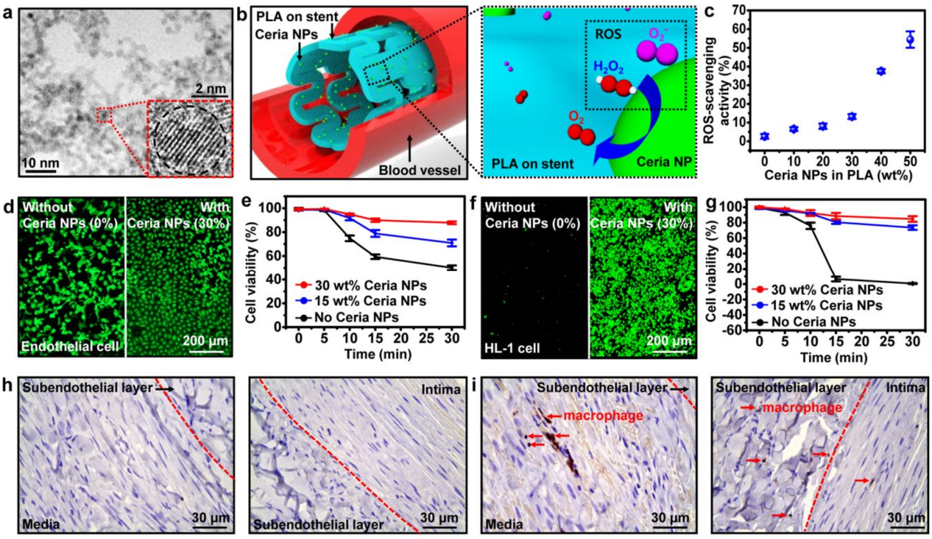

Figure 2.13 ROS scavenging effect of ceria NPs integrated on the BES. a, TEM image of ceria NPs. The inset shows a magnified image by the high resolution TEM. **b,** Schematic illustration of the ROS scavenging mechanism by ceria NPs. **c,** Plot of the ROS scavenging activity of the ceria nanoparticle-embedded PLA film with different ceria concentrations (standard deviation from the mean, n=3). The scavenging activity is measured by using the superoxide dismutase assay kit. **d,** Fluorescent images of HUVECs under 50 μM ROS, without (left) and with (right) ceria NPs *in vitro*. **e,** Cell viability of HUVECs with various ceria NPs concentrations under 50 μM ROS (standard deviation from the mean, n=3). **f,** Fluorescence images of mouse cardiac muscle cells (HL-1) under 50 μM ROS, without (left) and with (right) ceria NPs *in vitro*. **g,** Cell viability of HL-1 with various ceria NPs concentrations under 50 μM

ROS (standard deviation from the mean, n=3). **h,** *In vivo* immunolabeling image of MAC387 (macrophage) of the media and subendothelial layer (left) and subendothelial layer and intima (right) near the stent implantation site with ceria NPs. **i,** *In vivo* Immunolabeling image of MAC387 (macrophages) of the media and subendothelial layer (left) and subendothelial layer and intima (right) near the stent implantation site without ceria NPs.

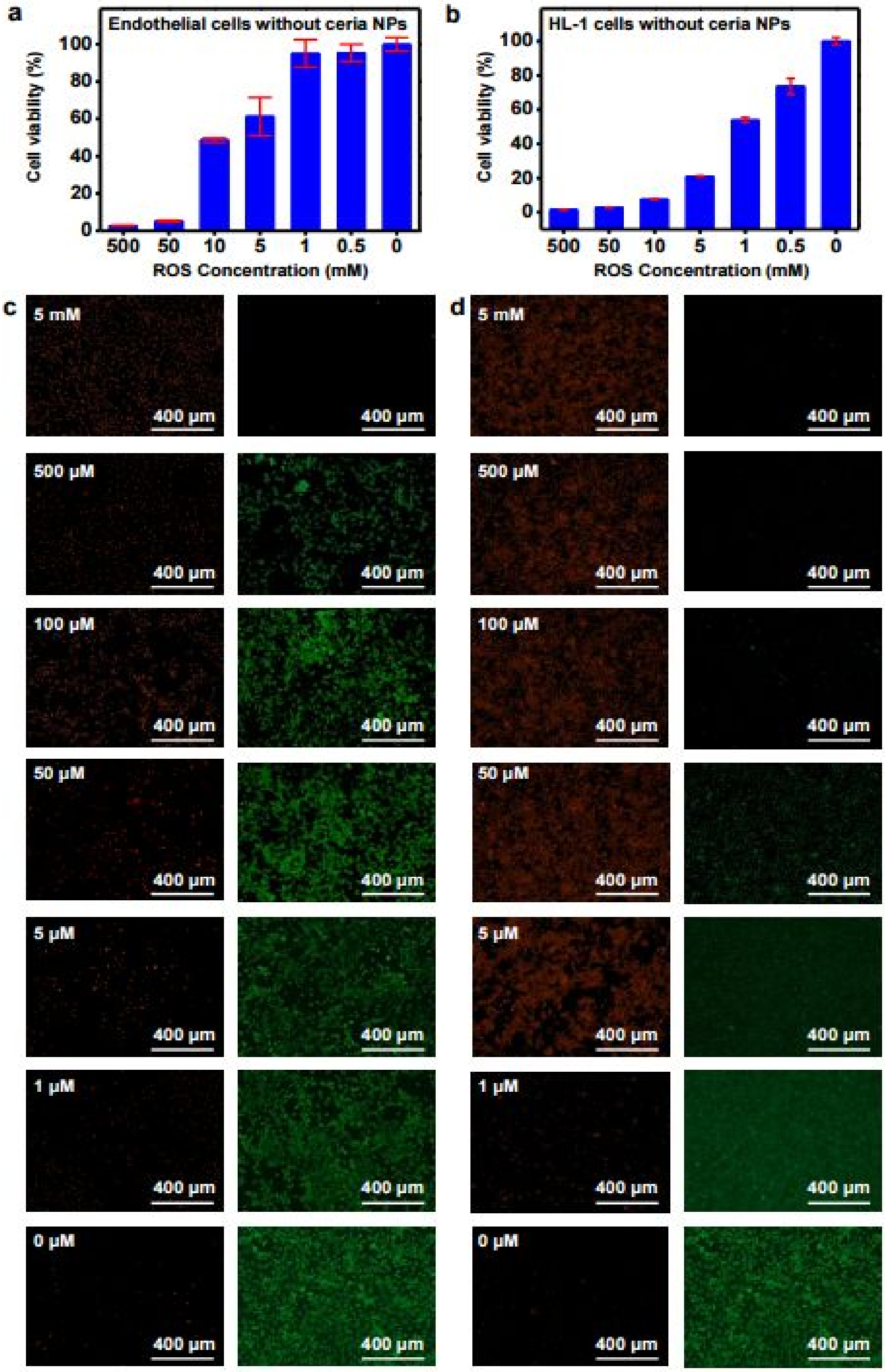
a
Endothelial cells without ceria NPs
Cell viability (%)
0
20
40
60
80
100
500
50
10
5
1
0.5
0
ROS Concentration (mM)
b
HL-1 cells without ceria NPs
Cell viability (%)
0
20
40
60
80
100
500
50
10
5
1
0.5
0
ROS Concentration (mM)
c
d
5 mM
500 μM
100 μM
50 μM
5 μM
1 μM
0 μM
400 μm

Figure 2.14 a, Plot of endothelial cell viability versus H2O2 concentration by MTT assay**. b,** Plot of mouse cardiac muscle cell (HL-1) viability versus H2O2 concentration by MTT assay**. c,** Fluorescent images of live/dead-stained endothelial and d, HL-1 cell at different H2O2 concentrations.

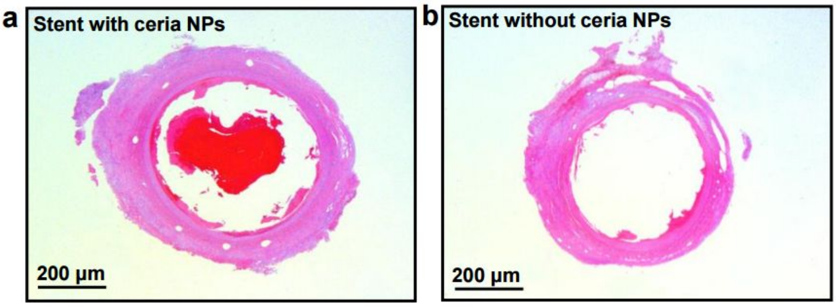

Figure 2.15 H&E stained histological image near the stent implantation site**. a,** The stent with ceria NPs. **b,** The stent without ceria NPs.

Hyperthermia-based controlled drug delivery

In addition to the protection against ROS and inflammations, multifunctional therapeutic nanoparticles responsive to external optical stimuli are also integrated on the BES to enable controlled drug release and photothermal therapy (Figure 4.17). Since drug-loaded nanoparticles are bound by PLA chains, the release rate is slow and thereby continuous/controlled nanoparticle-based therapy over extended period of time is possible. To achieve this form of actuation on the BES, we designed and synthesized nanoparticles containing NIR-responsive AuNR core (~20 nm length and ~10 nm diameter) and drug-loadable mesoporous silica shell (AuNR@MSN, diameters of ~100 nm) (Figure 4.16a).[22,23] The large surface area to volume ratio of AuNR@MSN[49] enables loading of large drug payloads (Rapamycin, LC Laboratories, USA) to sustain the long-term medication for the suppression of SMC proliferation and restenosis.[50] To promote sufficient adsorption of large molecular-sized drugs (Rapamycin), we increased the size of the mesopore by adding swelling agents (mesitylene, Sigma Aldrich, USA) (Figure 4.18a). N_2 adsorption/desorption isotherm analysis shows that AuNR@MSN has well-developed mesopores. The corresponding Barrett-Joyner-Halenda (BJH) pore size distribution indicates an effective pore diameter of ~3.9 nm (Figure 4.18b). UV-Vis adsorption spectrum indicates that AuNR@MSN has an adsorption peak at ~761 nm (Figure 4.18c). AuNR@MSN is responsive to NIR laser (~800 nm) that has high penetration depth through soft tissue,[22,23,51] and thereby it can be used for minimally- or non-invasive photothermal actuation of AuNR@MSN. Figure 4.16c highlights *in vitro* experiments of a drug release from AuNR@MSN in PLA with and without NIR laser (~800 nm) radiation. The AuNR core that absorbs NIR generates and transfers heat to the drug-loaded-mesoporous silica shell, which in turn, facilitates desorption and diffusion of loaded drug.[22,23] By modulating the NIR laser power, we controlled the dosage of drug released (Figure 4.16b) from the BES. Although the NIR beam guiding through the optical fiber to endovascular locations for photothermal therapies[52,53] is still challenging, the drug delivery induced by guided-NIR was successfully demonstrated through *in vivo* experiments (Figure 4.16c, 4.19). Furthermore, the radio-frequency (RF) magnetic field can induce heat on the stent for the accelerated drug diffusion (Figure 4.20,21). The hyperthermia-based drug delivery from the stent to the intima is evaluated through the *in vivo* animal experiment (Figure 4.16d).

Thermal mapping at intravascular sites is important to ensure precise drug release and to prevent the heat-induced cell necrosis. Because of the small areal coverage of NIR laser spot on the temperature sensor (~18% of total area of the temperature sensor, see Figure 4.22a), we applied a modified linear correlation

(~0.014 Ω/°C) for the temperature sensor (original correlation in Figure 4.22b). The photothermal experiment setup (Figure 4.22c) is further explained in Experimental section. To verify the effect of AuNR@MSN-based hyperthermia, we monitored the temperature relative to a control experiment (temperature sensor on the BES without AuNR@MSN). Results show a ~10 times increase in temperature changes by including AuNR@MSN (Figure 4.16e). The time dependent and NIR-intensity dependent temperature changes (monitored by the integrated temperature sensor) are shown in Figure 4.22d and e, respectively.

The temperature distribution near the BES and in the adjacent intima region must be precisely controlled to prevent the generation of heat-induced clotting or endothelial cell death. Numerical thermal analysis (Figure 4.16f, 4.23) shows the three dimensional thermal distribution near the heat focus area (~47 °C) generated by the NIR laser during occlusion (blood flow rate = 0 mm/s, Figure 4.23c) and reperfusion (blood flow rate = 2 mm/s, Figure 4.16f, 4.23d) conditions. Heating (maximum temperature ~ 47 °C) is significantly reduced by blood flow (Figure 4.23c and d), causing blood temperature near the BES to remain below ~43 °C. The temperatures in the intima and subendothelial layers in direct contact with the stent decrease nonlinearly with depth. Blood flow at 2 mm/s helps to further reduce the tissue temperature slightly (Figure 4.16g). Considering the thickness of intima (~600 μm),[54] the heat conduction to cardiac tissues is tolerated without severe decrease of cell viability and mainly localized to the intima.

Figure 4.16h-j show fluorescence images of HUVECs after exposure to NIR laser radiation with discrete laser power and associated temperature change (Figure 4.22d). HUVECs are dyed with LIVE/DEAD Viability/Cytotoxicity Kit (Life technologies, USA), consisting of calcein-AM (green color, dye for live cell) and ethidium homodimer-1 (red color, dye for dead cell). When 17 mW of NIR laser power is applied for 10 min, HUVECs remain alive, with some detectable photo-bleaching of green dye by the laser (Figure 4.16h). However, cell death onset occurs (red colored region) in response to 29 mW of NIR laser power (Figure 4.16i). As the NIR laser power is further increased to 40 mW, cell death expands to the surrounding region (Figure 4.16j). Quantitative analysis of cell viability as a function of laser power is shown in Figure 4.16k, which is consistent with the previous reports.[55] The utility of embedded temperature sensors on the BES can help mitigate cell injury and death during diagnosis and therapy. In addition, hyperthermia therapy is reported to prevent the accumulation of vulnerable plaques, which are prone to produce sudden risks, such as a heart attack or stroke.[56]

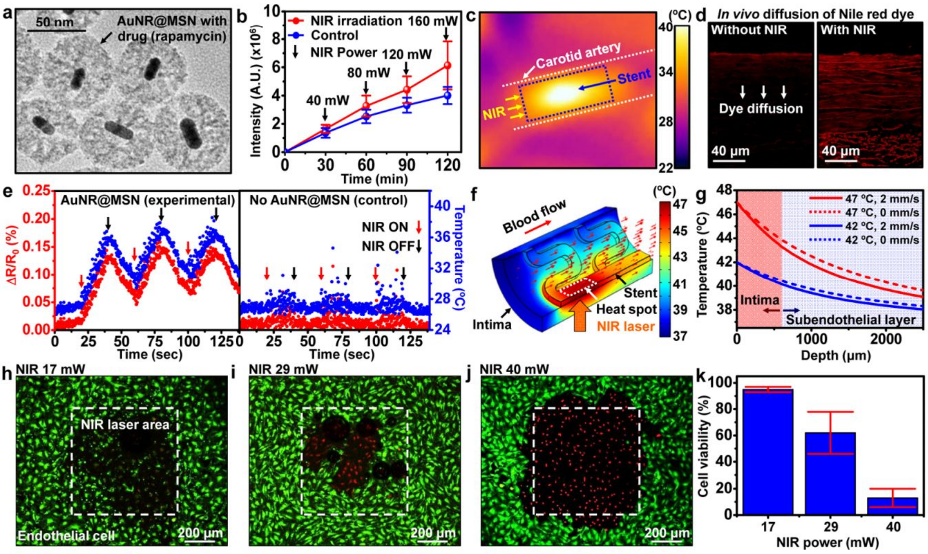

Figure 2.16 Hyperthermia-based controlled drug delivery, integrated temperature sensing, and photothermal therapy. a, TEM image of the AuNR (core)/mesoporous silica (shell) with the anti-stenosis drug (Rapamycin). **b,** Plot of fluorescent intensity as a function of time shows that simulated drug release experiment with fluorescein dyes loaded on AuNR@MSN under the NIR laser irradiation (standard deviation from the mean, n=3). **c,** IR camera image of NIR-based hyperthermia effect on the stent inside a carotid artery. **d,** Fluorescent images that show the diffused Nile red dye (simulated drug) from the BES into the walls of the canine common carotid artery, without (left) and with (right) optical-fiber-guided NIR laser. **e,** Monitoring hyperthermia-induced temperature fluctuations on the BES with (left, experiment) and without (right, control)

AuNR@MSN under the intermittent NIR irradiation. **f,** Thermal finite element modelling (FEM) of the temperature distribution near the stent/intima interface with a blood flow rate of 2 mm/s. The temperature at the heat spot (NIR laser spot) is assumed to be 47 °C. **g,** Plot of the temperature distribution of the vascular tissues near the heated stent (intima and subendothelial layer) as a function of the tissue depth, with (2 mm/s) and without (0 mm/s) the blood flow, for two different temperature settings (42 °C and 47 °C). **h,** Image of HUVECs on the PLA film containing AuNR@MSN. The NIR laser with 17 mW power is exposed in the white dotted box area *in vitro*. The green and red coloured regions indicate live and dead cells, respectively. The photo-bleaching of the green dye is observed. **i,** Image of HUVECs under the NIR laser irradiation with increased power (29 mW). Dead cells (red colour) by the hyperthermia effect are observed. **j,** Image of HUVECs under NIR laser with 40 mW power. All cells exposed to the NIR laser are dead due to the hyperthermia effect of AuNR@MSN. **k,** Cell viability data measured from Figs. 4h-j.

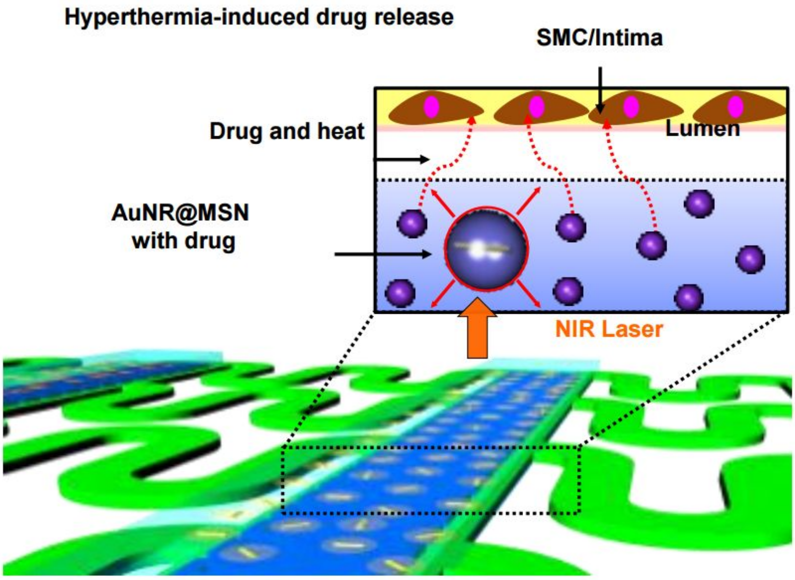

Figure 2.17 Schematic illustration showing the localized and controlled drug delivery by the hyperthermia effect of AuNR@MSN in conjunction with the NIR laser irradiation.

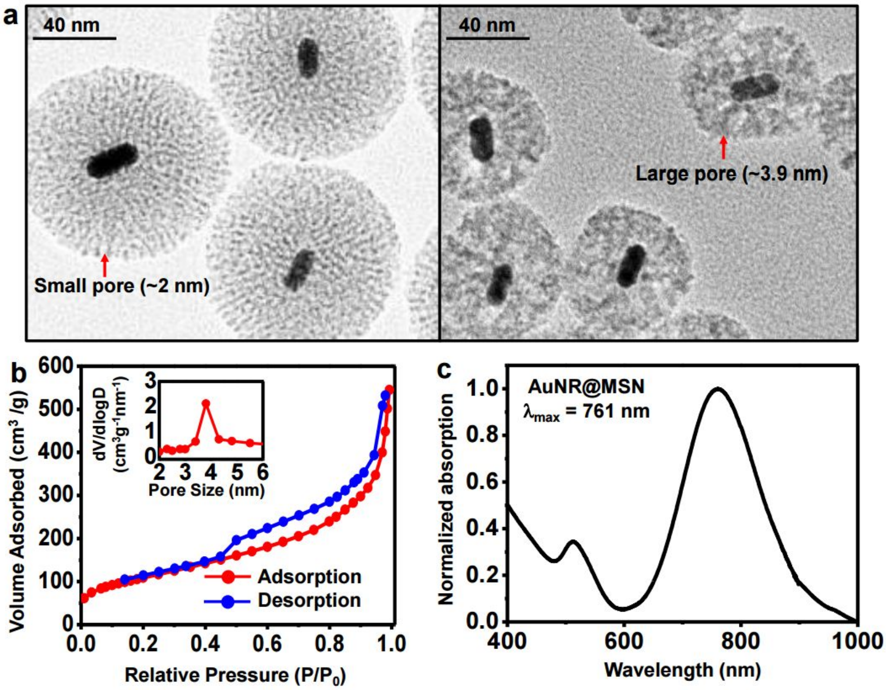

Figure 2.18 a, TEM image of AuNR@MSN with small pore size (left), and large pore size (right). **b,** Plot of the adsorbed N2 volume versus the relative N2 pressure for the measurement of adsorption and desorption isotherms at 77 K. Inset shows the pore distribution of the AuNR@MSN using the Barrett-Joyner-Halenda (BJH) method. **c,** Normalized absorption spectra of AuNR@MSN.

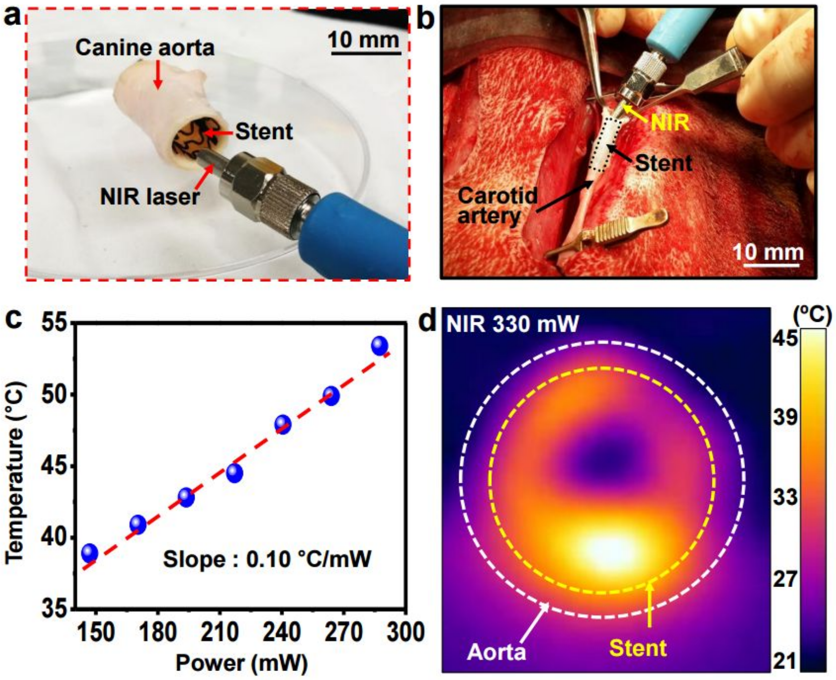

Figure 2.19 a, Image of optical-fiber-guided NIR induced photothermal drug actuation model ex vivo and **b,** in vivo. **c,** Plot of the temperature of BES versus NIR laser power. **d,** Side-view of the IR camera image of the BES inside a canine aorta, heated by the exposure to the optical-fiber-guided NIR laser

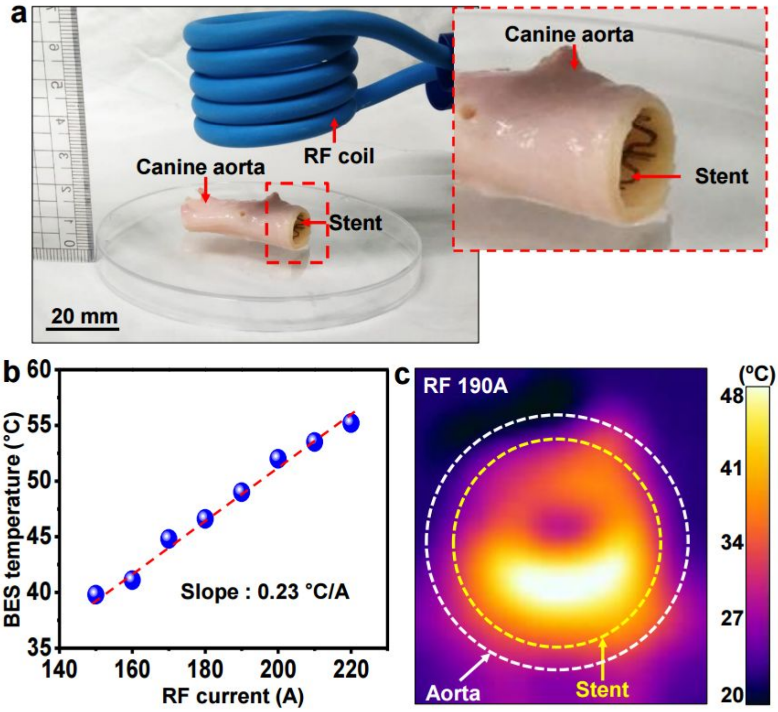

Figure 2.20 a, Image of radio-frequency (RF) magnetic field-induced heating of the BES for the actuation of drug delivery and the magnified image (red dotted box). **b,** Plot of the temperature of the BES versus RF magnetic field. **c,** IR camera image of the stent (side-view) deployed into the canine aorta.

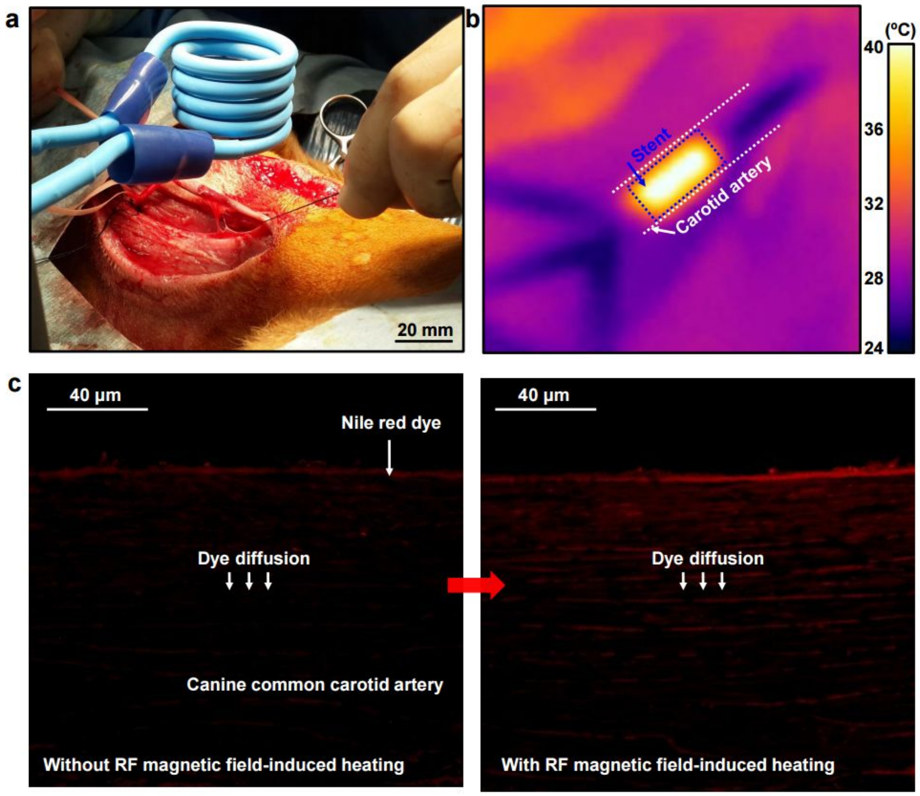

Figure 2.21 a, In vivo experiment image for drug delivery based on RF magnetic field-induced heating. **b,** IR camera images of RF magnetic field-induced heating. **c,** Fluorescent images that show the diffused Nile red dye (simulated drug) from the BES into the walls of the canine common carotid artery, without (left) and with (right) RF magnetic field-induced heating.

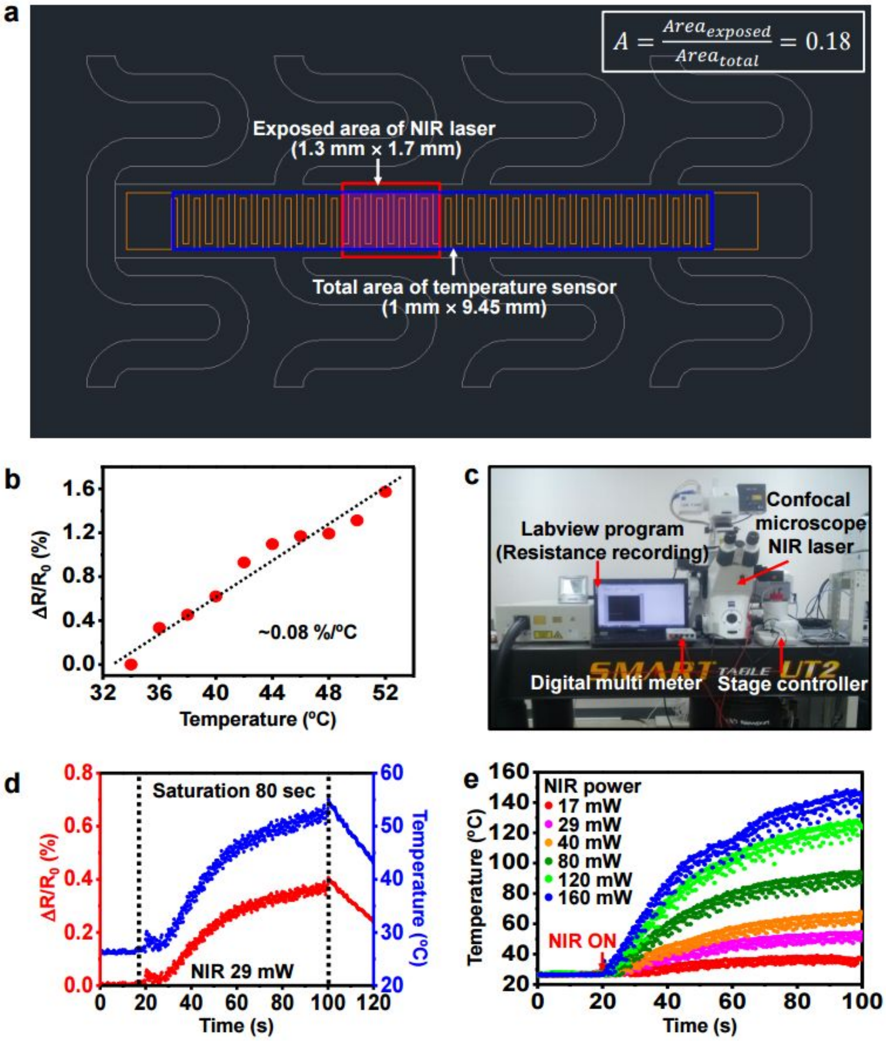

Figure 2.22 a, Schematic diagram showing the area exposed to NIR laser beam spot (18% of the total area of the temperature sensor). **b,** Plot of the percentage resistance change versus the temperature change for the estimation of the modified linear correlation of the temperature sensor. The slope, the temperature

sensor sensitivity, is ~0.08%/°C. **c,** Image of the NIR laser set-up. **d,** Plot of the percentage resistance change (red) and the estimated temperature from the percentage resistance change (blue) as a function of time in 80 seconds NIR laser irradiation with the power of 29 mW. **e,** Plot of the temperature change as a function of the NIR laser irradiation time under various NIR laser power levels, ranging from 17 mW to 160 mW.

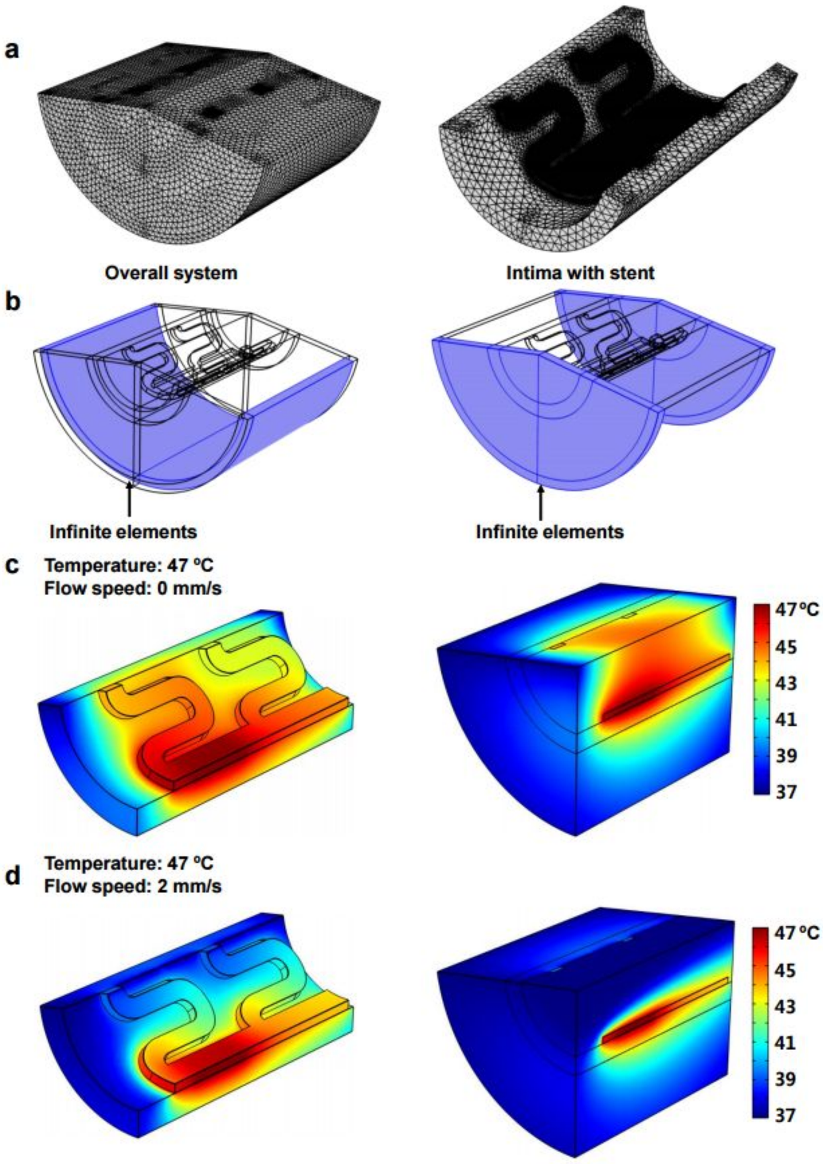

Figure 2.23 a, FEM mesh for the thermal modeling of the BES. **b,** Images of infinite elements along the blood flowing direction (left) and the tissue thickness

direction (right). **c,** Temperature distribution of the entire system (right) in an equilibrium state with a blood flow rate of 0 mm/s. Left shows the temperature distribution of the BES only. **d,** Temperature distribution of the entire system (right) in an equilibrium state with a blood flow rate of 2 mm/s. Left shows the temperature distribution of the BES only.

4.4 Conclusion

The bioresorbable/bioinert nanomaterials, electronics, mechanics and biomedical aspects of the BES described in this study provide new opportunities for the integration of sensors, data storage elements, and optically responsive therapeutic nanoparticles for bioresorbable endovascular implants. This system with on-board bioresorbable sensors and memory modules resolves the limitations of existing stents by enabling the acquisition of physiological signals, data storage, anti-inflammation, localized drug delivery and photothermal therapies through minimally- and/or non-invasive optical control. Numerical modeling and FEM analysis validate the mechanical robustness of the active components and the thermal stability of hyperthermia-induced therapies using nanoparticles, and lay the basis for future optimization of stent design. *In vitro, ex vivo* and *in vivo* studies demonstrate the biocompatibility and multifunctional electronic and therapeutic utilities of the proposed biointegrated system. Further work will focus on the integration of wireless power[12,27,42] and data communication[43-45] in bioresorbable formats.

References

1. Serruys, P. W.; Kutryk, M. J. B.; Ong, A. T. L. Coronary-artery stents. *N. Eng. J. Med.* **2006**, *354*, 483-495.

2. Zlokovic, B. V. Neurovascular pathways to neurodegeneration in Alzheimer's disease and other disorders. *Nat. Rev. Neurosci.* **2011**, *12,* 723-738.

3. Weinberg, M. D.; Lau, J. F.; Rosenfield, K.; Olin, J. W. Peripheral artery disease. Part 2: medical and endovascular treatment. *Nat. Rev. Cardiol.* **2011**, *8*, 429-441.

4. Howard-Alpe, G. M.; Bono, J. de; Hudsmith, L.; Orr, W. P.; Foex, P.; Sear, J. W. Coronary artery stents and non-cardiac surgery. *Brit. J. Anaesth*. **2007**, *98*, 560-574.

5. Jukema, J. W.; Verschuren, J. J. W.; Ahmed, T. A. N.; Quax, P. H. A. Restenosis after PCI. Part 1: pathophysiology and risk factors. *Nat. Rev. Cardiol.* **2012**, *9*, 53-62.

6. Bertrand, O. F.; Sipehia, R.; Mongrain, R; Rodés, J.; Tardif, J.-C.; Bilodeau, L.; Côté, G.; Bourassa, M. G. Biocompatibility aspects of new stent technology. *J. Am. Coll. Cardiol.* **1998***, 32*, 562-571.

7. Stefanini, G. G.; Holmes, D. R. Drug-eluting coronary-artery stents. *N. Eng. J. Med.* **2013**, *368*, 254-265.

8. Son, D.; Lee, J.; Qiao, S.; Ghaffari, R.; Kim, J.; Lee, J. E.; Song, C.; Kim, S. J.; Lee, D. J.; Jun, S. W.; *et al.* Multifunctional wearable devices for diagnosis and therapy of movement disorders. *Nat. Nanotechnol.* **2014**, *9*, 397-404.

9. Kaltenbrunner, M.; Sekitani, T.; Reeder, J.; Yokota, T.; Kuribara, K.; Tokuhara, T.; Drack, M.; Schwödiauer, R.; Graz, I.; Bauer-Gogonea, S.; *et al.* An ultra-lightweight design for imperceptible plastic electronics. *Nature* **2013**, *499*, 458-463.

10. Sekitani, T.; Zschieschang, U.; Klauk, H.; Someya, T. Flexible organic transistors and circuits with extreme bending stability. *Nat. Mater.* **2010**, *9*, 1015-1022.

11. Viventi, J.; Kim, D.-H.; Vigeland, L.; Frechette, E. S.; Blanco, J. A.; Kim, Y.-S.; Avrin, A. E.; Tiruvadi, V. R.; Hwang, S.-W.; Vanleer, A. C.; *et al.* Flexible, foldable, actively multiplexed, high-density electrode array for mapping brain activity *in Vivo*. *Nat. Neurosci.* **2011**, *14*, 1599-1605.

12. Hwang, S.-W.; Tao, H.; Kim, D.-H.; Cheng, H.; Song, J.-K.; Rill, E.; Brenckle, M. A.; Panilaitis, B.; Won, S. M.; Kim, Y.-S.; *et al.* A physically

transient form of silicon electronics. *Science* **2012**, *337*, 1640-1644.

13. Kim, D.-H.; Viventi, J.; Amsden, J. J.; Xiao, J.; Vigeland, L.; Kim, Y.-S.; Blanco, J. A.; Panilaitis, B.; Frechette, E. S.; Contreras, D.; *et al.* Dissolvable films of silk fibroin for ultrathin conformal bio-integrated electronics. *Nat. Mater.* **2010**, *9*, 511-517.

14. Peer, D.; Karp, J. M.; Hong, S.; Farokhzad, O. C.; Margalit, R.; Langer, R. Nanocarriers as an emerging platform for cancer therapy. *Nat. Nanotechnol.* **2007**, *2*, 751-760, (2007).

15. Lohse, S. E.; Murphy, C. J. Applications of Colloidal Inorganic nanoparticles: from medicine to energy. *J. Am. Chem. Soc.* **2012**, *134*, 15607-15620.

16. Mura, S.; Nicolas, J.; Couvreur, P. Stimuli-responsive nanocarriers for drug delivery. *Nat. Mater.* **2013**, *12*, 991-1003.

17. Vivero-Escoto, J.; Huxford-Phillips, R. C.; Lin, W. Silica-based nanoprobes for biomedical imaging and theranostic applications. *Chem. Soc. Rev.* **2012**, *41*, 2673-2685.

18. Karakoti, A.; Singh, S.; Dowding, J. M.; Self, W. T. Redox-active radical scavenging nanomaterials. *Chem. Soc. Rev.* **2010**, *39*, 4422-4432.

19. Huang, X.; El-Sayed, I. H.; Qian, W.; El-Sayed, M. A. Cancer cell imaging and photothermal therapy in the near-infrared region by using gold nanorods. *J. Am. Chem. Soc.* **2006**, *128*, 2115-2120.

20. Kim, C. K.; Kim, T.; Choi, I.-Y.; Soh, M.; Kim, D.; Kim, Y.-J.; Jang, H.; Yang, H.-S.; Kim, J. Y.; Park, H.-K.; *et al.* Ceria nanoparticles that can protect against ischemic stroke. *Angew. Chem. Int. Ed.* **2012**, *51*, 11039-11043.

21. Libby, P.; Simon, D. I. Inflammation and thrombosis: the clot thickens. *Circulation.* **2001**, *103*, 1718-1720.

22. Zhang, Z.; Wang, L.; Wang, J.; Jiang, X.; Li, X.; Hu, Z.; Ji, Y.; Wu, X.; Chen, C. Mesoporous silica-coated gold nanorods as a light-mediated multifunctional theranostic platform for cancer treatment. *Adv. Mater.* **2012**, *24*, 1418-1423.

23. Yan, H.; Teh, C.; Sreejith, S.; Zhu, L.; Kwok, A.; Fang, W.; Ma, X.; Nguyen, K. T.; Korzh, V.; Zhao, Y. Functional mesoporous silica nanoparticles for photothermal-controlled drug delivery *in vivo*. *Angew. Chem. Int. Ed.* **2012**, *51*, 8373-8377.

24. Jabs, A.; Göbel, S.; Wenzel, P.; Kleschyov, A. L.; Hortmann, M.; Oelze, M.; Daiber, A.; Münzel, T. Sirolimus-induced vascular dysfunction. *J. Am. Coll.*

Cardiol. **2008**, *51*, 2130-2138.

25. Ormiston, J. A.; Serruys, P. W. S. Bioabsorbable coronary stents. *Circulation: Cardiovasc. Interv.* **2009**, *2*, 255-260.

26. Zberg, B.; Uggowitzer, P. J.; Löffler, J. F. MgZnCa glasses without clinically observable hydrogen evolution for biodegradable implants. *Nat. Mater.* **2009**, *8*, 887-891.

27. Hwang, S.-W.; Huang, X.; Seo, J.-H.; Song, J.-K.; Kim, S.; Hage-Ali, S.; Chung, H.-J.; Tao, H.; Omenetto, F. G.; Ma, Z.; *et al.* Materials for bioresorbable radio frequency electronics. *Adv. Mater.* **2013**, *25*, 3526-3531.

28. Xu, L.; Yu, G.; Zhang, E.; Pan, F.; Yang, K. *In Vivo* Corrosion behavior of Mg-Mn-Zn alloy for bone implant application. *J. Biomed. Mater. Res. A* **2007**, *83A*, 703-711.

29. Dagdeviren, C.; Hwang, S.-W.; Su, Y.; Kim, S.; Cheng, H.; Gur, O.; Haney, R.; Omenetto, F. G.; Huang, Y.; Rogers, J. A. Transient, biocompatible electronics and energy harvesters based on ZnO. *Small* **2013**, *9*, 3398-3404.

30. Liu, X.; Jin, X.; Ma, P. X. Nanofibrous Hollow Microspheres Self-assembled from star-shaped polymers as injectable cell carriers for knee repair. *Nat. Mater.* **2011**, *10*, 398-406.

31. Hwang, S.-W.; Park, G.; Cheng, H.; Song, J.-K.; Kang, S.-K.; Yin, L.; Kim, J.-H.; Omenetto, F. G.; Huang, Y.; Lee, K.-M.; *et al.* 25th anniversary article: materials for high-performance biodegradable semiconductor devices. *Adv. Mater.* **2014**, *26*, 1992-2000.

32. Murphy, C. J.; Gole, A. M.; Stone, J. W.; Sisco, P. N.; Alkilany, A. M.; Goldsmith, E. C.; Baxter, S. C. Gold nanoparticles in biology: beyond toxicity to cellular imaging. *Acc. Chem. Res.* **2008**, *41*, 1721-1730.

33. Omenetto, F. G.; Kaplan, D. L. New opportunities for an ancient material. *Science* **2010**, *329*, 528-531.

34. Kim, S.; Marelli, B.; Brenckle, M. A.; Mitropoulos, A. N.; Gil, E.-S.; Tsioris, K.; Tao, H.; Kaplan, D. L.; Omenetto, F. G. All-water-based electron-beam lithography using silk as a resist. *Nat. Nanotechnol.* **2014**, *9*, 306-310.

35. Huang, X.; Peng, X.; Wang, Y.; Wang, Y.; Shin. D. M.; El-Sayed, M. A.; Nie, S. A Reexamination of active and passive tumor targeting by using rod-shaped gold nanocrystals and covalently conjugated peptide ligands. *ACS Nano* **2010**, *4*, 5887-5896.

36. Chen, Y.; Chen, H.; Shi, J. *In Vivo* Bio-safety evaluations and diagnostic/therapeutic applications of chemically designed mesoporous

silica nanoparticles, *Adv. Mater.* **2013**, *25*, 3144-3176.

37. Yang, P.; Gai, S.; Lin, J. Functionalized mesoporous silica materials for controlled drug delivery. *Chem. Soc. Rev.* **2012**, *41*, 3679-3698.

38. Hirst, S. M.; Karakoti, A.; Singh, S.; Self, W.; Tyler, R.; Seal, S.; Reilly, C. M. Bio-distribution and *in vivo* antioxidant effects of cerium oxide nanoparticles in mice. *Environ. Toxicol.* **2013**, *28,* 107-118.

39. Kwon, D.-H.; Kim, K. M.; Jang, J. H.; Jeon, J. M.; Lee, M. H.; Kim, G. H.; Li, X.-S.; Park, G.-S.; Lee, B.; Han, S.; *et al.* Atomic structure of conducting nanofilaments in TiO_2 resistive switching memory. *Nat. Nanotechnol.* **2010**, *5,* 148-153.

40. Uchida, T.; Wang, Y.; Rivers, M. L.; Sutton, S. R. Yield strength and strain hardening of MgO up to 8 GPa measured in the deformation-DIA with monochromatic X-ray diffraction. *Earth Planet. Sci. Lett.* **2004**, *226*, 117-126.

41. LaDisa, J. F.; Olson, L. E.; Molthen, R. C.; Hettrick, D. A.; Pratt, P. F.; Hardel, M. D.; Kersten, J. R.; Warltier, D. C.; Pagel, P. S. Alterations in wall shear stress predict sites of neointimal hyperplasia after stent implantation in rabbit iliac arteries. *Am. J. Physiol. Heart Circ. Physiol.* **2005**, *288*, H2465-H2475.

42. Sekitani, T.; Takamiya, M.; Noguchi, Y.; Nakano, S.; Kato, Y.; Sakurai, T.; Someya, T. A Large-area wireless power-transmission sheet using printed organic transistors and plastic MEMS switches. *Nat. Mater.* **2007,** *6*, 413-417.

43. Chow, E. Y.; Chlebowski, A. L.; Chakraborty, S.; Chappell, W. J.; Irazoqui, P. P. Fully wireless implantable cardiovascular pressure monitor integrated with a medical stent. *Biomed. Eng. IEEE Trans.* **2010**, *57*, 1487-1496.

44. Tao, H.; Brenckle, M. A.; Yang, M.; Zhang, J.; Liu, M.; Siebert, S. M.; Averitt, R. D.; Mannoor, M. S.; McAlpine, M. C.; Rogers, J. A.; *et al.* Silk-based conformal, adhesive, edible food sensors. *Adv. Mater.* **2012,** *24*, 1067-1072.

45. Kim, T.-i.; McCall, J. G.; Jung, Y. H.; Huang, X.; Siuda, E. R.; Li, Y.; Song, J.; Song, Y. M.; Pao, H. A.; Kim, R.-H.; *et al.* Injectable, cellular-scale optoelectronics with applications for wireless optogenetics. *Science* **2013,** *340*, 211-216.

46. Yin, L.; Huang, X.; Xu, H.; Zhang, Y.; Lam, J.; Cheng, J.; Rogers, J. A. Materials, designs, and operational characteristics for fully biodegradable primary batteries. *Adv. Mater.* **2014,** *26*, 3879-3884.

47. Juni, R. P.; Duckers, H. J.; Vanhoutte, P. M.; Virmani, R.; Moens, A. L.

Oxidative stress and pathological changes after coronary artery interventions. *J. Am. Coll. Cardiol.* **2013,** *61*, 1471-1481.

48. Taniyama, Y.; Griendling, K. K. Reactive oxygen species in the vasculature: molecular and cellular mechanisms. *Hypertension* **2003,** *42*, 1075-1081.

49. Lee, J. E.; Lee, N.; Kim, T.; Kim, J.; Hyeon, T. Multifunctional mesoporous silica nanocomposite nanoparticles for theranostic applications. *Acc. Chem. Res.* **2011,** *44*, 893-902.

50. Kastrati, A.; Mehilli, J.; von Beckerath, N.; *et al.* Sirolimus-eluting stent or paclitaxel-eluting stent *vs* balloon angioplasty for prevention of recurrences in patients with coronary in-stent restenosis: a randomized controlled trial. *J. Am. Med. Assoc.* **2005,** *293*, 165-171.

51. Hirsch, L. R.; Stafford, R. J.; Bankson, J. A.; Sershen, S. R.; Rivera, B.; Price, R. E.; Hazle, J. D.; Halas, N. J.; West, J. L. Nanoshell-mediated near-infrared thermal therapy of tumors under magnetic resonance guidance. *Proc. Nat. Acad. Sci.* **2003,** *100*, 13549-13554.

52. Yeager, D.; Chen, Y.-S.; Litovsky, S.; Emelianov, S. Intravascular photoacoustics for image-guidance and temperature monitoring during plasmonic photothermal therapy of atherosclerotic plaques: a feasibility study. *Theranostics* **2014,** *4*, 36-46.

53. Yoo, H.; Kim, J. W.; Shishkov, M.; Namati, E.; Morse, T.; Shubochkin, R.; McCarthy, J. R.; Ntziachristos, V.; Bouma, B. E.; Jaffer, F. A.; *et al.* Intra-arterial catheter for simultaneous microstructural and molecular imaging *in Vivo*. *Nat. Med.* **2011,** *17*, 1680-1684.

54. de Groot, E.; Hovingh, G. K.; Wiegman, A.; Duriez, P.; Smit, A. J.; Fruchart, J.-C.; Kastelein, J. J. P. Measurement of arterial wall thickness as a surrogate marker for atherosclerosis. *Circulation* **2004,** *109*, III-33-III-38.

55. Brinton, M. R.; Tagge, C. A.; Stewart, R. J.; Cheung, A. K.; Shiu, Y.-T. E.; Christensen, D. A. Thermal sensitivity of endothelial cells on synthetic vascular graft material. *Int. J. Hyperthermia* **2012,** *28*, 163-174.

56. Waxman, S.; Ishibashi, F.; Muller, J. E. Detection and treatment of vulnerable plaques and vulnerable patients: novel approaches to prevention of coronary events. *Circulation* **2006,** *114*, 2390-2411.

요약 (국문초록)

연성 및 생재흡수성 전자소자용 비휘발성 메모리 소자와 집적센서 구현

최근 나노물질과 마이크로 전자공학기술 기반으로 헬스케어 관련한 많은 연구가 진행되고 있다. 하지만 기존의 딱딱한 기판에 만들어진 전자소자는 고유의 기계적 성질 때문에 비침습성 혹은 최소 침습성 의료전자소자에 적용하기 매우 어려웠다. 본 논문에는 두가지 종류의 다기능성 전자소자시스템을 다루고 있다.

첫째로, 탑-다운 방식으로 제작된 나노박막과 바텀-업 방식으로 합성된 나노튜브/나노입자를 피부와 기계적 특성이 유사한 고분자 기판에 적용하여 입을 수 있는 전자시스템을 소개한다. 이러한 시스템은 늘일 수 있는 기계적 특성을 지니면서, 생체신호용 센서, 비휘발성 메모리, 논리회로, 약물주입기등을 포함한다. 또한 각각의 전자소자의 기계적 특성 및 열전달 특성에 기인한 약물주입을 가능하게 하는 원리를 정량적으로 분석하여 시스템 수준의 다기능성의 효과를 검증하였다.

둘째로, 혈관질병 진단 및 치료용 생재흡수성 전자스텐트를 소개한다. 본 논문에서 소개하는 전자스텐트는 국소약물주입 및 혈관치료용 나노입자를 담지하면서, 혈류를 측정하고 데이터를 저장하는 메모리소자에 실시간으로 저장할 수 있다. 또한, 내부에 전자소자를 구동시키기 위한 전원을 무선으로 공급받을 수 있으며, 데이터를 무선으로 외부에 전송할 수 있는 기능을 탑재했다. 새롭게 제시된 생재흡수성 전자스텐트는 동물실험에 적용하여 혈관치료에 새로운 가능성을 제시하게 되었다.

위에 언급된 두가지 다기능성 전자시스템은 모두 생체신호를 정밀하게 진단할 수 있었으며, 실시간으로 데이터를 저장해서 최적의 치료가 가능해 질 수 있는 시스템적인 집적기술을 제시했다. 이러한 기술은 외부에 강한 충격 및 높은 습도에서도 선택적으로 적용되어 환자 맞춤형으로 작동 될 수 있음을 보여주었다.

주요어: 늘일 수 있는 전자소자, 입을 수 있는 전자소자, 생재흡수성 전자소자, 비휘발성 메모리, 논리회로, 스텐트, 센서

학번: 2012-30742 성명 : 손 동 희